Estimating Snowfall Metrics with a Terrestrial Laser Scanner

by

Sven Alexander Sorhus

A thesis submitted to the Civil and Environmental Engineering,

Cullen College of Engineering

in partial fulfillment of the requirements for the degree of

MASTER OF SCIENCES

in Geosensing Systems Engineering and Sciences

Chair of Committee: Dr. Craig Glennie

Committee Member: Dr. Shad O'Neel

Committee Member: Dr. Preston Hartzell

University of Houston

May 2021

ACKNOWLEDGMENTS

I would like to sincerely thank Dr. Craig Glennie for his continued support, guidance and mentorship. He has provided sound advice, logical reasoning and enlightening encouragement, which I am forever grateful for. It has been an honor to have him as my graduate advisor.

Thank you to Dr. Shad O'Neel and Dr. Preston Hartzell for being a part of my defense committee, providing insight and helping me throughout my academic career.

A special thanks to Adam LeWinter for allowing me the opportunity to contribute towards this research project. And thank you to Aaron Kehl and Ned Bair for their efforts in collecting the data that was used in this research.

Finally, I would like to thank my parents for their unwavering support through all of my endeavors in life and always being there for me.

ABSTRACT

This thesis examines lidar (light detection and ranging) scans collected from a Terrestrial Laser Scanner (TLS) during varying snowfall events with the goal of determining its capability to make measurements in a degraded visual environment and the feasibility of using it as a meteorological instrument. The ability to estimate visibility, snowfall intensity rate, particle size and velocity of hydrometeors are explored by comparing metrics derived from lidar scans with estimations obtained from an optical disdrometer.

Statistics based on return counts, ranges and reflectance values from the TLS measurements of hydrometeors and static targets were used for comparisons and modeling the parameters of interest. Estimated hydrometeor sizes are much smaller than the laser footprint, preventing bulk statistical comparisons from revealing clear correlations. The TLS is capable of estimating hydrometeor velocities when conditions are conducive; however, results are sporadic and selection of returns must be considered as systematic errors yield unreasonable estimations. Regression between TLS metrics and the optical disdrometer estimates for visibility and snowfall intensity proved statistically significant. This indicates that a TLS provides informative measurements during varying atmospheric conditions of snowfall.

Results show that TLS has potential to estimate visibility and a snowfall intensity rate, but has difficulty estimating hydrometeor size and speed. Visibility estimations from a laser scanner with a larger range of spatial measurements will be an improvement compared to the optical disdrometer, which samples a static position and

extrapolates based on the assumption of atmospheric homogeneity. This would allow the ability to monitor a larger spatial extent with a higher degree of accuracy.

Contents

ACKNOWLEDGMENTS II

ABSTRACT III

LIST OF TABLES VIII

LIST OF FIGURES IX

1. INTRODUCTION 1

2. INSTRUMENTATION 9

2.1. Site Location 9

2.2. Riegl VZ-400 11

2.3. OTT Hydromet Parsivel^2 Disdrometer 16

2.4. Snow Pillow 19

2.5. Lufft WS600-UMB Smart Weather Sensor 20

2.6. Judd Ultrasonic Depth Sensor 21

3. METHODS 22

3.1. TLS Lidar 22

3.1.1. VZ-400 22

3.1.2. Data Processing 25

3.2. Target Statistics 31

3.3. Disdrometer Data 32

3.3.1. Hydrometeor Size and Velocity 35

4. RESULTS 39

4.1. Line Scan Statistics 39

4.1.1. Count Statistics 39

4.1.2. Range and Reflectance Statistics 42

4.1.3. Range Histograms 42

4.2. Target Statistics 45

4.2.1. Spectralon Panel 45

4.2.2. Tree Trunk 48

4.3. Reflectance Fluctuations 50

4.4. JUDS Comparison 52

4.5. Discrepant Scans 55

4.6. Full-waveform 58

4.7. Particle Size 65

4.8. Particle Speed 68

4.9. Snowfall Intensity 70

4.10. Visibility 77

5. DISCUSSION 89

5.1. Can a TLS provide similar or enhanced snowfall metrics compared to other meteorological sensors? 89

5.2. Does FW scanning provide better snowfall estimation? 90

5.3. Can particle velocities be determined from a TLS? 90

5.4. Are there any noticeable variations in data metrics due to hydrometeor size? 91

5.5. Is a TLS able to estimate a snowfall intensity rate? 92

5.6. Do variations in TLS measurements relate to visibility? 92

6. CONCLUSION AND FUTURE WORK 94

REFERENCES 99

APPENDIX A 106

APPENDIX B 108

APPENDIX C 109

APPENDIX D 110

APPENDIX E 111

APPENDIX F 113

LIST OF TABLES

Table 1. Riegl VZ-400 specifications. 12

Table 2. TLS settings for different data collections. *Frame scan settings were adjusted midway through the season 23

Table 3: Hydrometeor count and corrections of presented line scans. 31

Table 4: Spectralon average reflectance for varying internal temperatures of VZ-2000. 52

Table 5: Height comparison of TLS and JUDS. 53

Table 6: Non-linear regression results from 1st return reflectance average vs disdrometer snow intensity. 71

Table 7: Multi-variable linear regression statistics for disdrometer snow intensity model. 74

Table 8: Nonlinear regression results from near count total and disdrometer MOR. 80

Table 9: Nonlinear regression results for far count total vs disdrometer MOR. 81

Table 10: Statistical results of linear regression models of disdrometer MOR. 84

LIST OF FIGURES

Figure 1: Instrument for measuring fall speeds of solid precipitation (Locatelli and Hobbs 1974).. 4

Figure 2: Point return metrics from visibility study (Pfenningbauer et al. 2014) – full visibility (left column), 40-meter visibility (middle column), 10-meter visibility (right column). First return – blue points, second return – green points. 6

Figure 3: Waveforms from the VZ-1000 in varying foggy conditions (Pfenningbauer et al. 2014). 7

Figure 4: Sesame street snow study plot location. 9

Figure 5: Spectralon panel installed at Sesame site. 10

Figure 6: Typical reflectance for a 99% Spectralon panel. 11

Figure 7: Riegl VZ-400 in protective housing unit at Sesame. 12

Figure 8: Spectral reflectance properties for snow (Deems et al. 2013). 13

Figure 9: Intensity values from amplitude (left) and relative reflectance (right) of a frame scan. 15

Figure 10: VZ-400 amplitude return ranges from a calibration target (Pfennigbauer and Ullrich 2010). 15

Figure 11: OTT Hydromet Parsivel^2 Disdrometer (OTT Hydromet). 17

Figure 12: Extinction illustration (OTT Hydromet).. 18

Figure 13: Results from Parsivel measurements (Battaglia et al. 2010). 19

Figure 14: WS600-UMB smart weather sensor (Lufft). 20

Figure 15: Judd ultrasonic depth sensor (Judd Communications). 21

Figure 16: Frame scan collected before snow season with ground (brown) and tree (grey-scaled intensity) returns. 22

Figure 17: Frame scan with ground (brown) and tree (grey-scaled intensity) returns overlaid with both line scans (blue). 23

Figure 18: Timeline of data acquisitions. Blue depicts confirmed snow events, red depicts discrepant snow events and black depicts a frame scan. 24

Figure 19: Size reference for data collection. 25

Figure 20: Good line scan classification - hydrometeors (red) and non-hydrometeors (blue). 28

Figure 21: Few line scan misclassification - hydrometeors (red) and non-hydrometeors (blue). 29

Figure 22: Many line scan misclassification - hydrometeors (red) and non-hydrometeors (blue). 29

Figure 23: Corrected line scan classification - hydrometeors (red) and non-hydrometeors (blue). 30

Figure 24: Location of returns examined from the Spectralon panel and tree trunk. 32

Figure 25: TLS snow count with disdrometer intensities – large variations. 33

Figure 26: TLS snow count with disdrometer intensities – small variations. 34

Figure 27: TLS snow count with disdrometer intensities – discrepant scan. 34

Figure 28: Example of estimated particle size count from disdrometer. 35

Figure 29: Example of estimated particle speed count from disdrometer. 35

Figure 30: Example of point streaks from hydrometeors in a section of the frame scan. 36

Figure 31: Point returns from a frame scan. 37

Figure 32: Point streaks from a frame scan classified by linearity. 38

Figure 33: Point streaks from a frame scan with classified linearity values over 99%. 38

Figure 34: Echo return counts from line scans. 40

Figure 35: Total laser returns per laser pulse counts. 40

Figure 36: Bar graph of near count totals for TLS line scans. 41

Figure 37: Line scan range histograms - light snowfall (top), heavy snowfall (bottom). 43

Figure 38: Line scan range histograms with exponential fits and e-folding lengths. 44

Figure 39: First return average reflectance of Spectralon panel from frame scans. Undetected snow events from December 5th-16th highlighted in red. 45

Figure 40: Daily cyclical variation of average reflectance from Spectralon panel – May. 46

Figure 41: Daily cyclical variation of average reflectance from Spectralon panel – November. 46

Figure 42: First and second average reflectance returns of Spectralon panel from frame scans. 47

Figure 43: First and second average reflectance returns of Spectralon panel from frame scans – November-December. 48

Figure 44: First and second average reflectance return of a tree trunk from the frame scan. 49

Figure 45: Daily cyclical variation of average reflectance from a tree trunk. 49

Figure 46: Spectralon first return reflectance average and ambient temperatures in May. 50

Figure 47: Spectralon scans of varying internal temperature of TLS:
February 16th – (a) 77 °F, (b) 55.4 °F, (c) 39.2 °F and
February 7th – (d) 78.8 °F, (e) 66.2 °F, (f) 59 °F. 51

Figure 48: Snow height measurements from TLS and JUDS. 53

Figure 49: TLS snow height and SWE. 54

Figure 50: Snow height and average return reflectance. 55

Figure 51: Robust and discrepant line scan comparisons. 56

Figure 52: Average Spectralon reflectance colored by return count. 57

Figure 53: Intended (left side) and actual (right side) check volume
locations. 58

Figure 54: RiSCAN Pro full-waveform results from a laser pulse. 59

Figure 55: Line scan deviation in RiSCAN Pro. 60

Figure 56: Full-waveform of single hydrometeor with low deviation. 60

Figure 57: Full-waveform of two hydrometeors with minor deviation. 61

Figure 58: Full-waveform of hydrometeor near snow surface with
minor deviation. 61

Figure 59: Full-waveform of hydrometeor above the snow surface with
low deviation. 62

Figure 60: Full-waveform of two closely spaced hydrometeors with
higher (yellow) deviation. 62

Figure 61: Full-waveform of a hydrometeor near the snow surface with higher (orange) deviation. 62

Figure 62: Full-waveform of a hydrometeor near the snow surface with high (red) deviation. 63

Figure 63: Line scan with range reductions 63

Figure 64: FW of returns that met extinction in the atmosphere at different ranges. (a) 15 meters, (b) 26 meters, (c) 47 meters. 64

Figure 65: Median disdrometer size vs. ambient air temperature. 65

Figure 66: Median disdrometer size vs. Spectralon second return reflectance average. 66

Figure 67: Median disdrometer size vs near count total. 67

Figure 68: Median disdrometer size vs average hydrometeor range. 67

Figure 69: PD speed estimates (top) and manually calculated speeds from TLS (bottom). 68

Figure 70: Automatically calculated streak velocities. 70

Figure 71: Automatically calculated streak velocities - filtered by count and speed. 70

Figure 72: Non-linear regression of 1st return reflectance average vs. disdrometer snow intensity. 71

Figure 73: Near frame reflectance returns. 72

Figure 74: Average reflectance 1st return vs average hydrometeor range. 73

Figure 75: Multi-variable linear regression of near count total, average reflectance 1st return, return count 1 and 2 vs disdrometer snow intensity. 74

Figure 76: Average second return reflectance from Spectralon panel of frame scans identified with hydrometeors vs disdrometer snow intensity. 75

Figure 77: Average second return reflectance from Spectralon line scan vs disdrometer snow intensity. 76

Figure 78: Average second return reflectance from Spectralon panel of frame scans identified with hydrometeors vs disdrometer snow intensity – zoomed in. 76

Figure 79: Disdrometer snow intensity vs MOR. 78

Figure 80: Disdrometer MOR vs near count total. 78

Figure 81: Disdrometer snow intensity vs MOR – zoomed in. 79

Figure 82: Nonlinear regression of near count total and disdrometer MOR. 79

Figure 83: Nonlinear regression of far count total vs disdrometer MOR. 81

Figure 84: e-folding length vs disdrometer MOR (limited to 5000 meters). Colored by disdrometer snow intensity estimate. 82

Figure 85: e-folding length vs disdrometer MOR (limited to 1000 meters). Colored by disdrometer snow intensity estimate. 82

Figure 86: Linear regression of e-folding length vs disdrometer MOR. 83

Figure 87: Multi-variable linear regression of far count total, average hydrometeor range, average 2nd return reflectance from Spectralon panel vs disdrometer MOR. 84

Figure 88: Frame scan Spectralon panel – Average 2nd reflectance return vs disdrometer MOR. 85

Figure 89: Spectralon line scan – Average 2nd reflectance return vs disdrometer MOR. 86

Figure 90: Line scans of maximum line scan range reductions 87

Figure 91: Webcam images from CUES site - reduced visibility (top), clear visibility (bottom) 88

1. INTRODUCTION

Snow is a natural phenomenon that affects various aspects of human life and global climate ranging from transportation to water resources. Snowfall degrades the visual environment with occlusions from snow particles and by scattering visible light. Snow can create hazardous conditions for vehicles and aviation when visibility conditions approach whiteout, resulting in partial or total loss of visibility. Lowered visibility is responsible for many multi-vehicle collisions. In 2019, whiteout conditions in Neenah, Wisconsin resulted in 131-vehicle pileup that caused one fatality and injured 71 others (CNN 2019). The severity of these types of accidents could easily be minimized if drivers are alerted to reduce their speeds, allowing drivers adequate time to stop if there is an accident up ahead. Considering these types of collisions still occur to this day, could an automated warning system exist to better alert drivers?

In addition to civilian applications, the military has significant interest in exploring technology that can mitigate the effects of a Degraded Visual Environment, DVE. The U.S. Army Combat Readiness Center Director of the Aviation Directorate, Lt. Col. Mike Higginbotham, reported in 2014 that a DVE accounted for 24% of the Army's flight accidents in the past 12 years (Higginbotham 2014). The Command, Control, Communications, Computers, Cyber, Intelligence, Surveillance and Reconnaissance, has a directorate dedicated to research and development of night vision and electronic sensors. Integrating new sensors and tactics can improve the ability to acquire targets and aid in navigation of vehicles that must operate in a DVE.

The US Army Combat Capabilities Development Command is conducting a multi-year program addressing DVE mitigation. Interest is in creating a fusion of multiple sensor modalities to be able to operate in all types of DVE. In comparison to how night vision goggles allowed Army Aviation to “own the night”, the ability to safely operate in any weather conditions will enable the army to “own the environment” (Bratt and Walker 2019).

Visibility is a complex metric to estimate due to the many variables and conditions that affect it, such as the environment, light sources, object reflectance and scattering of light. These conditions can change in localized areas within a matter of minutes due to microclimate changes. Most commercially available visibility sensors rely on measurements of light scattered at a certain angle from a small sample volume, which is unable to account for spatial variance and is difficult to accurately correlate to human visibility, especially during precipitation events (Wang et al. 2014).

From a meteorological standpoint, snowfall measurements at a single location and estimation across a larger spatial area is also a complex problem, due to variations in shape, size, and microphysical properties of hydrometeors. The World Meteorological Organization, WMO, defines a hydrometeor as a liquid or solid that is either suspended in the atmosphere, falling through the atmosphere or blown by the wind from the Earth’s surface (WMO 2008). Precipitation gauge analyses show that wind-induced losses can significantly reduce hydrometeor catch by up to 80% (Sevruk et al. 2009). Precipitation gauges measure accumulation over time and do not provide any additional properties of the hydrometeors. They only collect data at a single location, as extrapolation to broad areas is challenged by the high spatial variability of snow accumulation and transport.

The development of radar systems to estimate precipitation on a larger spatial scale has been ongoing since the 1970's (Sekhon and Srivastava 1969). "A detailed understanding of the geometric, microphysical, and scattering properties of ice hydrometeors is a vital prerequisite for the development of radar-based quantitative precipitation estimation (QPE) algorithms" (Huang et al. 2019). The utility of accurate forecasts generates strong scientific interest in measuring hydrometeor size and velocity. Instruments that are capable of these measurements are known as a disdrometer and measurements of various physical principles have been explored and studied in the past such as impact techniques, imaging techniques and scattering techniques (Löffler-Mang and Joss 2000).

Locatelli and Hobbs (1974) created one of the first optical instruments to measure the fall speeds of solid precipitation (Figure 1). It uses incandescent lamps to create two parallel beams of light separated by a small gap; photomultiplier tubes are used to measure the change in intensity as particles fall through. The velocity is calculated using the time interval between the peak intensity differences. Extensive manual labor was required for observing hydrometeors that fell through the optical sensor: classifying the hydrometeor type, collecting their dimensions, and weighing their mass. Once sufficient data was collected for a certain type of hydrometeor, various models could be derived to compare velocity, size, and mass. These mass/fall speed models have been used as a reference in later studies of solid precipitation.

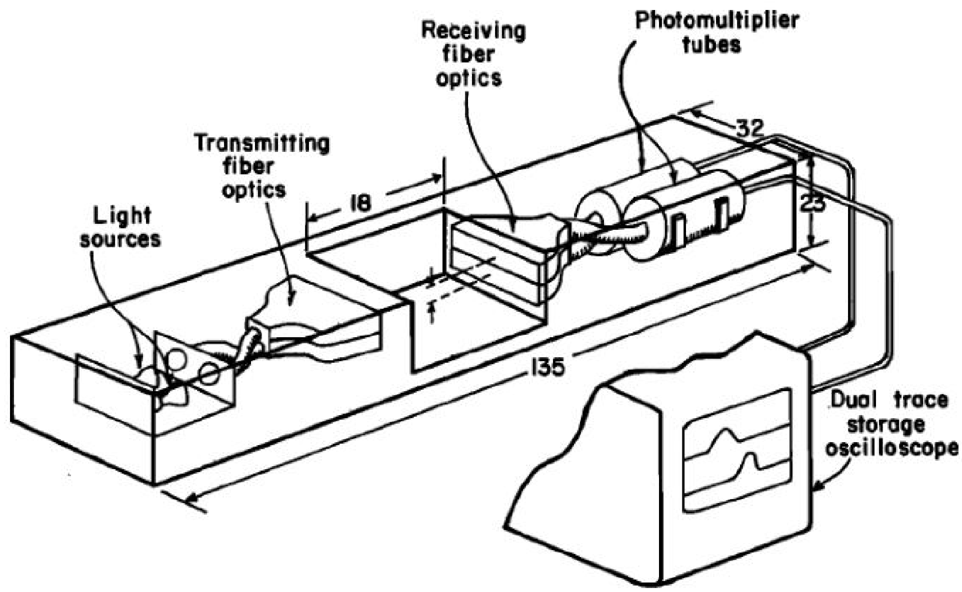

Figure 1: Instrument for measuring fall speeds of solid precipitation (Locatelli and Hobbs 1974)

Kwon (2004) collaborated with the Minnesota Department of Transportation to research visibility measurements by processing images acquired from video cameras along a highway that frequently experiences low visibility due to snow squalls and fog. This research introduced a relative visibility concept by using image processing from video cameras and revealed some of the shortcomings of this method. Images acquired from highway video cameras have limited resolution and accuracy, making it difficult to capture accurate luminance due to camera noise. Images are also not able to provide spatial information, requiring multiple targets to be set up at varying distances. In addition, the camera's inability to capture images at night requires use of external light sources to illuminate targets.

The use of lidar (light detection and ranging) in laser scanning systems has revolutionized many branches of engineering and Earth sciences with its ability to create dense 3D models, often referred to as point clouds, from laser-pulse echo returns of the environment surrounding the scanner. As technology has advanced, laser scanning system capabilities have improved and become more accessible to researchers and industry professionals. This has enabled a variety of new applications to be explored and investigated with this new technology (Barup et al. 2010, Bhardwaj et al. 2016, Telling et al 2017).

Terrestrial Laser Scanner (TLS) systems have been used for many different snow studies, most often mapping snow depths (water equivalence) or monitoring critical areas that are susceptible to avalanches (Prokop 2008, Deems et al 2015). These studies require repeat scans, the first scan is before the snow season to get ground conditions; sequential scans are performed after snow events to assess snow surface height. Acquiring a scan in the field can be time consuming, cost-prohibitive, and potentially dangerous depending on the location. The presence of hydrometeors in the atmosphere introduces noise and potential occlusions that can reduce the effective range and accuracy of a TLS scan; therefore, these conditions are usually avoided. However, rather than avoiding these conditions, this thesis examines whether the noise, occlusions, and reduced range experienced by TLS measurements during a hydrometeor event can be used to extract metrics describing the current weather conditions.

Pfenningbauer et al. (2014) conducted an experimental setup using a Riegl VZ-1000 inside a fog chamber to evaluate the scanners ability to acquire target returns in adverse atmospheric conditions. Figure 2 shows the range, amplitude, reflectance and pulse-shape deviation from returns collected by the TLS targeting a black and a white panel at a distance of 30 meters for various visibility conditions. These results show

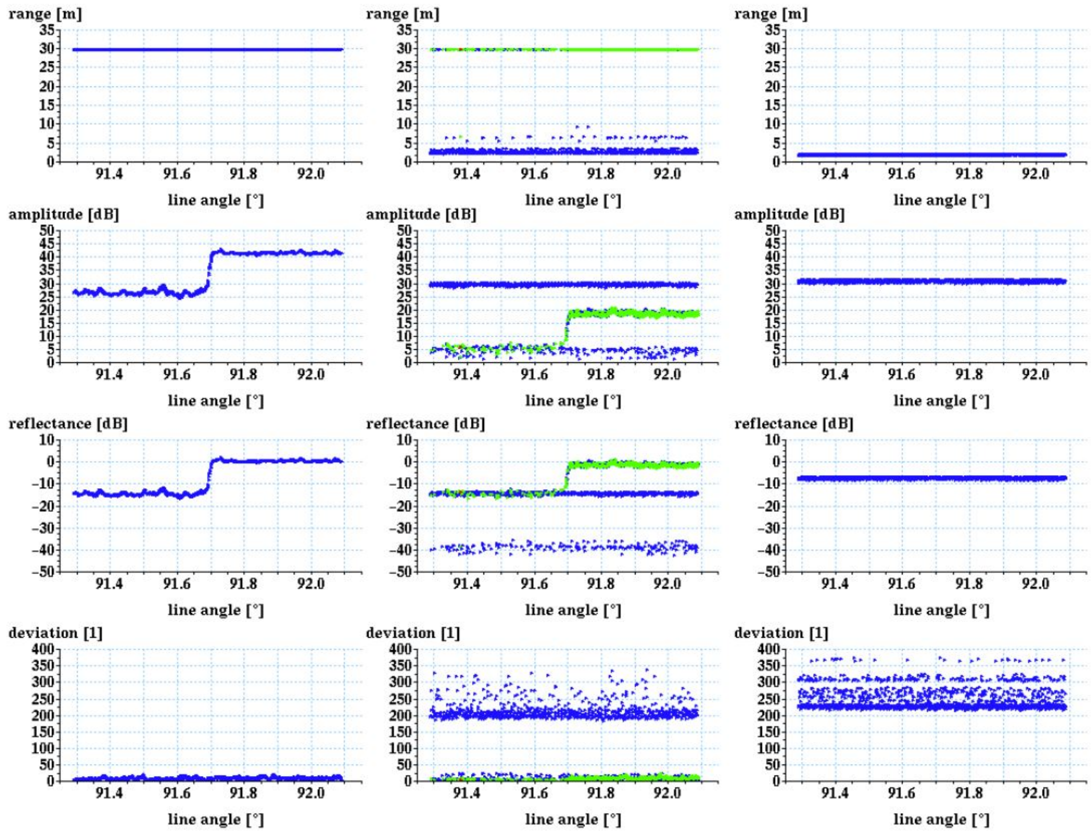

Figure 2: Point return metrics from visibility study (Pfenningbauer et al. 2014) – full visibility (left column), 40-meter visibility (middle column), 10-meter visibility (right column). First return – blue points, second return – green points.

that the scanner is capable of observing a target with partial obstruction from fog particles and is capable of experiencing whiteout conditions due to dense fog. Figure 3 shows full-waveform (FW) results from fog returns for six different visibility ranges and the insert provides the corresponding mean waveforms for comparison in one single chart. The study proposed that the visibility range could be determined by the distance from the center of mass to the rising edge of the fog's echo waveform. There

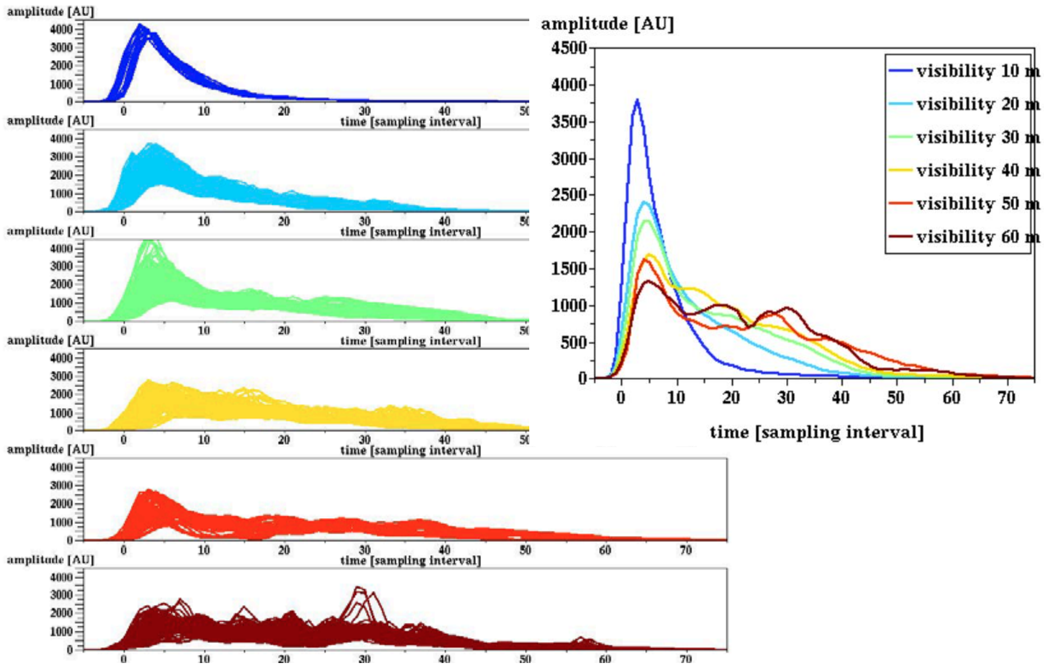

Figure 3: Waveforms from the VZ-1000 in varying foggy conditions (Pfenningbauer et al. 2014).

is interest to examine FW results during heavy snowfall events to see if waveform characteristics can provide more insight than a single return point.

The Cold Regions Research and Engineering Laboratory (CRREL) conducted a novel research project attempting to identify and characterize the different conditions that affect the optical transmissivity of falling and blowing snow using a TLS system co-located with a first-order meteorological station. This thesis analyses lidar scans collected during the 2019-2020 winter season at Mammoth Lakes California, with the goal of answering or informing the following questions:

- Can a TLS provide similar or enhanced snowfall metrics compared to other meteorological sensors?
- Does FW scanning provide any additional insight during snowfall events?
- Can hydrometeor velocities be determined from a TLS?

- Are there any noticeable variations in TLS metrics due to hydrometeor size?
- Is a TLS able to estimate a snowfall intensity rate?
- Do variations in TLS measurements relate to visibility?

If successful, TLS systems could potentially improve or supplement spatial-temporal snowfall measurements to further aid the meteorological community and regions that experience extreme snow events leading to hazardous visibility conditions.

2. INSTRUMENTATION

2.1. Site Location

The Sesame Street Snow Study Plot (Sesame; Figure 4), is located in Mammoth Lakes, California (37°39'0" N, 119°2'30" W) at an elevation of 2743 m. Sesame is a primary weather station for Mammoth Mountain ski resort. Trees surround the Sesame site, which helps reduce wind effects, but also limits the range the TLS is able to scan. The region receives heavy winter precipitation with an average of 890 mm snow water equivalent (SWE) and 7.2 m of snow depth from December through March (Bair 2013). The high elevation of Sesame leads to colder temperatures and infrequent mid-winter rains. CRREL has a worked at this location in the past for various snow studies and has a weather station, CUES, on the mountain in collaboration with the University of California – Santa Barbara (Davis et al. 1999, Bair et al. 2015).

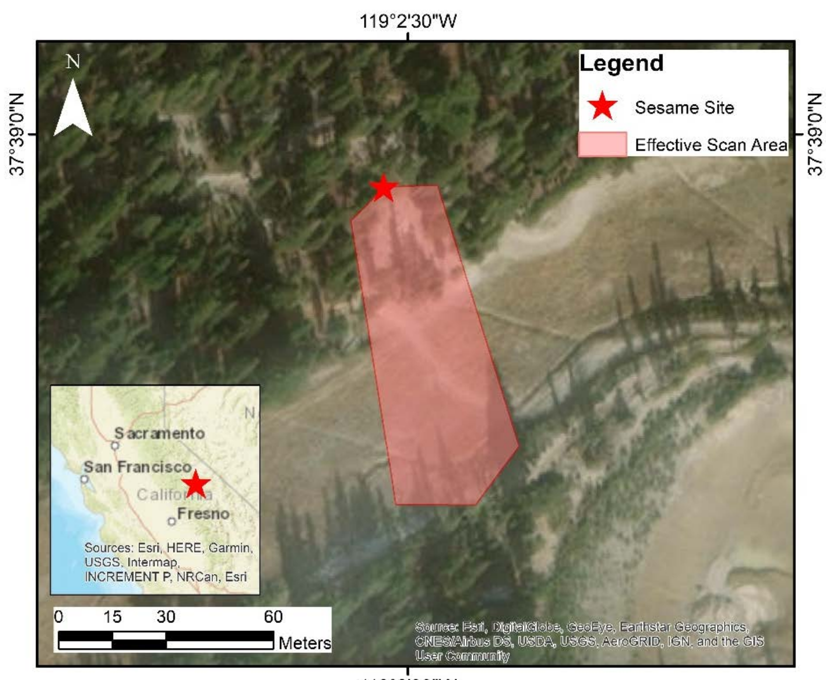

Figure 4: Sesame street snow study plot location.

The Sesame TLS was permanently installed with the intention of collecting data when hydrometeors are present. To avoid the need for an operator to initiate the scanner whenever there was a snowfall event, an automated system was setup. The scanner operated autonomously via programmed scripts throughout the entire snow season. This created a large lidar database of the snow surface conditions and many scans acquired during snowfall events of varying intensity. Details on the data acquisitions from the TLS sensor are given in Chapter 3.

To help measure system performance, a calibration framework was setup using a Spectralon target. Spectralon is a diffuse reflectance material composed of pure polytetrafluoroethylene polymer resin that is compressed into a hard porous white material in a proprietary procedure (Goldstein et al. 1999). These panels are very durable, hydrophobic, and have very high reflectance values across a broad range of the electromagnetic spectrum, from approximately 250-2,500 nm, which makes them excellent calibration targets for optical sensors. A Spectralon panel approximately 0.5 by 0.5 m was installed ~8 meters from and orthogonal to the TLS on a tree (Figure 5).

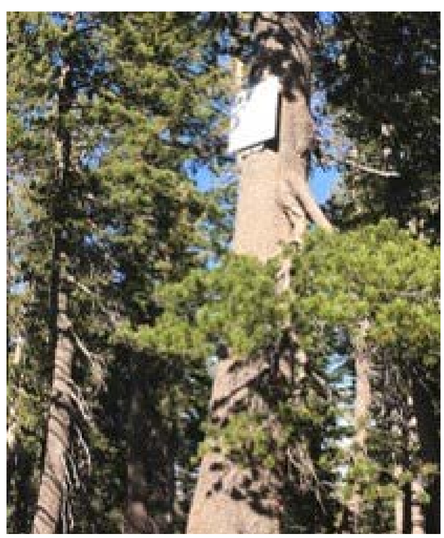

Figure 5: Spectralon panel installed at Sesame site.

Figure 6 shows typical reflectance values for a 99% Spectralon panel. The dotted line represents the wavelength of the TLS system used in the study (described in Section 2.2). The calibration report of the Spectralon panel used in at Sesame can be found in Appendix A. Examining lidar points returned from the Spectralon panel during snowfall events may show a reduction in intensity that could be correlated to the intensity of snowfall or visibility.

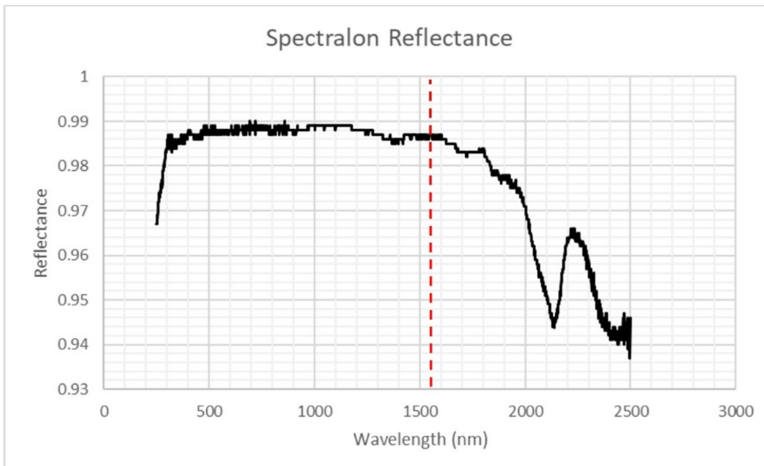

Figure 6: Typical reflectance for a 99% Spectralon panel.

2.2. Riegl VZ-400

The TLS system installed at Sesame is the Riegl VZ-400 (Figure 7), a single, near-infrared laser system capable of FW and multiple-return pulse-based data capture. The conditions at Sesame drop below the instrument recommended operating temperature, so a special housing was designed to heat and protect the instrument. The VZ-400 is able to scan 360° horizontally with a 100° vertical field-of-view. Some of the instrument's specifications can be seen in Table 1. The maximum range assumes that the target is larger than the illuminated laser beam area and that the target material has a high reflectance value for the given laser wavelength. This will not be applicable

Figure 7: Riegl VZ-400 in protective housing unit at Sesame.

Table 1. Riegl VZ-400 specifications.

Sensor Specifications	
Diameter	180 mm
Length	308 mm
Weight	9.6 kg
Standard Temperature Operation	0-40°C
Max Laser Pulse Repetition Rate	300 kHz
Max Measurement Range	600 m
Min Angular Resolution	0.0024°
Laser Wavelength	1550 nm
Laser Beam Divergence	0.3 mrad
Accuracy	5 mm
Precision	3 mm

to hydrometeors as they are much smaller than the laser beam area and have a relatively low reflectance at 1550 nm. Since materials have different reflectance properties at different wavelengths, it is important to consider the wavelength in use. Figure 8 (Deems et al. 2013) shows the varying reflectance values of snowpack with different snow particle sizes for common wavelengths used in laser systems. The low spectral albedo for snow in the 1550 nm wavelength means that not much of the laser energy will be reflected back to the sensor. Note that these are measurements of a snow surface on the ground and not individual particles.

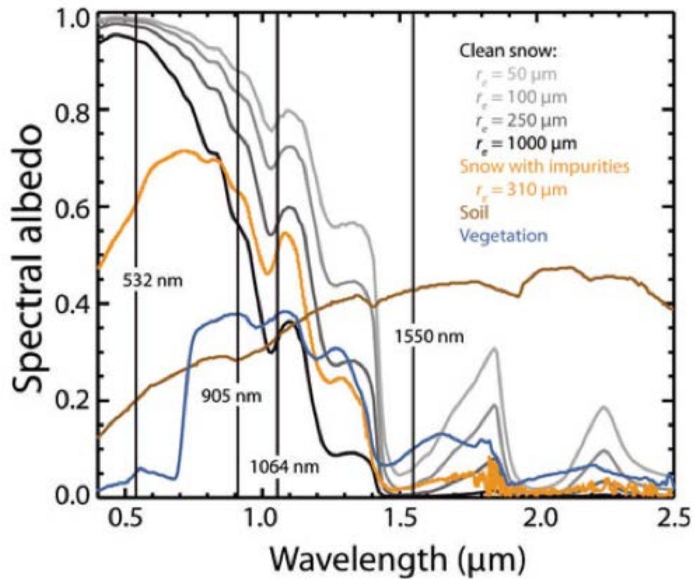

Figure 8: Spectral reflectance properties for snow (Deems et al. 2013).

The VZ-400 is capable of scanning the laser in two different modes, frame scan and line scan, both of which will be used for collecting data in this study. For a frame scan, the instrument rotates about its vertical axis to collect returns of the surrounding area. The instrument does not rotate for a line scan, but collects data from a fixed orientation for a predetermined amount of time. The sensor captures a time series of reflected intensities, which is what constitutes FW data. The VZ-400 digitizes the backscattered laser pulse energy at a 500 MHz (2-ns) sampling rate (Hartzell et al. 2014).

The V-line series of Riegl scanners employs an onboard processor to analyze the FW data in real-time and determine the corresponding target ranges for each laser pulse. For every target identified from an incoming digitized echo signal, the corresponding amplitude and temporal position with respect to the emitted laser pulse is determined by applying a 2-dimensional optimization algorithm (Pfennigbauer and Ullrich 2010). The V-line series online processing is also used to calibrate the amplitude, give a relative reflectance and calculate a pulse-shape deviation for every determined target. Amplitude calibration is a logarithmic ratio of the echo return power over a device-specific detection threshold for the entire measurement range of the instrument. The relative reflectance accounts for the range dependency and is the ratio of the amplitude of an identified target to the amplitude of a flat, white target at the same range. This calibration, known as the system response, is done for the entire operating range of the sensor and is utilized in real-time when the instrument is collecting data (RIEGL Laser Measurement Systems Gmbh 2017). Each target is compared with the expected system response to determine its pulse shape deviation. As the target varies from that of the system response, the pulse shape deviation increases. The TLS can record only the multi-return targets or also include the FW data; however, all of the measurements are derived from the FW results.

Intensity is a term that frequently gets used interchangeably for both amplitude and relative reflectance. It is a dimensionless unit that is arbitrarily scaled by the instrument and depends on both sensor and target properties. Figure 9 shows both amplitude and relative reflectance collected by the TLS located at Sesame. The foliage and snow show how amplitudes diminish at farther ranges. The relative reflectance is the sensors attempt to correct for this range dependence. All intensities reported herein will be of the relative reflectance unless otherwise noted.

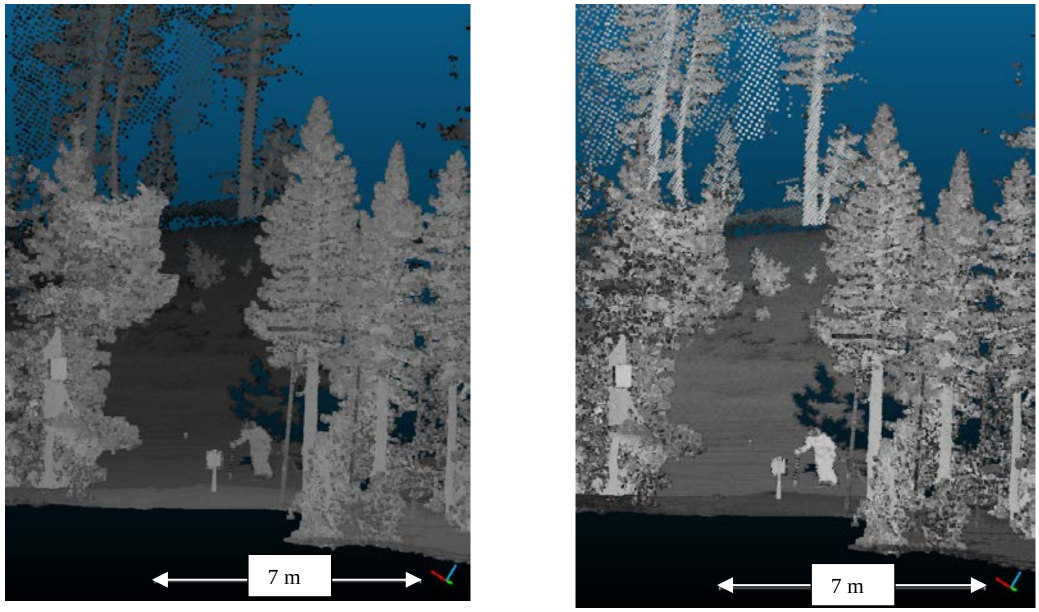

Figure 9: Intensity values from amplitude (left) and relative reflectance (right) of a frame scan.

Figure 10 shows the amplitude output of a VZ-400 when measuring a calibration target from 1 to 50 meters. A least squares cubic spline is fit and extrapolated from 50 to 1000 meters assuming $1/R^2$ amplitude decrease, based on the laser radar range

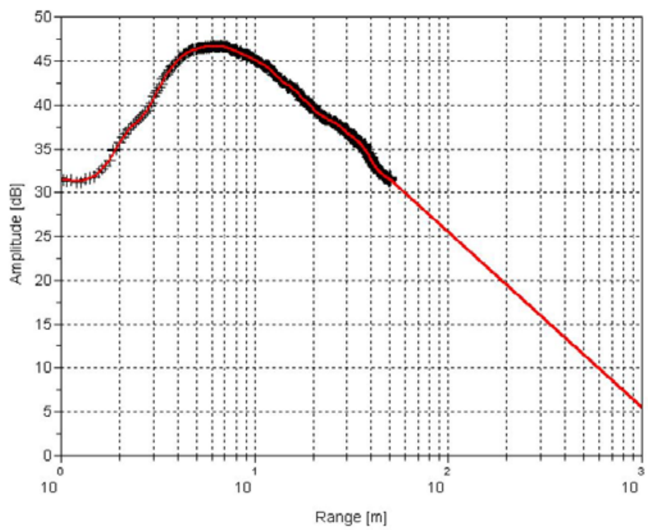

Figure 10: VZ-400 amplitude return ranges from a calibration target (Pfennigbauer and Ullrich 2010).

equations (P.W. Wyman 1969). The $1/R^2$ inverse-square law is only applicable for ranges greater than 20 m, as the amplitude drops about 20 dB per decade in range. "In the far-field the amplitude of the echo from a large diffusely reflecting object usually follows the $1/R^2$-law from the laser radar range equations when neglecting the atmospheric attenuation, the characteristics in the near field is more complex due to vignetting or central obscuration, depending on the specific optical setup of the instrument. The range of transition between near-field and far-field also depends on the optical setup; it is, for example, considerably larger for biaxial systems than for coaxial systems." (Pfennigbauer and Ullrich 2010) It is suspected that these physical configurations and characteristics will affect the scanner's ability to detect laser energy returning from hydrometeors in both the near and far field. The Spectralon panel located approximately 8 m away is considered to be in the transition region and the TLS will have no issue getting point returns from the panel. However, the laser pulse travels through very little atmosphere before reaching the panel which may limit the intensity reductions observed due to snowfall.

2.3. OTT Hydromet Parsivel^2 Disdrometer

In 2000, PM Tech Inc. released the first commercially available optical disdrometer, Parsivel (Particle Size and Velocity), and these were included in many precipitation studies in the following years (Löffler-Mang and Blahak 2001, Yuter et al. 2006, Tokay 2013). OTT Hydromet, a German based company, purchased the rights to the Parsivel in 2005. They redesigned and improved the instrument with knowledge from past performance and released a second version of the instrument in

2011, the OTT Parsivel^2 disdrometer, which collected measurements at the Sesame site and will be referred to as PD (Parsivel^2 Disdrometer). It provides estimates of hydrometeor size, speed, visibility and snowfall intensity, which are provided through proprietary algorithms that are not accessible.

The PD uses a 180 x 30 mm, 650 nm wavelength laser-optical sensor that is emitted and received by the two sensor heads, shown in Figure 11. Microprocessor controlled heating within the instrument provides de-icing protection making the sensor very durable with little need for maintenance, which is ideal for continuous remote observations. It has the ability to classify precipitation by type (drizzle, rain,

Figure 11: OTT Hydromet Parsivel^2 Disdrometer (OTT Hydromet).

snow, etc.) and categorize 32 classes of size and speed ranging from 0.2-25 mm and 0.2-20 m/s respectively. These classifications are based upon an extinction principal of the particle passing the optical plane of the sensor. The amount of dimming of the received signal is utilized to derive the size, velocity and type of the hydrometeor (Figure 12).

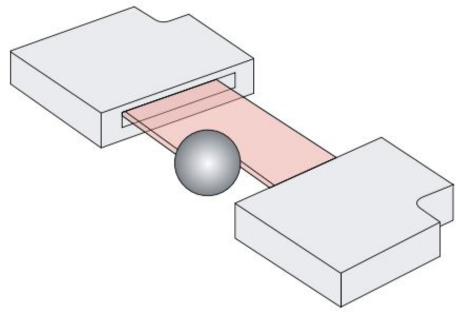

Figure 12: Extinction illustration (OTT Hydromet).

Battaglia et al. (2010) performed a critical assessment of Parsivel snow observations. The instrument's measuring principle was reexamined to detect limitations when applied to solid precipitation. The study used co-located data from two Parsivel disdrometers and a two-dimensional video disdrometer acquired during the Cloud-Aerosol Lidar and Infrared Pathfinder Satellite Observation, CALIPSO, Validation Project. Only one size parameter is estimated from the PD, namely, an equivalent volume diameter of a sphere. Reduced output voltage from the PD is converted to the size estimate using a few assumptions. The PD assumes that: particles have an oblate spheroid raindrop like shape, only one particle is crossing the laser beam at a time and that particles are falling with their axis vertically aligned. Additional assumptions are made for the particle shape based on the size estimate and these assumptions become arbitrary when applied to solid precipitation. Based on their studies, Battaglia et al. found that for solid precipitation 5 mm and larger, the derivation of widest horizontal dimension from the equivalent volume diameter to be quite accurate. Larger uncertainties exist for smaller particles caused by unknown shape and orientation. Figure 13 gives a visual example of different particle sizes being recorded by a Parsivel disdrometer.

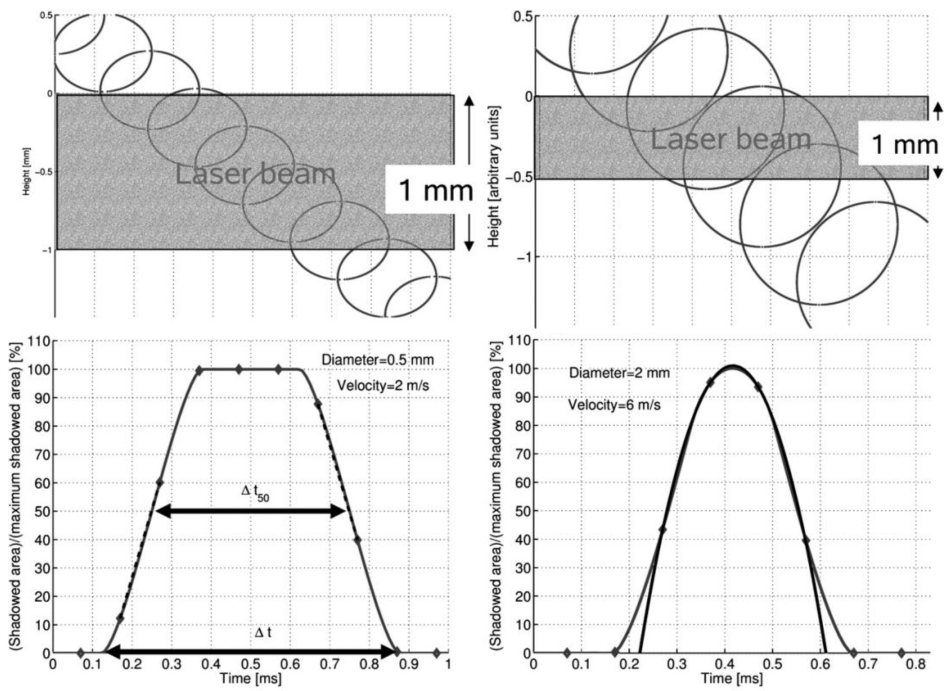

Figure 13: Results from Parsivel measurements (Battaglia et al. 2010).

The particle velocity is related to the beam dimming amplitude and duration (Angulo-Martínez et al. 2018). “The comparison between the PARISVEL simulated and measured data shows a PARSIVEL underestimation of fall velocities for small particles and an overestimation for large particles (up to 30% - 40%). The accuracy of snow velocity measurements does not fulfill the requirements needed to develop snow velocity parameterizations.” (Battaglia et al. 2010) The PD assumptions favor liquid-phase precipitation characteristics and irregularities of hydrometeor shape, orientation and the presence of wind can affect the measurements of solid precipitation.

2.4. Snow Pillow

The California Department of Water Resources installed a snow pillow designed to measure the weight of overlaying snowpack at the Sesame site in 2013 (Bair et al. 2018). Snow pillows constrain snowpack density, and improve accuracy of SWE estimates. The snow pillow is so close to the TLS that it is not within the scanning range of the sensor, however, nearby snow elevations should be equivalent and approximate the same relative density (density of the snowpack divided by the density of water) for the snowpack.

2.5. Lufft WS600-UMB Smart Weather Sensor

The WS600 is a compact all-in-one sensor capable of measuring temperature, relative humidity, precipitation intensity, wind speed and direction. The sensor uses a Doppler radar to estimate precipitation rates using a mass fall speed relationship. Although the sensor performs well for liquid precipitation, estimated accuracy for snow remains low (Bair et al. 2018). This sensor will be utilized to help characterize the weather conditions during TLS scans.

Figure 14: WS600-UMB smart weather sensor (Lufft).

2.6. Judd Ultrasonic Depth Sensor

The Judd Ultrasonic Depth Sensor (JUDS) is a device that measures the snow surface height by measuring the travel time for an ultrasonic pulse to reflect off the snow surface. The sensor is located directly above the snow pillow at the sesame site and will be used for calculating the relative density of the snowpack. The accuracy for the sensor is +/- 0.4%, which results in a maximum 2.5 cm uncertainty for the nominal Sesame snowpack.

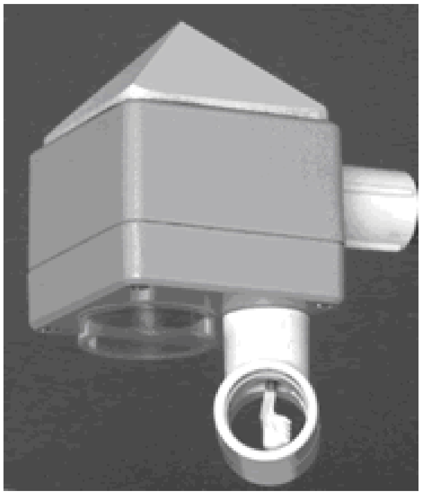

Figure 15: Judd ultrasonic depth sensor (Judd Communications).

3. METHODS

3.1. TLS Lidar

3.1.1. VZ-400

The TLS system was installed at the Sesame site in September of 2019. The laser scanner was programmed to take a frame scan every hour (Figure 16). After a frame scan is collected, a programmed script analyzes the point cloud and checks if there are laser returns in two predetermined 1-m^3 volumes above the ground. In order to classify a scan as a snowfall event, a threshold of 15 returns are needed in both sample

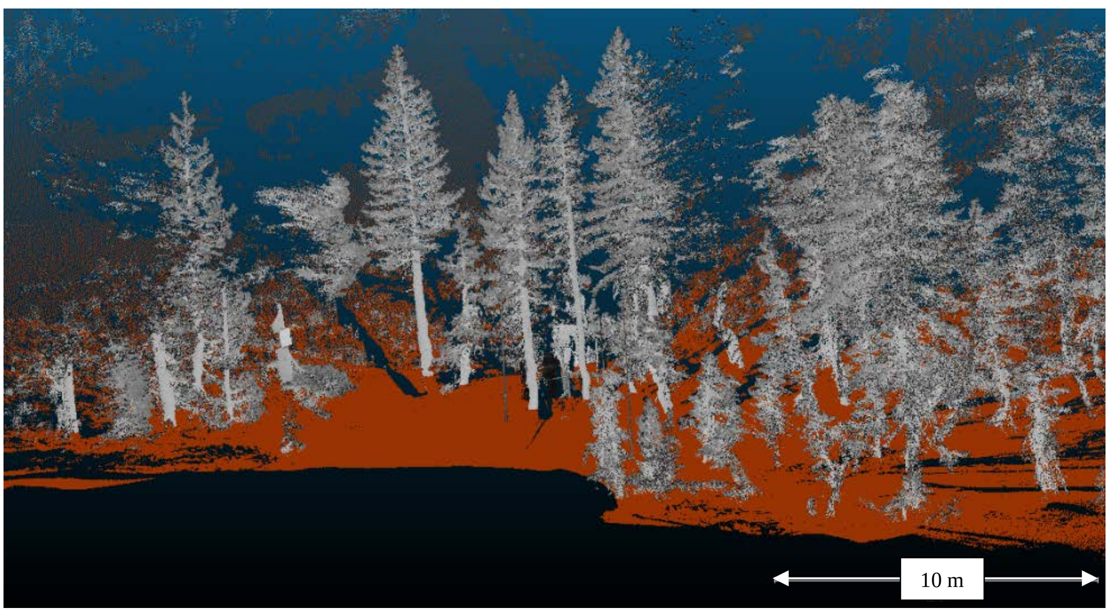

Figure 16: Frame scan collected before snow season with ground (brown) and tree (grey-scaled intensity) returns.

volumes. If the frame scan identifies a snow event, the laser then proceeds to collect a single vertical line scan for approximately 30 seconds. The direction of the line scan was oriented vertically with minimal tree interference. After February 21st, 2020, an additional script was added to collect a second line scan that intersects the Spectralon panel. The scanner settings for the various scans are provided in Table 2. The original line scan has a 100° vertical angle range and with a 0.04° resolution equals 2,500 measurements per line scan cycle. For 100 kHz sampling rate, a cycle happens approximately 40 times per second or 1,200 times for the 30-second duration. Figure 17 shows a frame scan with both the original line scan and the Spectralon line scan.

*Table 2. TLS settings for different data collections. *Frame scan settings were adjusted midway through the season*

	Pulse Repetition Rate (kHz)	**Vertical Angle Range**	**Vertical Angle Resolution**	**Point Spacing at 10 m (mm)**	**Horizontal Angle Range**	**Horizontal Angle Resolution**	**Duration (sec)**
Frame Scan	100	50-130°	0.08°, 0.04°*	7	110-280°	0.04°	38, 87*
Line Scan	100	30-130°	0.04°	7	195°	-	30
Spectralon Line Scan	100	115-125°	0.02°	3.5	276°	-	30

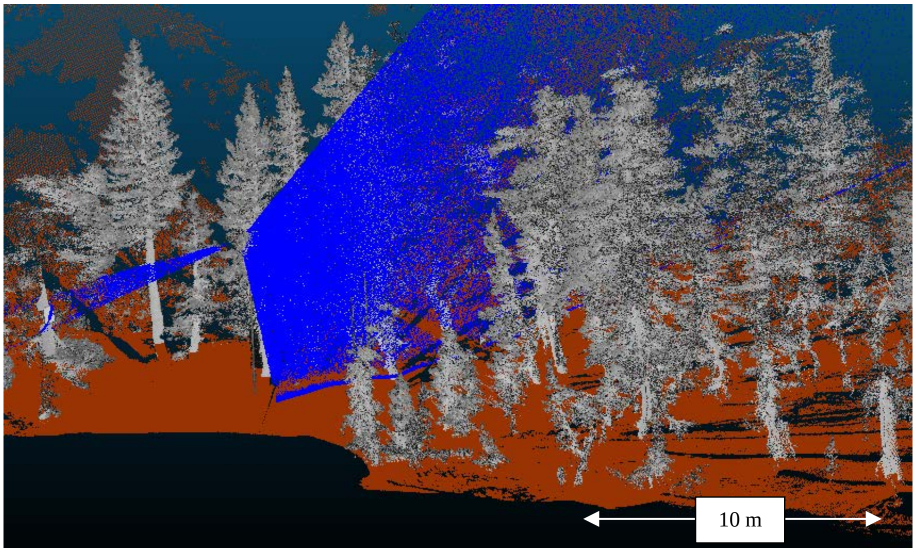

Figure 17: Frame scan with ground (brown) and tree (grey-scaled intensity) returns overlaid with both line scans (blue).

FW lidar scans were only collected until December 12, 2019, because discontinuing the FW data collection would reduce file size of the point clouds and ease bandwidth demands for uploading data. However, for the entire collection period, each lidar scan records the X, Y, Z position, the calibrated amplitude, relative reflectance, pulse deviation, time stamp, pulse return number and the total number of returns acquired for every laser pulse. In total, over 5000 frame scans were collected from September 2019 to June 2020. From those frame scans, the automated hydrometeor detection process identified 335 snowfall events (Figure 18). Of the 335 identified events, 59 were marked as discrepant due to the disdrometer and other instruments not clearly indicating it was snowing at the time (discussed later in Section 4.5).

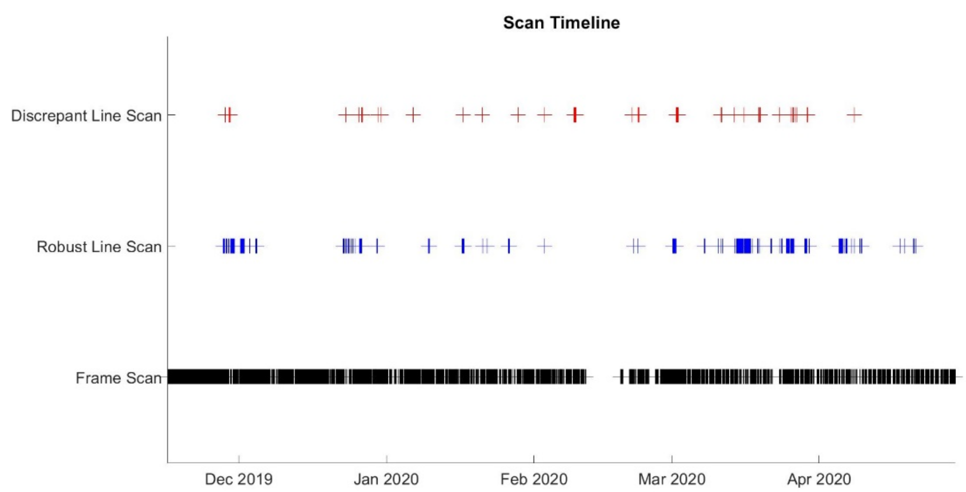

Figure 18: Timeline of data acquisitions. Blue depicts confirmed snow events, red depicts discrepant snow events and black depicts a frame scan.

There were instances where the TLS failed to collect a frame scan causing small data gaps due to an error indicating an overloading current occurred. The TLS' firmware was never updated after the protective housing was installed, so the additional weight of the housing occasionally overloaded the frame rotation motor. An extended power outage also produced a long data gap in mid-February 2020.

Figure 19 shows a scaled reference of sizes involved in the collection process for snowflakes, laser beam footprints and the disdrometer sampling area. Most of the PD size estimates were between 1-5 mm and the TLS ranges from the line scans reach about 75 meters. This illustrates the difficulty for smaller snowflakes to backscatter enough laser energy to be detected as a target return at larger ranges.

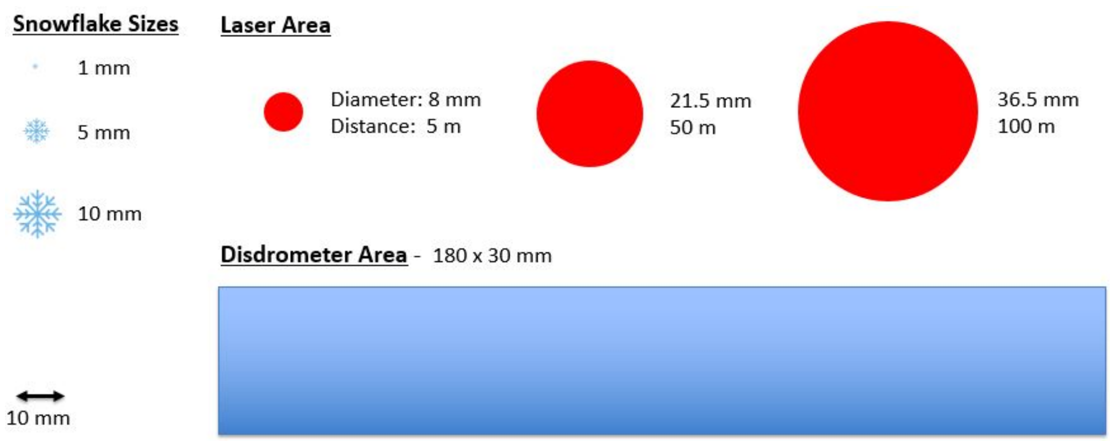

Figure 19: Size reference for data collection.

3.1.2. Data Processing

All of the lidar point clouds were georeferenced to the Universal Transverse Mercator (UTM) zone 10 N reference frame (EPSG number 32610), stored as a compressed .laz file and uploaded to an Amazon Web Services simple storage service bucket after they were acquired. Time was recorded in Coordinated Universal Time (UTC) and time forms the basis of the lidar file naming convention.

First, the georeferenced line scans were transformed back to the Scanners Own Coordinate System (SOCS), so that the raw range and angle relative to the scanner origin could easily be computed for each point. A 4 x 4, Project Orientation and Position (POP), transformation matrix (equation 1) was applied to convert coordinates from UTM back to World Geodetic System 1984 (WGS 84),

$$POP = \begin{bmatrix} 0.874268495900 & -0.485442681556 & 0.000000000000 & 0.000000000000 \\ 0.296522721271 & 0.534029007700 & 0.791762145284 & 20675.785437908489 \\ -0.384355138961 & -0.692212699869 & 0.610829522285 & -6370166.497704507783 \\ 0.000000000000 & 0.000000000000 & 0.000000000000 & 1.000000000000 \end{bmatrix} \quad (1)$$

utilizing the Point Data Abstraction Library (PDAL) in python. This matrix contains a 3D-rotation matrix and a translation vector. Equations 2, 3, and 4 show the rotation matrices for the X, Y, and Z-axes respectively as follows:

$$R_x(\omega) = \begin{pmatrix} 1 & 0 & 0 \\ 0 & \cos(\omega) & \sin(\omega) \\ 0 & -\sin(\omega) & \cos(\omega) \end{pmatrix}, \quad (2)$$

$$R_y(\varphi) = \begin{pmatrix} \cos(\varphi) & 0 & -\sin(\varphi) \\ 0 & 1 & 0 \\ \sin(\varphi) & 0 & \cos(\varphi) \end{pmatrix}, \quad (3)$$

and

$$R_z(\kappa) = \begin{pmatrix} \cos(\kappa) & \sin(\kappa) & 0 \\ -\sin(\kappa) & \cos(\kappa) & 0 \\ 0 & 0 & 1 \end{pmatrix}. \quad (4)$$

The final rotation matrix, which is a matrix multiplication of the three axes rotations $M = R_z(\kappa)*R_y(\varphi)*R_x(\omega)$, is shown in its extended form

$$M = \begin{pmatrix} \cos(\kappa)\cos(\varphi) & \cos(\omega)\sin(\kappa) + \cos(\kappa)\sin(\omega)\sin(\varphi) & \sin(\kappa)\sin(\omega) - \cos(\kappa)\cos(\omega)\sin(\varphi) \\ -\cos(\varphi)\sin(\kappa) & \cos(\kappa)\cos(\omega) - \sin(\kappa)\sin(\omega)\sin(\varphi) & \cos(\kappa)\sin(\omega) + \cos(\omega)\sin(\kappa)\sin(\varphi) \\ \sin(\varphi) & -\cos(\varphi)\sin(\omega) & \cos(\omega)\cos(\varphi) \end{pmatrix}. \quad (5)$$

The rotation angles ω, φ, κ that rotate the points about their respective X, Y, Z, axes can be determined with some simple trigonometry from the final rotation matrix shown by the following equations:

$$\omega = tan^{-1}(-M_{32} / M_{33}), \tag{6}$$

$$\varphi = sin^{-1}(M_{31}), \tag{7}$$

and

$$\kappa = tan^{-1}(-M_{21} / M_{11}). \tag{8}$$

Note subscripts are row and column locations within the final rotation matrix. A 4 x 4 matrix is needed to transform 3D coordinates, because it is necessary to translate the coordinate positions in addition to applying the axes rotations. The translation vector, T, is simply appended to the end of the rotation matrix as shown in equation 9,

$$\begin{bmatrix} x' \\ y' \\ z' \\ 1 \end{bmatrix} = \begin{bmatrix} M_{11} & M_{12} & M_{13} & T_x \\ M_{21} & M_{22} & M_{23} & T_y \\ M_{31} & M_{32} & M_{33} & T_z \\ 0 & 0 & 0 & 1 \end{bmatrix} * \begin{bmatrix} x \\ y \\ z \\ 1 \end{bmatrix}. \tag{9}$$

The Sensor's Orientation and Position (SOP) transformation is applied to convert the WGS 84 coordinates back to the SOCS

$$SOP = \begin{bmatrix} 0.243466990948 & 0.834583002822 & 0.494160940895 & -1371.356756454145 \\ -0.958570643796 & 0.284725256939 & -0.008593455998 & -7.178285891526 \\ -0.147872052968 & -0.471595948900 & 0.869327968815 & -2362.346996182266 \\ 0.000000000000 & 0.000000000000 & 0.000000000000 & 1.000000000000 \end{bmatrix}. \tag{10}$$

Note that these transformation matrices are the inverse of the original transformations applied to the point clouds. The inverse of a 4 x 4 matrix can be calculated with Gauss-Jordan elimination or by use of the adjugate matrix. All points and metadata were then output as comma-separated values (CSV) files so that they could be read into Matlab for further analysis and classification.

The next step was classifying whether or not each point from the line scans are hydrometeors. The maximum range is calculated for a series 0.05° angle bins across the entire vertical range of the line scan. The maximum range of each angle bin is considered to be in a static position and is therefore not a hydrometeor. This accounts for the changing snow elevations and trees observed in the line scan. All point ranges in a given angle bin are then compared to its maximum range and other conditional statements to classify points as a hydrometeor or not. A pseudocode for hydrometeor classification is shown as

```
if Point Return(Range) < Max Range - 0.5 meters AND
Point Return(Range) < 73 meters OR Point Return(Angle) > -47.5°
then
Point Return = hydrometeor;
else
Point Return = not hydrometeor;
end.
```
(11)

Figure 20 - Figure 22 demonstrate the performance of the classification process. The algorithm misclassifies points when there are little or no points collected from the tree in the background, approximately 75 m away. There were only a few events that were poorly classified, like the line scan taken on January 17 2020 (Figure 22).

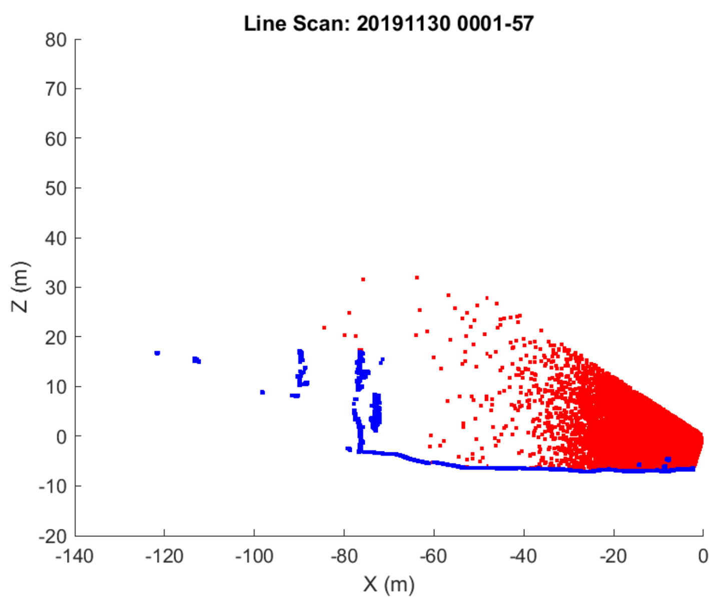

Figure 20: Good line scan classification - hydrometeors (red) and non-hydrometeors (blue).

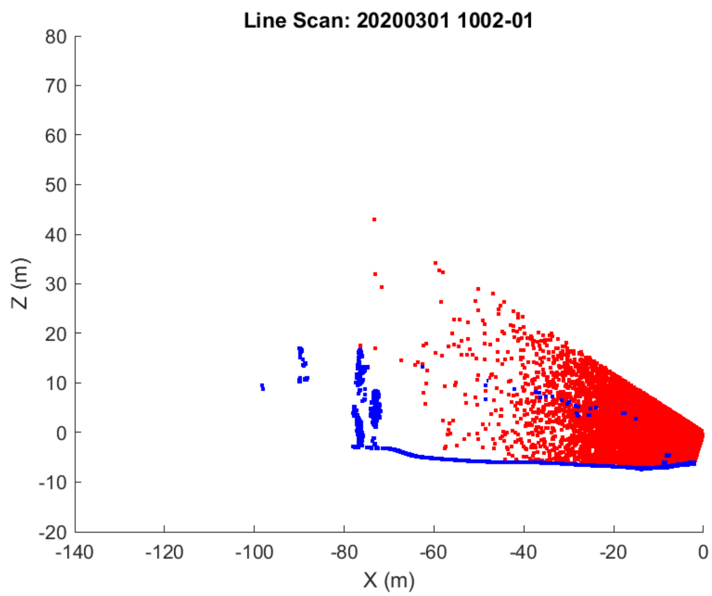

Figure 21: Few line scan misclassification - hydrometeors (red) and non-hydrometeors (blue).

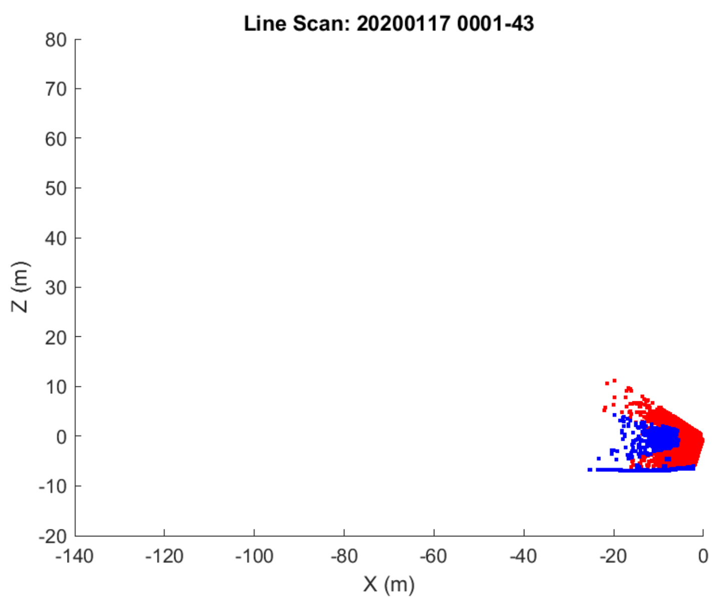

Figure 22: Many line scan misclassification - hydrometeors (red) and non-hydrometeors (blue).

The poorly classified line scan in Figure 22 was reprocessed with additional conditional statements to correct the misclassified point returns. The original classification classified 292,098 hydrometeors and after the correction only 864 points were added, which equates to 0.3% of the observations made. Figure 23 shows the corrected line scan plot. Note the few blue points remaining in the scan are branches from nearby trees. These do contribute false positive misclassifications of hydrometeors when an angle bin is able to penetrate through the branches and reach the ground surface. These misclassifications will be shown in the range scan histograms in Section 4.1.3 and should be taken into consideration when evaluating results derived from the line scans. Statistics for the presented line scans can be found in Table 3.

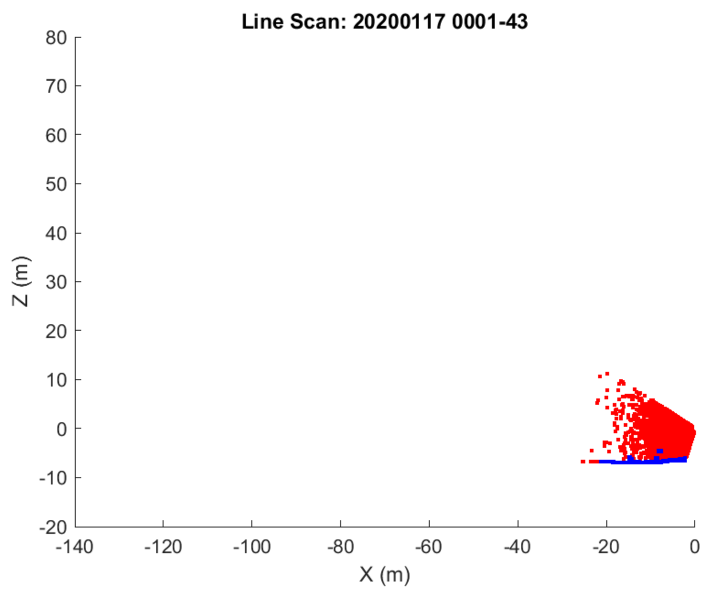

Figure 23: Corrected line scan classification - hydrometeors (red) and non-hydrometeors (blue).

Table 3: Hydrometeor count and corrections of presented line scans.

	Original Classified Hydrometeors	Corrected Classified Hydrometeors	% Increase
Figure 20	73,114	-	-
Figure 21	130,260	130,287	0.02
Figure 22	292,098	293,004	0.31

3.2. Target Statistics

Statistics were examined for different targets located within the frame scan. The Spectralon panel was installed near the TLS at the beginning of the snow season, but was only sampled with its own specific line scan starting at the end of February 2020, which resulted in 115 datasets captured during snowfall events that aligned with the original line scans. Since the Spectralon panel appears in every frame scan, additional processing extracted the return points from the Spectralon panel for all of the frame scans, including events not identified with snowfall. Additionally, returns from a tree trunk approximately 16 meters away were also extracted. Location of the tree trunk in relation to the frame scan and Spectralon panel can be seen in Figure 24. Comparison of return behavior for both a calibrated and natural target during hydrometeor events will indicate feasibility of utilizing natural targets located in the environment surrounding the TLS for modeling purposes.

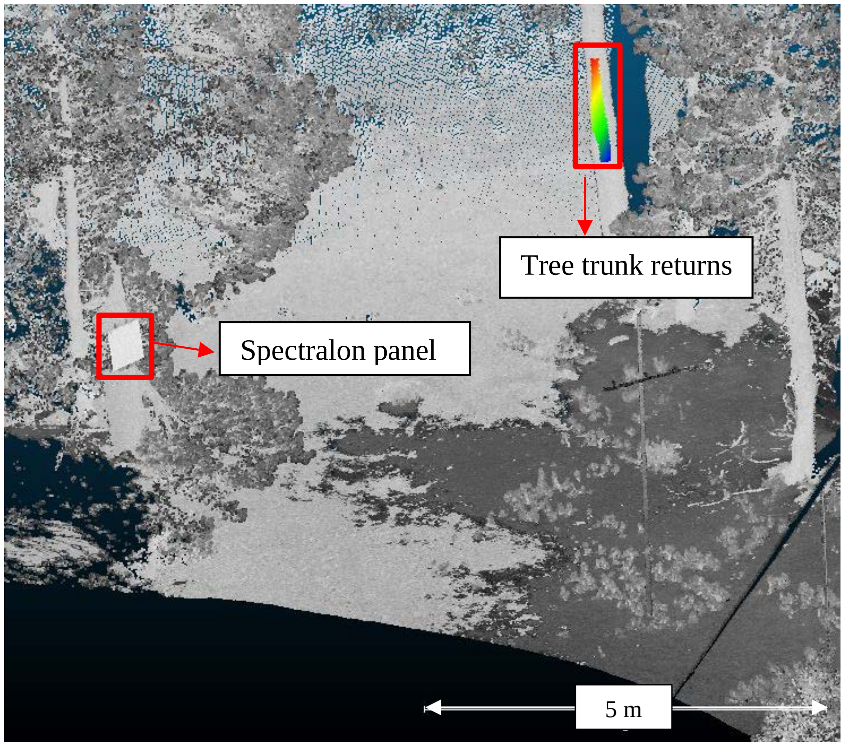

Figure 24: Location of returns examined from the Spectralon panel and tree trunk.

3.3. Disdrometer Data

The PD was configured to record observations every minute resulting in 350,000 records from September 2019 to May 2020. Since the PD logged data in local time, all time stamps were adjusted to UTC to match the lidar data. PD outputs include particle size, speed, snowfall intensity rate and the visibility metric Meteorological Optical Range (MOR).

The WMO classifies MOR as the length of path in the atmosphere required to reduce the luminous flux in a collimated beam from an incandescent lamp, at a color temperature of 2,700 K, to 5 % of its original value (WMO 2008). The PD estimates MOR with a range from 0 – 20,000 meters. Visibility is computed based on the reduction of laser intensity on the receiving sensor and does not exclusively use hydrometeor observations in the process, i.e., reduced visibility can be measured without the presence of hydrometeors. OTT has not conducted validation experiments to evaluate accuracy of MOR estimates (OTT Hydromet customer support, personal communication, October 27, 2020). Snowfall intensity rate is estimated as millimeters per hour with a +/-20% accuracy and is derived from the observed particle extinctions.

A batch process was executed in Python utilizing the Pandas library, creating an accompanying CSV dataset for each line scan that includes PD data 5 minutes before and after the line scan was collected to observe variations in sensor observations and weather conditions. Figure 25 shows an example of the number of hydrometeors that were classified per cycle of a line scan and the PD intensity rates for both liquid and solid precipitation. Precipitation phase is determined from particle size and speed estimates, so solid precipitation can be misclassified on occasion. Large variations were observed for both the laser line scans and disdrometer datasets, which shows how quick conditions can change (Figure 25). Figure 26 and Figure 27 show a more consistent example and one of the discrepant scans respectively.

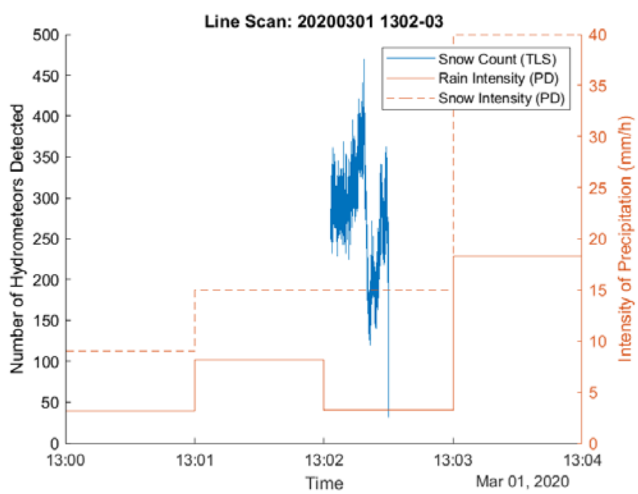

Figure 25: TLS snow count with disdrometer intensities – large variations.

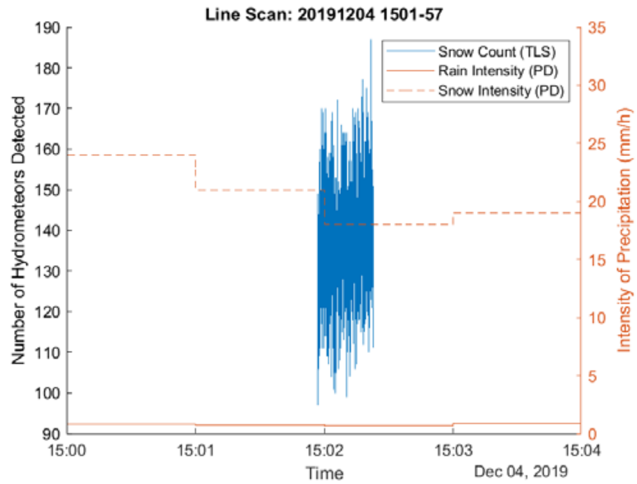

Figure 26: TLS snow count with disdrometer intensities – small variations.

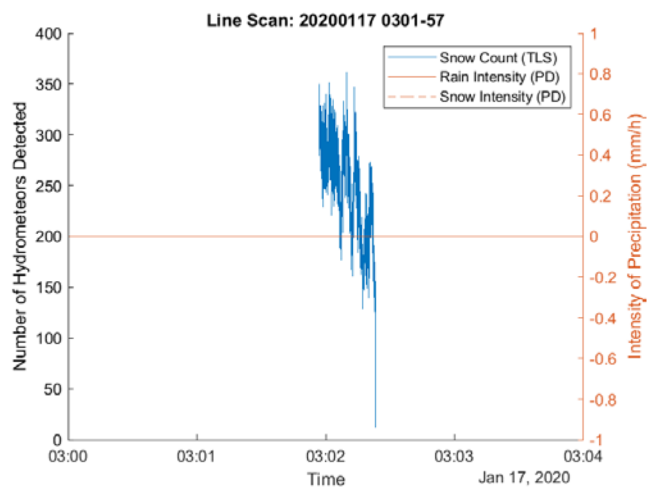

Figure 27: TLS snow count with disdrometer intensities – discrepant scan.

3.3.1. Hydrometeor Size and Velocity

The PD estimates hydrometeor size and fall speed for every detected particle during a collection interval. Output is organized as a 32 x 32 matrix with different size and speed classes in which the particles are binned. Total counts and median values were calculated for each matrix (Figure 28-Figure 29). The one-minute median

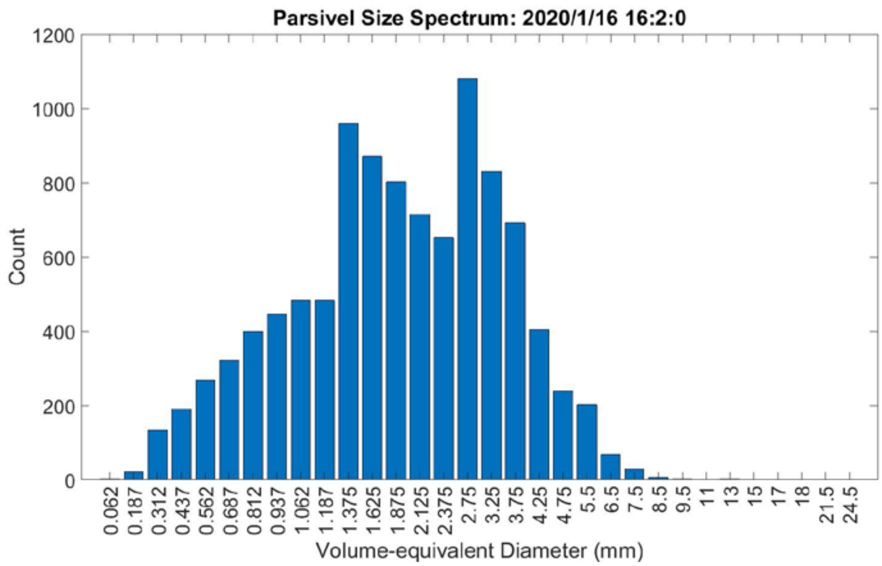

Figure 28: Example of estimated particle size count from disdrometer.

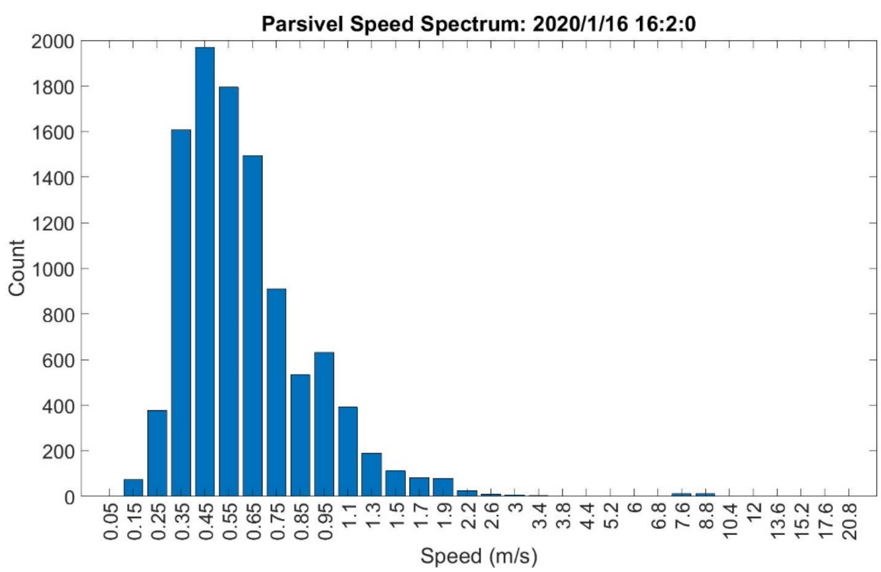

Figure 29: Example of estimated particle speed count from disdrometer.

disdrometer size, MDS, was examined in attempt to identify patterns in the TLS data collection and is presented in Section 4.7.

An attempt to measure particle velocity was made by comparing the speed estimates from the PD with estimates made from the TLS point clouds by using the differences in time and displacement for what was believed to be measurements of the same hydrometeor. This analysis was conducted in CloudCompare (www.danielgm.net/cc/), which is a free open-source program used for analyzing point clouds. Co-linear points that appear as streaks within the scan are suspected to be repeat measurements of the same particle (Figure 30). Note that the point streaks are not necessarily the actual path the hydrometeor travels. Point returns are assigned coordinates at the center of the laser footprint, regardless of where the return energy originates from within the laser beam. Therefore, these streaks are likely sequential observations of a particle and only depend on the range of the returned energy.

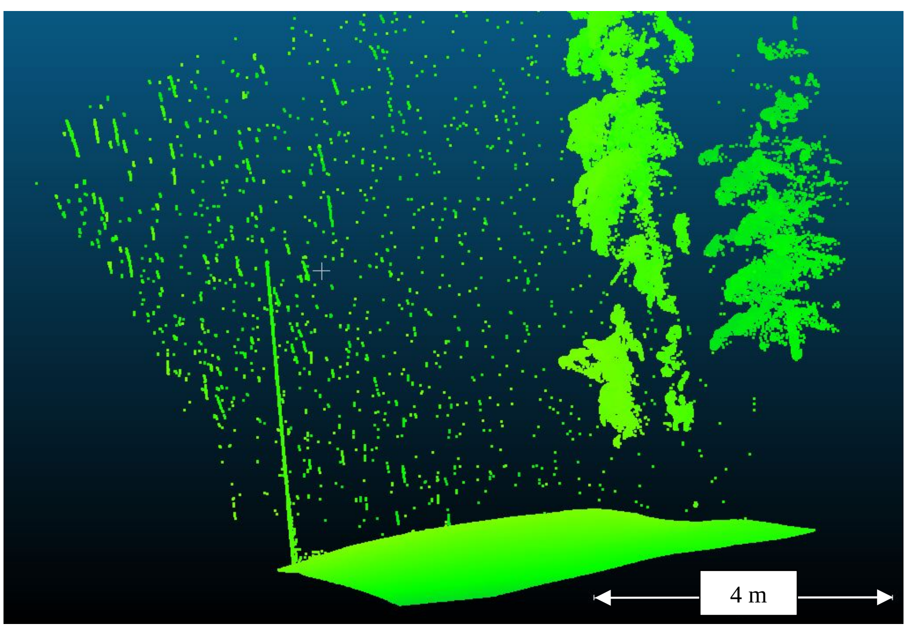

Figure 30: Example of point streaks from hydrometeors in a section of the frame scan.

A frame scan with point streaks, shown in Figure 31, was selected to compare with the PD estimated particle speed measurements. This frame scan was collected on December 23, 2019 at 10 PM. The PD records show this was a light snow event with a rate of 2 mm/h and the WS600 indicates there was very little wind at the time of capture. Note that the obstacles observed within the frame scan are labeled. CloudCompare has a tool that allows geometric features to be computed from a point cloud. This tool estimates geometric features based on arithmetic combinations of eigenvalues and eigenvectors (Hackel et al. 2016). Processing the point cloud based upon linearity, the streaks become more visible as the points surrounding them are filtered out (Figure 32). Further filtering the points that have a strong linearity value over 0.99, reveals the point return streaks of interest (Figure 33). Note the variation in types of streaks as some are well defined with a longer length, whereas other streaks resemble more of a point. All streaks were used to estimate hydrometer velocities from the TLS system and the analysis is presented in Section 4.8.

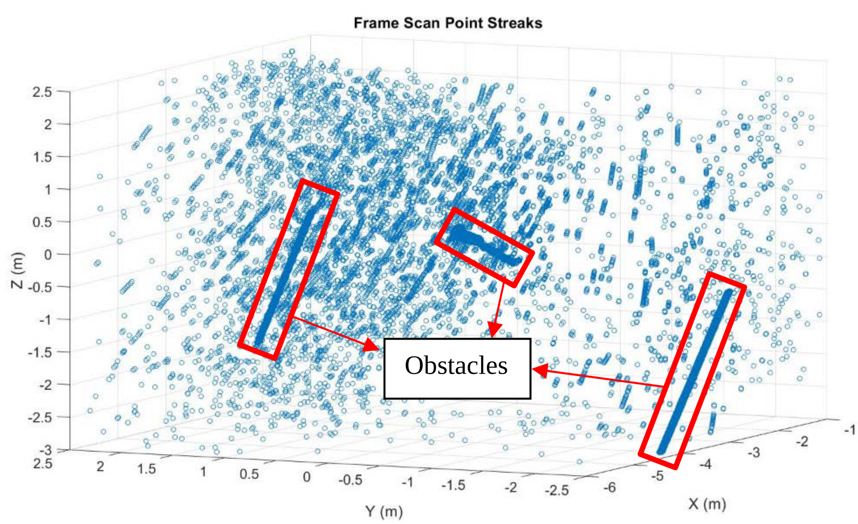

Figure 31: Point returns from a frame scan.

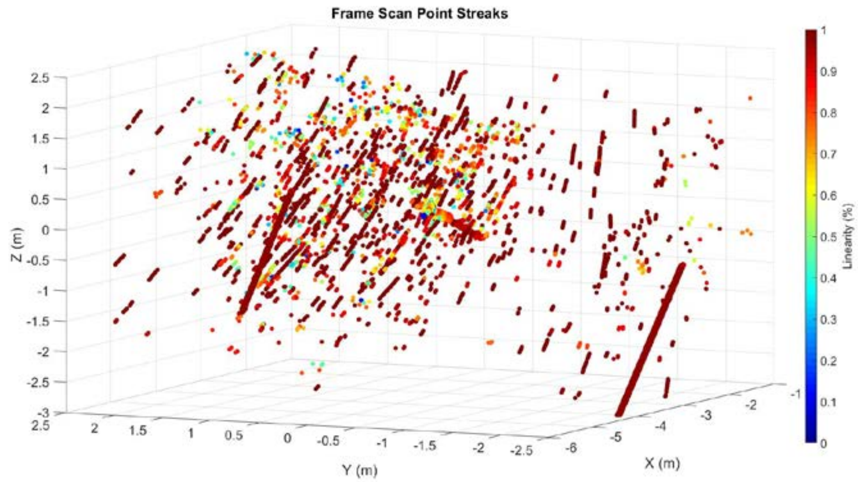

Figure 32: Point streaks from a frame scan classified by linearity.

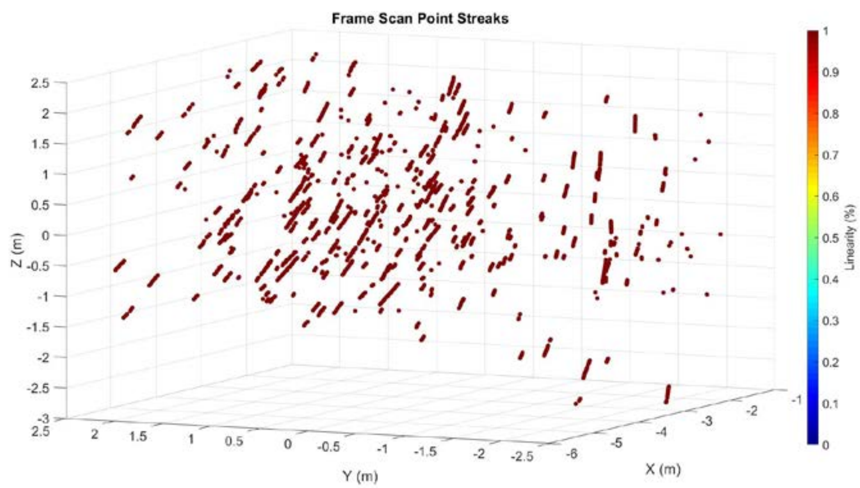

Figure 33: Point streaks from a frame scan with classified linearity values over 99%.

4. RESULTS

In this section, the various statistical relationships observed between the lidar scan metrics and other instruments are presented. The derived measurements from the disdrometer (visibility, snowfall intensity rate, particle size and speed) cannot ultimately be considered as truth, as they are only estimates; there are inherent uncertainties in these measurements and there are no controls in place to validate their estimates. However, instrument performance can be evaluated through comparative analysis, helping to address the science questions given earlier. Therefore, these results are used to characterize the Riegl VZ-400's performance in a DVE and its ability to model estimates derived from the PD.

4.1. Line Scan Statistics

Line scan statistics were calculated from point returns classified as hydrometeors. Point returns were grouped by their echo return number within the pulse, 1st through 4th, and the total number of returns for a given pulse, 1 through 4. Bulk statistics of count, range and reflectance were computed for all of the groupings. This analysis helped determine which statistics had a correlation with snowfall characteristics that could be utilized for modeling purposes.

4.1.1. Count Statistics

Total counts were calculated for all of the groupings. Counts of first echo returns exceed all other returns (Figure 34). On average, the first echo returns have over 170,000 points per line scan. Less than half of the 276 line scans have more than ten third returns and only one line scan has more than ten fourth returns. There are many line scans where neither third nor fourth returns are observed, so these statistical groupings provide little value. Total point returns acquired per laser pulse (Figure 35) shows that most laser pulses acquire two returns. Most second returns come from terrestrial points, not hydrometeors. A table of all count statistics calculated is given in Appendix B.

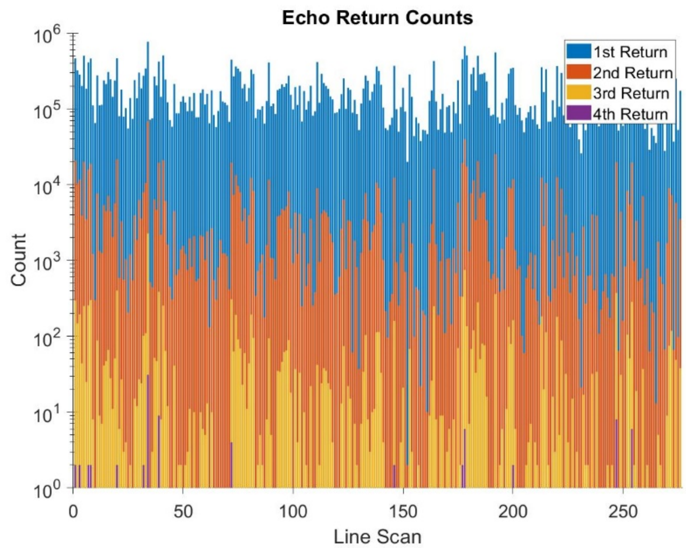

Figure 34: Echo return counts from line scans.

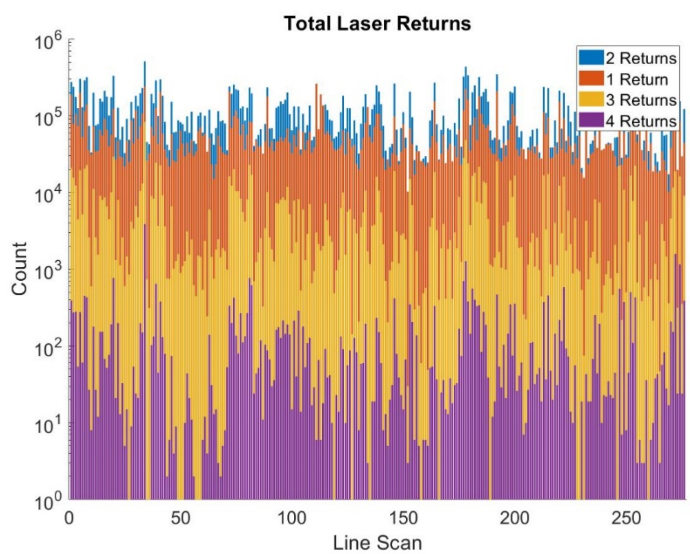

Figure 35: Total laser returns per laser pulse counts.

Another trend observed for the hydrometeor count was the variation in total counts in the near range less than or equal to 5 meters. A bar graph of the near count totals for all of the line scans sorted by magnitude shows that the TLS exhibits an exponential trend for the amount of hydrometeors observed within the first 5 meters (Figure 36).

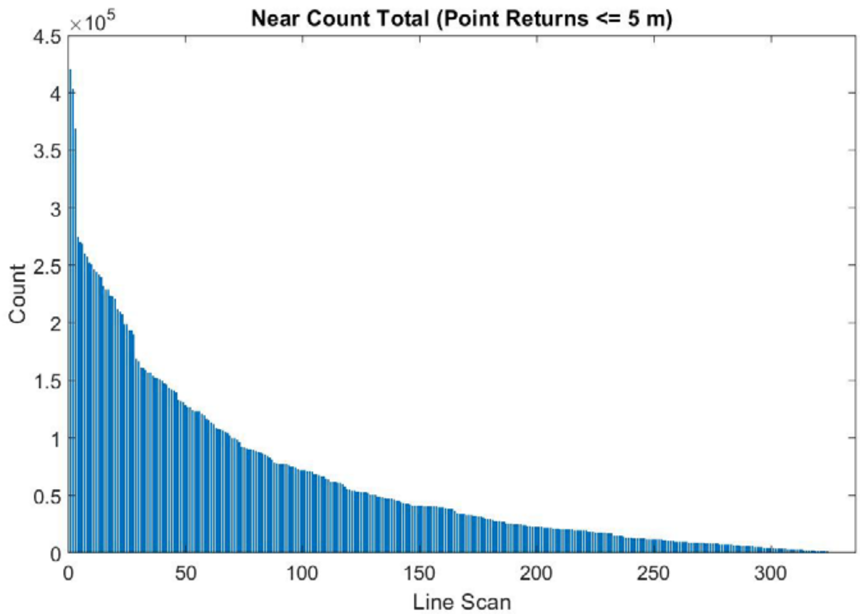

Figure 36: Bar graph of near count totals for TLS line scans.

In the near range, the laser beam will overlap for adjacent pulses, which can result in oversampling of hydrometeors. Bair et al. (2012) developed a sampling theory that estimates sampling efficiency based on range and physical characteristics of the Riegl LMS-Z390i TLS, which has the same laser aperture and beam divergence as the VZ-400, such that results are comparable. From 3-4 meters, the TLS sampling efficiency is estimated to be 1.9 to 1.1 respectively. This means that a hydrometeor at 3 meters is likely to be sampled twice within a scan cycle, due to the laser footprint overlapping between adjacent pulses. However, since snowfall intensity could affect oversampling and there is no way to distinguish when oversampling occurs, no corrections were made and all results were left as bulk observations in effort to keep all TLS observations consistent.

4.1.2. Range and Reflectance Statistics

The minimum, maximum, average and variance of the range and relative reflectance were calculated for each return number grouping. Since there are significantly more first returns from hydrometeors compared with other return values, the average range of first returns were the most informative. The total number of returns per pulse includes all first returns, therefore they do not provide much value or distinction between different line scans. A table of all the range statistics that were calculated can be found in Appendix C.

Similar to the range statistics, the relative reflectance statistical groupings for total number of returns are affected by the first return echoes. In addition, reflectance returns observed after the first return are not expected to be completely accurate due to the unknown reduction in laser energy caused by the first return. Therefore, the inconsistencies in third and fourth return observations rendered these statistics useless for modeling purposes. The reflectance statistics that were calculated can be found in Appendix D.

4.1.3. Range Histograms

Range histograms of classified hydrometeor returns revealed some insights into snow events during line scans. During light snow events, there are large return peaks at around 10 and 18 meters. These peaks are due to false positive hydrometeor classifications within the tree branches that obstruct the line scan. Heavy snow events produced an exponential decay for returns at range from the scanner. In addition, the scanner has difficulty observing hydrometeor targets beyond 30 meters. Figure 37 shows a few range histograms for heavy and light snowfall events. The exponential decay observed for heavy snowfall could be related to the Beer-Lambert Law, which states that the amount of absorption of light is proportional to the length traveled and the concentration of absorbing species (Camps et al. 2017). This law is used for various atmospheric applications.

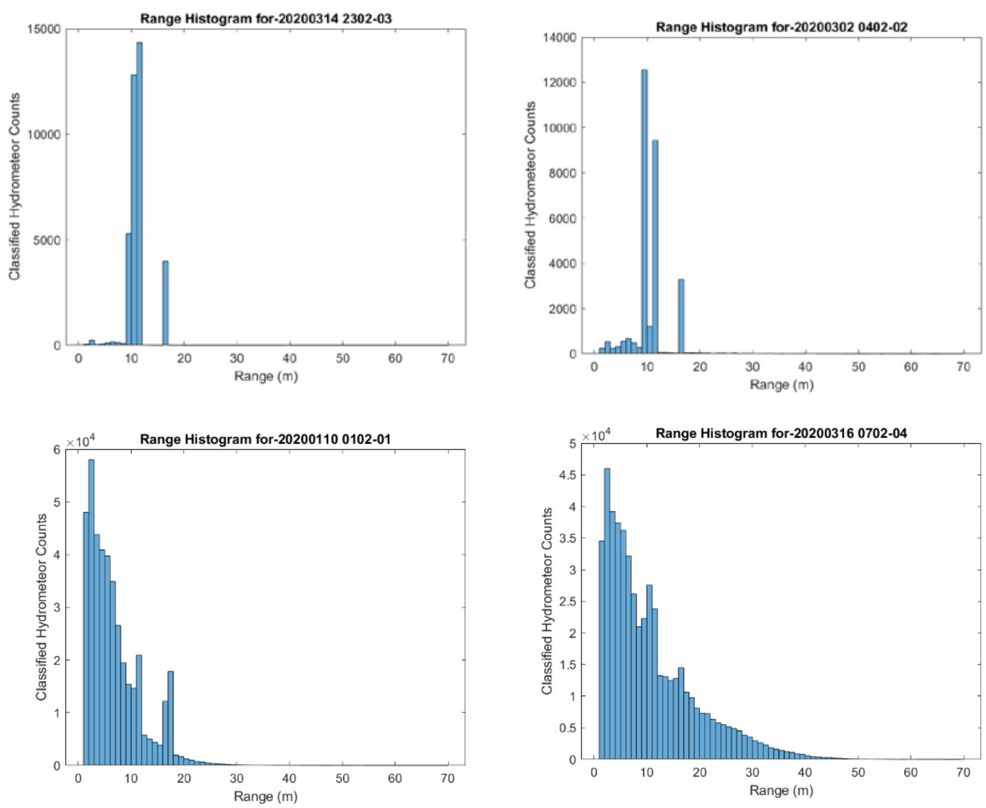

Figure 37: Line scan range histograms - light snowfall (top), heavy snowfall (bottom).

Exponential fits were modeled for each line scan and an e-folding length was calculated for each fitted model. The e-folding length is a common metric for exponential models and is the length at which the initial value decreases by a factor of the mathematical constant e. Figure 38 shows the exponential models and e-folding lengths for the range histograms shown in Figure 37. Due to the misclassifications, there is a bias for e-folding lengths at and beyond 10 meters. However, e-folding lengths shorter than 10 meters could be used as a metric for modeling visibility. This will be evaluated in Section 4.10.

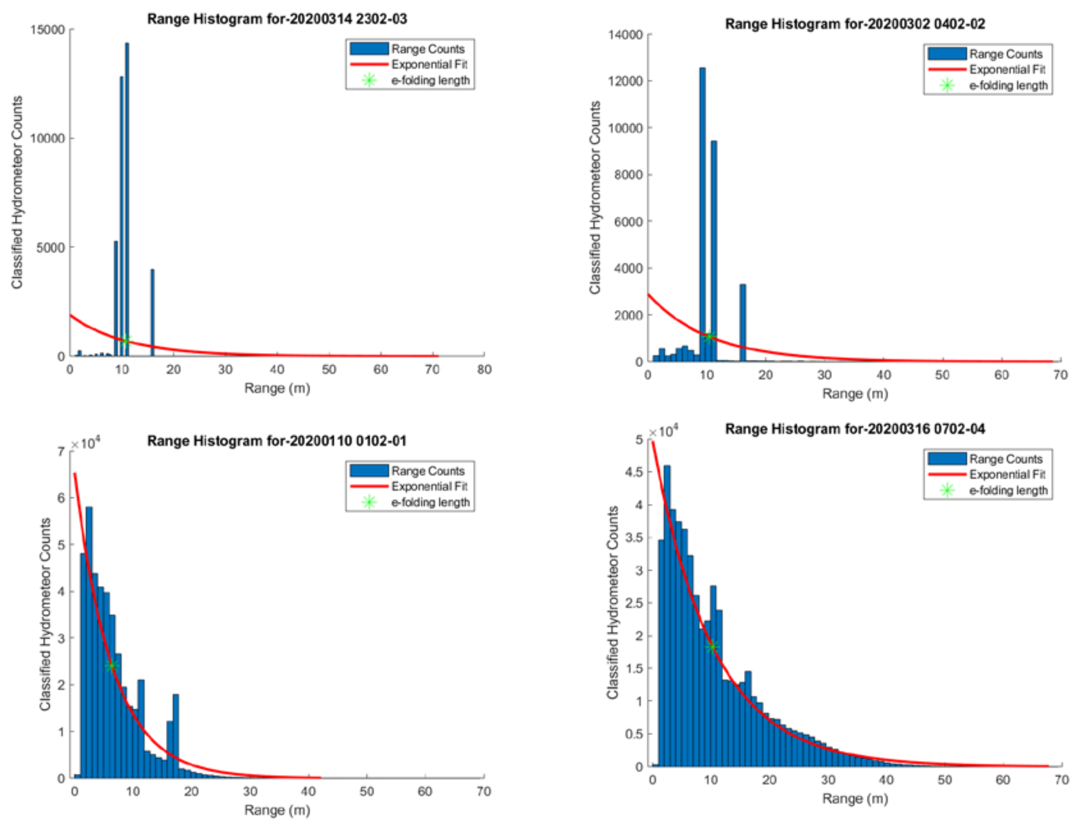

Figure 38: Line scan range histograms with exponential fits and e-folding lengths.

4.2. Target Statistics

4.2.1. Spectralon Panel

Plotting the first return average relative reflectance of the Spectralon panel from the frame scans shows that the average reflectance when no hydrometeors are present is around 78% of the TLS reflectance scale (Figure 39). Frame scans that were automatically identified as having hydrometeors present are shown in orange. There are reflectance reductions of first returns when there are hydrometeors present, which could be caused by hydrometeors absorbing and scattering the laser energy, but not reflecting enough to be identified as a target. After further examining the frame scans from December 5th-16th with reduced reflectance (highlighted in red), it appears the automatic hydrometeor identification algorithm failed to identify a these events as having hydrometeors, as PD records indicate snowfall occurring during the time of these scans.

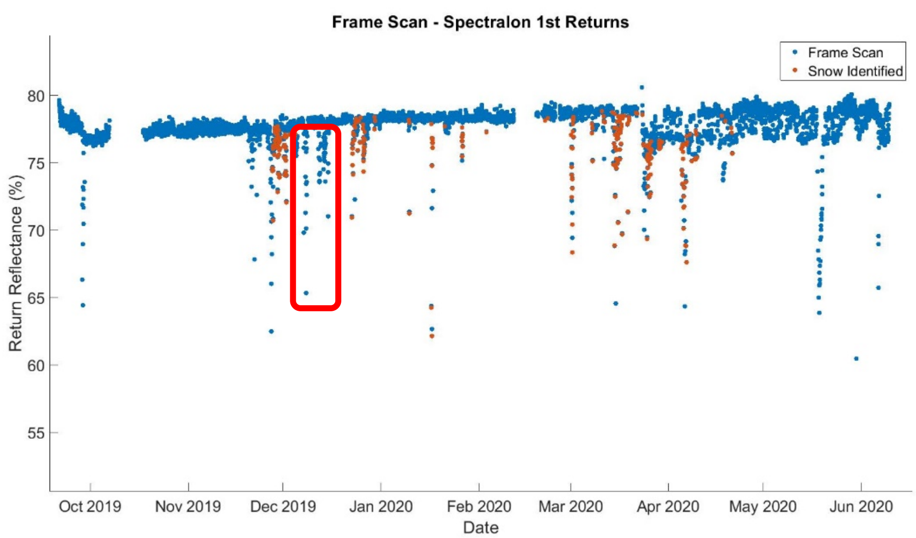

Figure 39: First return average reflectance of Spectralon panel from frame scans. Undetected snow events from December 5th-16th highlighted in red.

A cyclical variation in return reflectance was observed in the spring; Figure 40 shows a close up of the return reflectance behavior. There appears to be a diurnal pattern with a peak at midnight and trough around noon UTC. Examining the first returns more closely throughout the year reveals the diurnal variation always occurs when there are no hydrometeors present; however, the variation appears to have a smaller amplitude in the fall and winter. Figure 41 shows the cyclical variation in November.

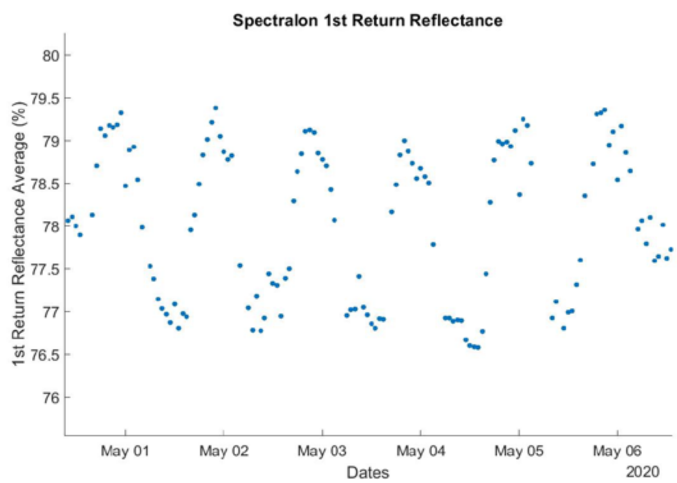

Figure 40: Daily cyclical variation of average reflectance from Spectralon panel – May.

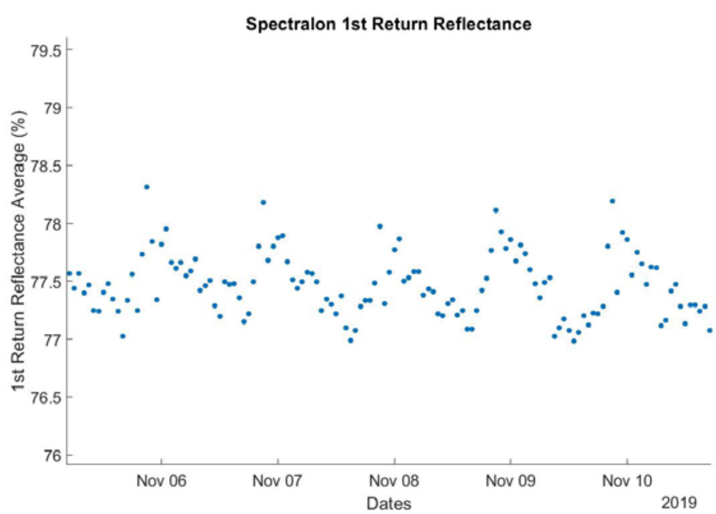

Figure 41: Daily cyclical variation of average reflectance from Spectralon panel – November.

Figure 42 includes the reflectance average of both the first and second returns from the Spectralon panel. When no second returns were identified, the return reflectance is zero. The max reflectance reduction caused by hydrometeors appears to be around 20% from the average when no hydrometeors are present.

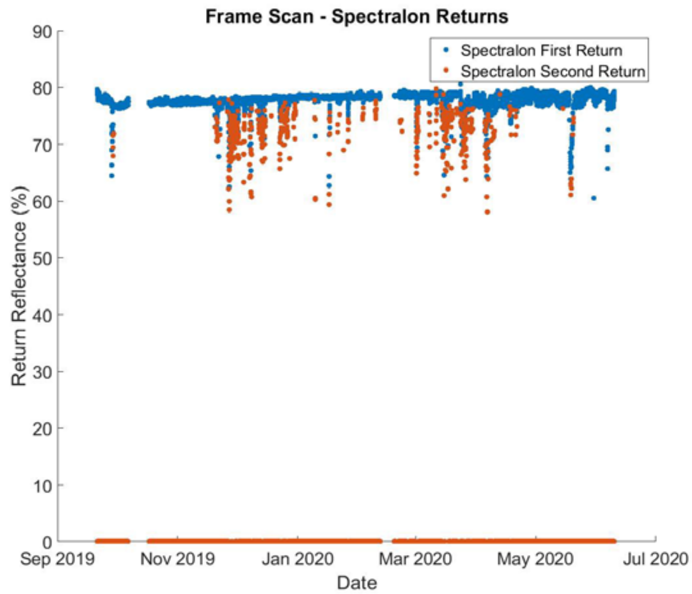

Figure 42: First and second average reflectance returns of Spectralon panel from frame scans.

Figure 43 shows that a greater reduction in reflectance typically occurs for the second return reflectance average. The first return reflectance is on average 4% higher than the second return with a standard deviation of 2.3% during hydrometeor events. Note that the unidentified December dates in Figure 39 appear with second returns from the Spectralon panel in Figure 43, suggesting that the automatic hydrometeor detection algorithm may not have been operating correctly during this time.

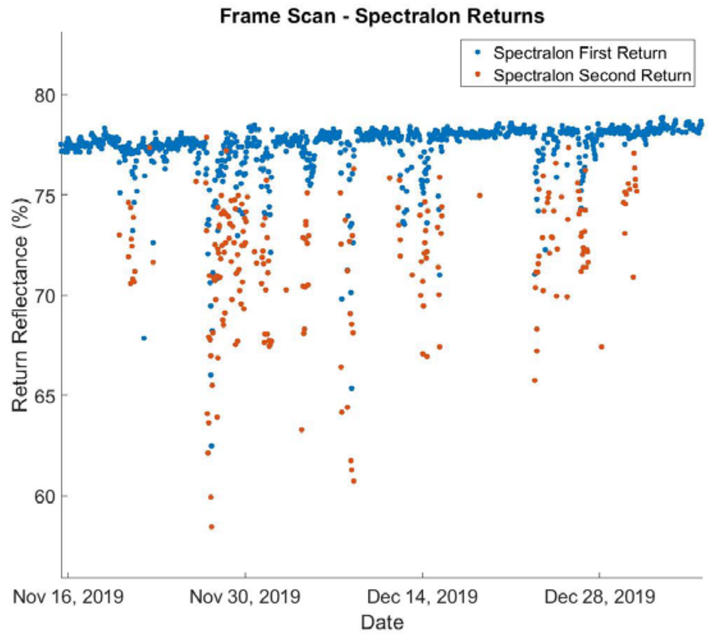

Figure 43: First and second average reflectance returns of Spectralon panel from frame scans – November-December.

4.2.2. Tree Trunk

The tree trunk exhibited similar return behavior as the Spectralon panel. It had a consistent average reflectance around 70% when no hydrometeors are present and the max reflectance reduction is just over 35% (Figure 44). The reduction in the averages could be caused by surface properties and the increased length the laser must travel. The tree trunk also exhibits similar behavior in the fall and spring with diurnal reflectance fluctuations, but the variations are smaller than those of the Spectralon panel. Figure 45 shows the cyclical variation in reflectance from the tree trunk in May.

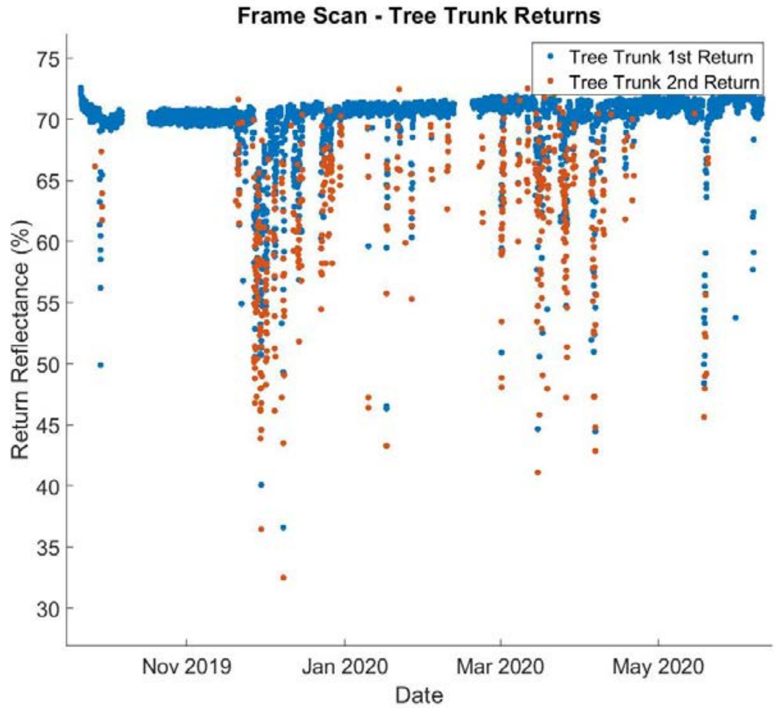

Figure 44: First and second average reflectance return of a tree trunk from the frame scan.

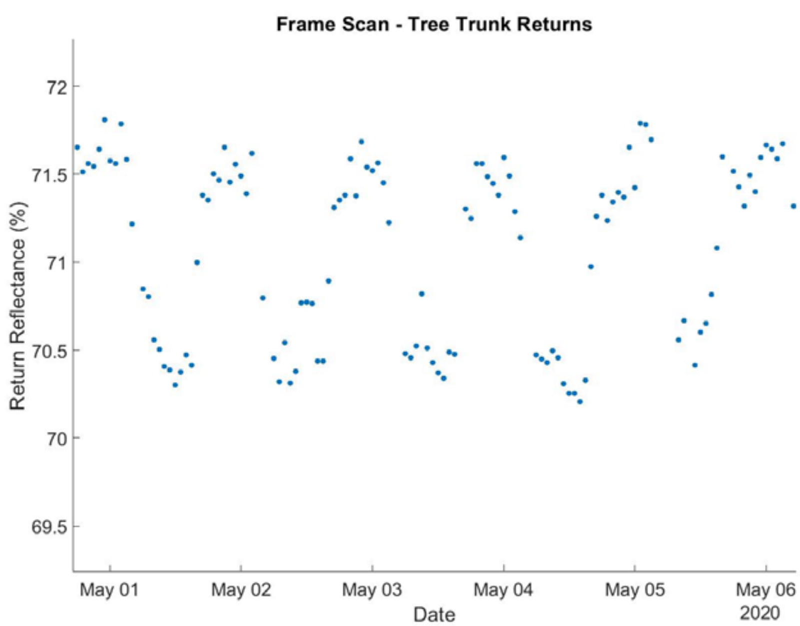

Figure 45: Daily cyclical variation of average reflectance from a tree trunk.

4.3. Reflectance Fluctuations

It is suspected that changes in temperature are responsible for the reflectance fluctuations. Plotting the ambient air temperature along with the Spectralon first return reflectance reveals a similar cyclical pattern that is most likely the cause of the fluctuations (Figure 46).

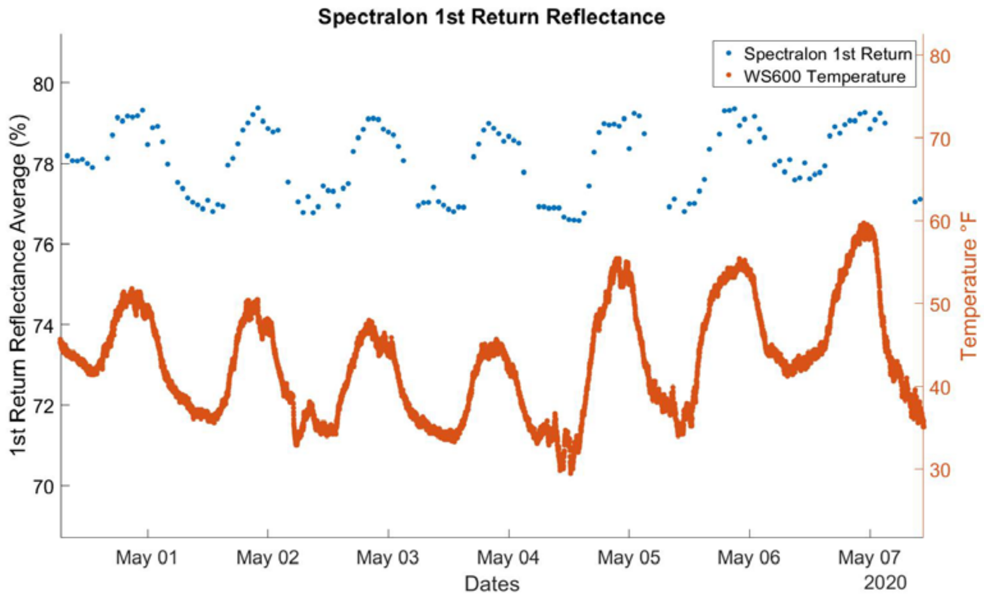

Figure 46: Spectralon first return reflectance average and ambient temperatures in May.

In effort to validate the hypothesis of temperature causing the cyclical variations of the TLS reflectance measurements, a few scans were conducted in an experimental setting at the University of Houston. A similar TLS, the Riegl VZ-2000, was setup approximately 8 meters away from a metal plate that had been coated with Spectralon paint. Scanning parameters were set the same as the frame scan with 0.04° for vertical and horizontal resolution and a pulse rate of 100 kHz. To test the effects of temperature, the TLS conducted scans with varying internal temperatures on two separate days. On February 7, 2021, the ambient temperature was 42 °F and on

February 16, 2021, the temperature was 21 °F. The first scans were acquired immediately once the TLS was set up, so that the internal temperature did not have time to acclimate to the surrounding environment. The TLS was then powered off for some time allowing the internal temperature to drop. Figure 47 shows the intensity values from the Spectralon scans captured on both days. The reflectance percentage is calculated by dividing by the max intensity of 65,536 (2^{16}). The internal temperature of the scanner and average reflectance can be seen in Table 4. This analysis, independent of the TLS at Sesame, shows that the Riegl V-line series reflectance values can fluctuate depending on the internal temperature of the instrument.

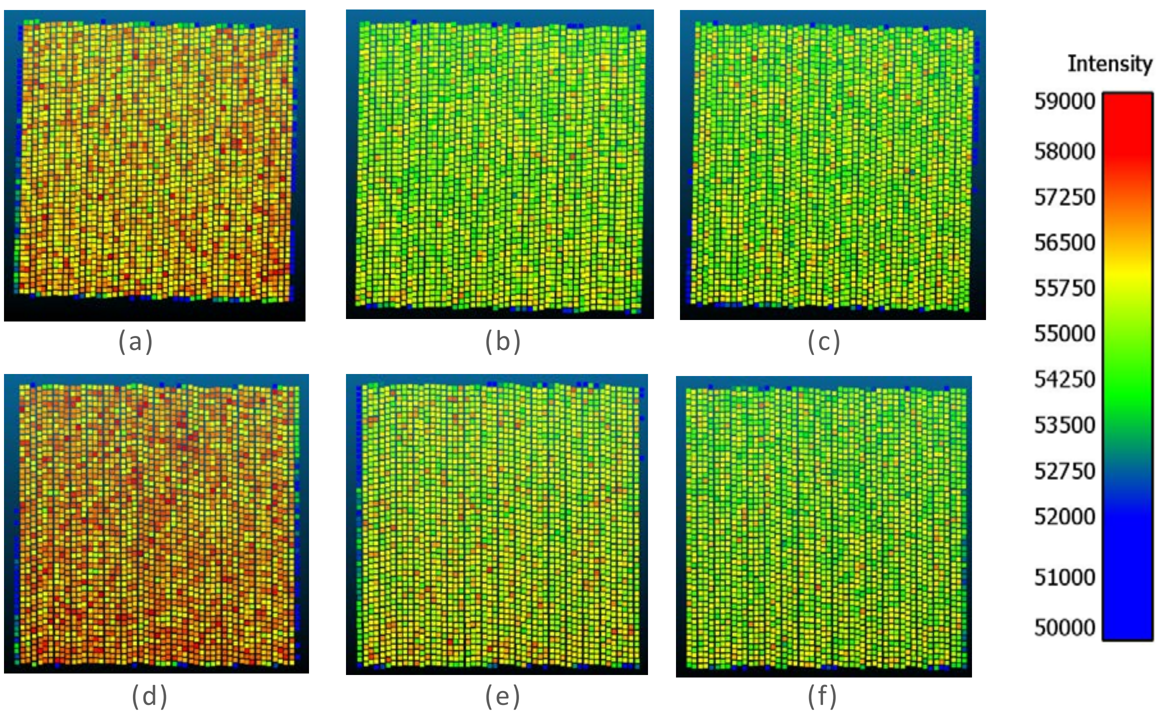

Figure 47: Spectralon scans of varying internal temperature of TLS: February 16th – (a) 77 °F, (b) 55.4 °F, (c) 39.2 °F and February 7th – (d) 78.8 °F, (e) 66.2 °F, (f) 59 °F.

Table 4: Spectralon average reflectance for varying internal temperatures of VZ-2000.

Scan	Outside Temperature (°F)	Internal TLS Temperature (°F)	Average Reflectance (%)
a	21	77	86.2
b	21	55.4	84.4
c	21	39.2	83.9
d	42	78.8	86.6
e	42	66.2	84.8
f	42	59	84.6

4.4. JUDS Comparison

The JUDS operates in a similar manner as the TLS, by use of two-way time-of-flight for an active signal. Because the JUDS measurements depend on the air temperature, an integrated thermometer is used in its range calculation. Comparing the TLS to the JUDS shows similarities between the two instruments and highlights some of the added benefits of using a laser scanner. The VZ-400 is capable of measuring points 100's of meters away in every direction, allowing the measurement of the entire snow surface surrounding the scanner, whereas the JUDS can only measure one static position directly below the sensor. Even though the JUDS makes measurements every minute and the TLS makes measurements every hour, the overall change in snow depth is consistently captured by both sensors. In Figure 48, the JUDS measurements are resampled to coincide with those of the TLS. The small offset between the two datasets is likely because the sensors are not able to measure the exact same location, as the JUDS is just outside the field of view of the TLS by a few meters.

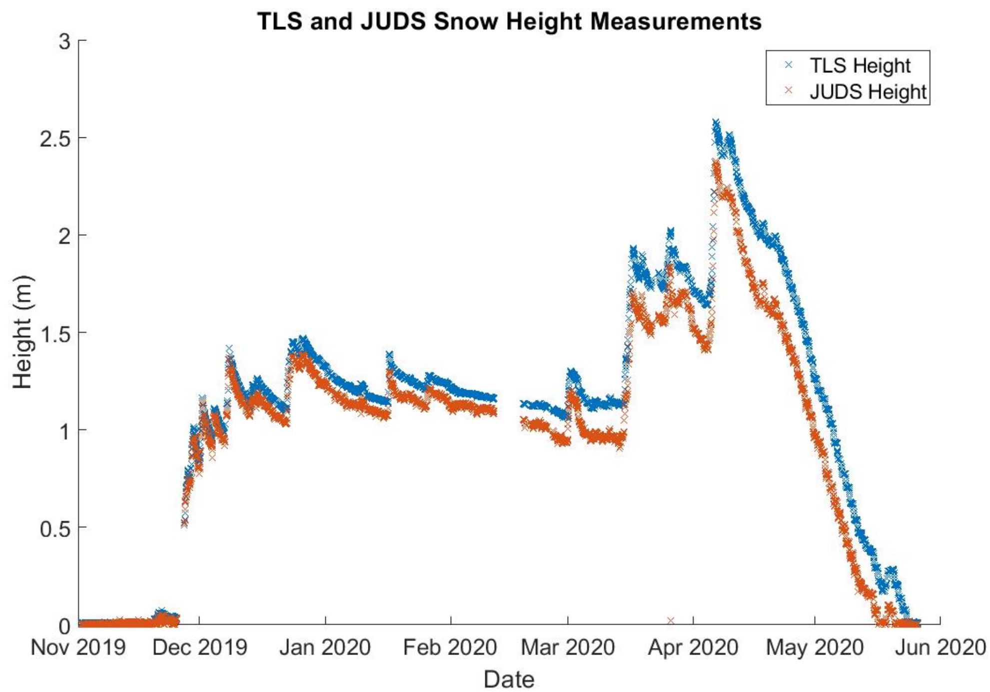

Figure 48: Snow height measurements from TLS and JUDS.

Table 5 shows the statistics of the differences between the TLS and JUDS measurements. On average, the measurements from the TLS are approximately 12 cm higher than the JUDS measurements.

Table 5: Height comparison of TLS and JUDS.

	Difference between TLS and JUDS measurements (cm)
Minimum	-1.6
Maximum	38.2
Average	12.6
Standard Deviation	10.1

Multiplying the relative snow density with a height measurement gives an estimate for SWE. If the relative density of a snowpack of 1 meter were 20%, after the snowpack melts it would yield 20 cm of water. The relative density was calculated from the JUDS and snow pillow measurements and Figure 49 shows the height measurements from the TLS and the corresponding SWE estimate. Assuming the relative density is similar for a region scanned by a TLS, SWE can be computed for a larger area and give better estimates for total SWE than for only a single location.

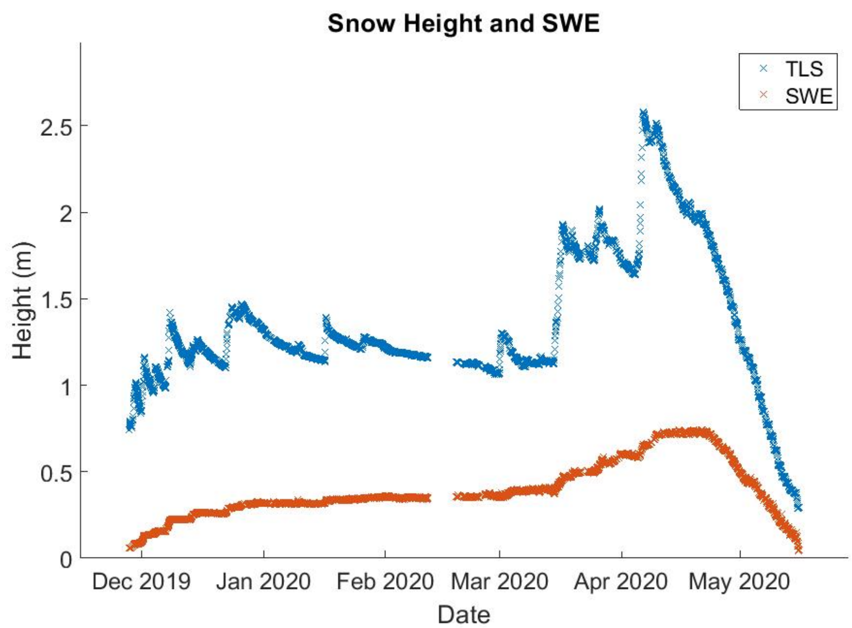

Figure 49: TLS snow height and SWE.

An advantage of using the TLS, aside from being able to measure a large surface area, is that it can also provide reflectance measurements of the snow surface. This gives an indication when the snow surface has undergone a change as the return reflectance is drastically altered depending on the angle of incidence relative to the TLS. Figure 50 shows TLS heights with the average reflectance measurements for dates in December and January. Lowered intensities can be observed when snow is not accumulating, allowing an extended period for the snowpack surface to undergo metamorphism.

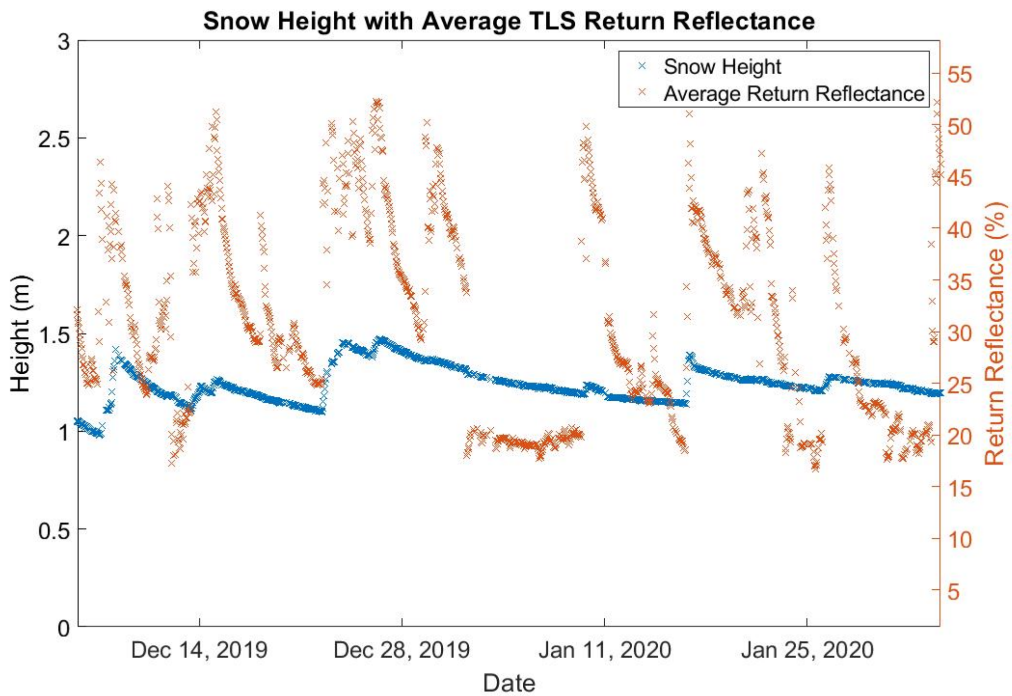

Figure 50: Snow height and average return reflectance.

4.5. Discrepant Scans

Of the 335 line scans that were identified as snowfall events, only 276 had disdrometer observations that indicated precipitation. The 59 discrepant scans were examined more closely to determine why the automatic identification process would be triggered if other sensors did not clearly indicate snowfall at the time of the data capture. A discrepant scan was normally located during, before or after a series robust line scan events (i.e., snowfall was recorded by the disdrometer). Of the 59 scans, 32 had PD results that indicated snowfall within +/- 5 minutes of the line scan. It is suspected that the cause for some of these discrepancies could be due to differences in location and size of sampling volume between the two instruments, therefore these scans will be omitted from the discrepant scan analysis. General comparisons were made between the remaining scans in an attempt to identify any reasons that could have caused these discrepancies. Figure 51 shows differences between time, the average count of hydrometeors per line scan cycle and various wind properties. There is no clear distinction for the time of day or time of the year. The average laser count per cycle is usually lower than 100 for discrepant scans. As wind speeds increase,

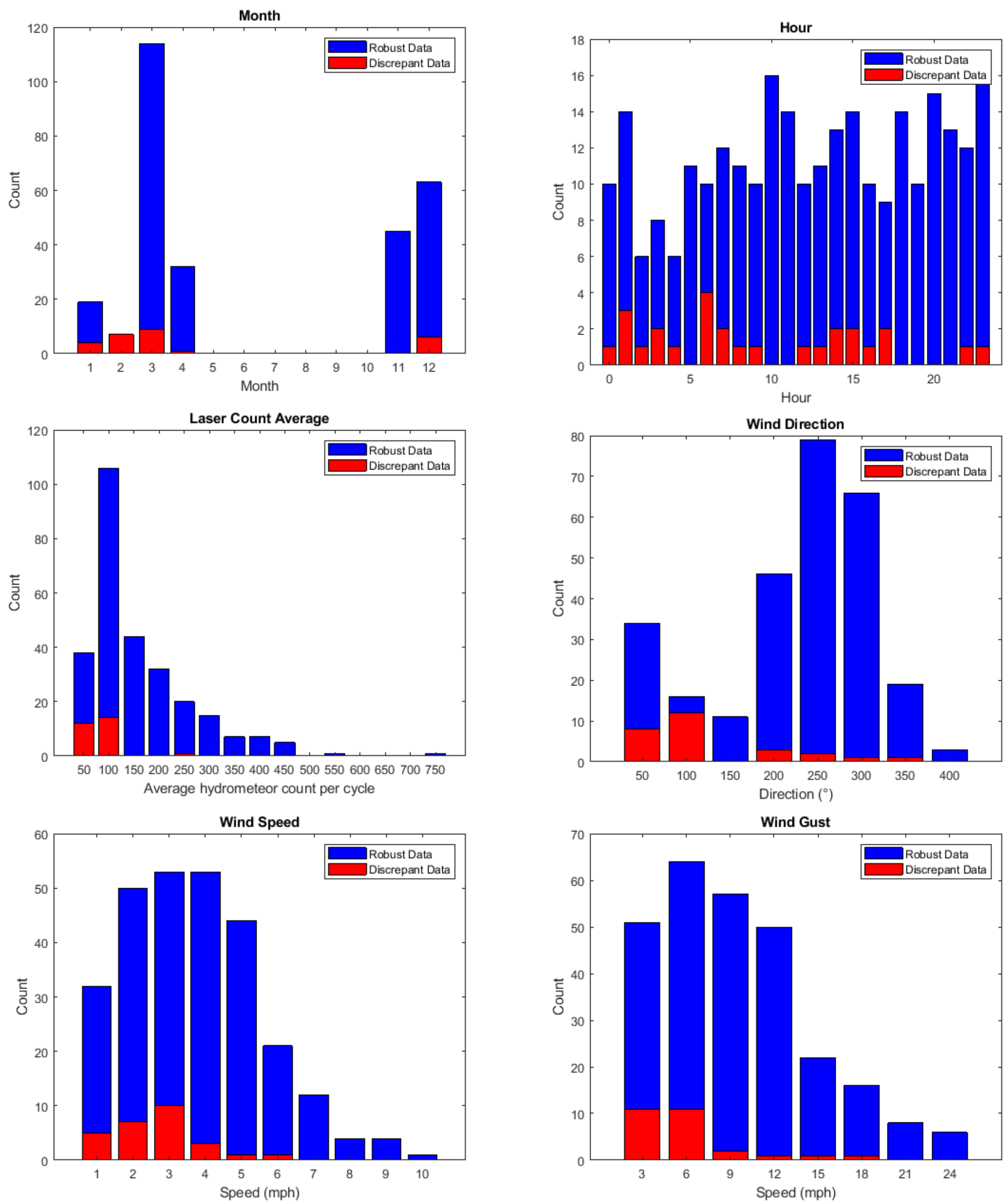

Figure 51: Robust and discrepant line scan comparisons.

more discrepant scans are observed up until 4 mph, after which discrepant scans become less prevalent. Easterly winds appear to have more discrepant scans compared to other directions.

Upon further analysis of the point clouds, additional discrepancies were discovered. Figure 52 shows the first return reflectance of the Spectralon panel colored by the count of points returned from the panel. This revealed that scan acquisition parameters were adjusted for the frame scan collections. Correspondence with CRREL confirmed that after January 28th 2020 the angular increments had been halved, which means the scanner sampling density increased (CRREL, personal communication, November 2nd, 2020). Because of this, fewer hydrometeors within a check volume would result in the threshold count being more easily reached - potentially resulting in more uncertain scans, with low snowfall rates.

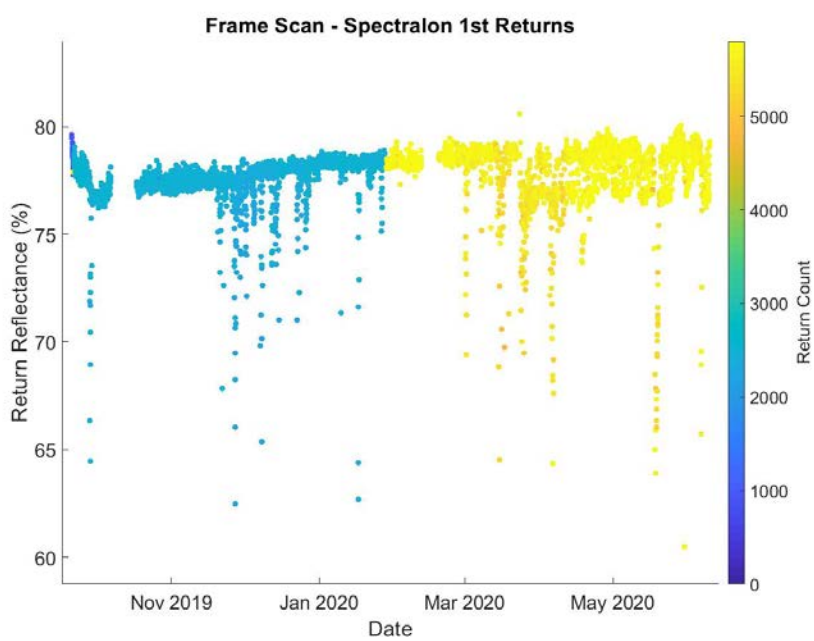

Figure 52: Average Spectralon reflectance colored by return count.

When reviewing the location of the check volumes, it was also discovered that one of the locations had been entered erroneously into the automatic hydrometeor detection algorithm. Figure 53 shows the intended and actual locations of the check volumes. This error partially negates the spatial decorrelation of using multiple check volumes since they are located side by side, however, after further review of the discrepant scans, most of these events would have been triggered regardless of the location of the check volumes since many returns were observed around the scanner.

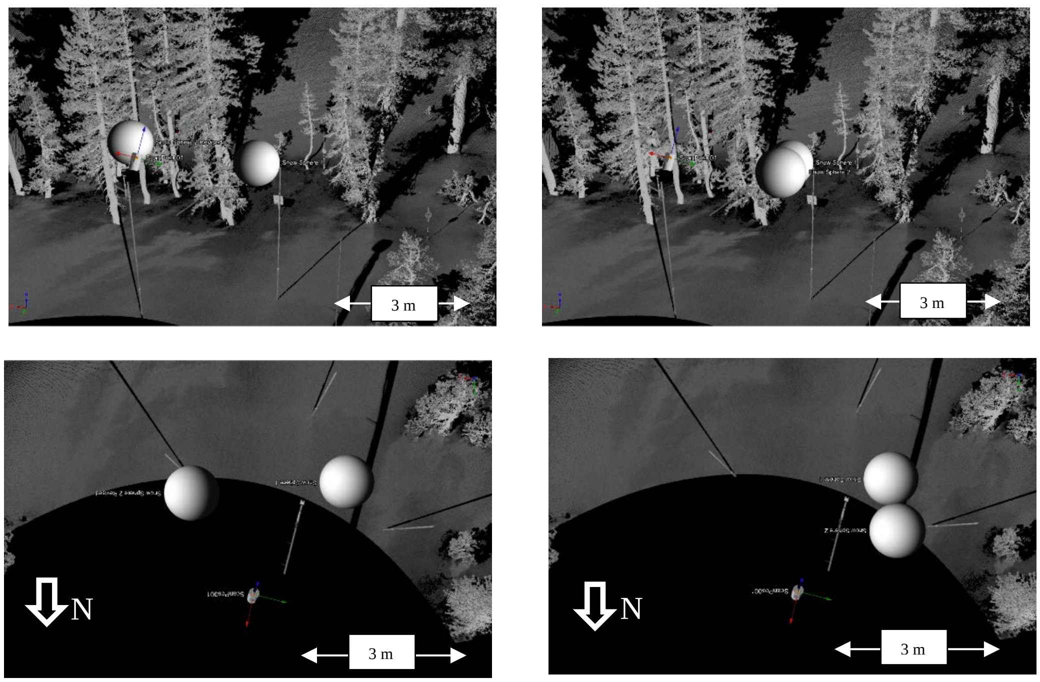

Figure 53: Intended (left side) and actual (right side) check volume locations.

4.6. Full-waveform

Riegl's proprietary software, RiSCAN Pro, is needed to visualize the FW results acquired at Sesame. Results show the various FW return behaviors that can be acquired from a TLS system in this environment. Figure 54 shows a laser pulse from a line scan with the accompanying FW amplitudes. Distinct target returns were typically

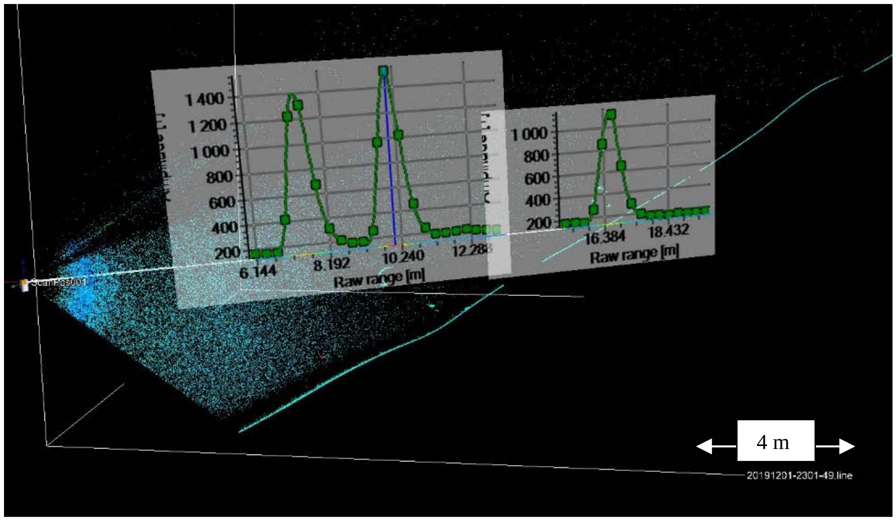

Figure 54: RiSCAN Pro full-waveform results from a laser pulse.

acquired when there were no obstructions from multiple targets. One of the derived metrics from the FW return is the amount of deviation that occurs from the expected system response of a flat, orthogonal target. As stated earlier, the return energy is sampled every 2 nanoseconds, which is approximately 60 cm intervals. When targets are close to or within this range resolution, the radiometric cross-section will deviate from a normal system response.

Figure 55 shows a line scan colored by pulse deviation. Low deviation indicated by blue is a normal return, which is what is predominantly captured for hydrometeors. Figure 56 shows the waveform of a hydrometeor return with low deviation. Higher deviations are observed when multiple hydrometeors are near each other and illuminated by a laser pulse at nearly the same time (Figure 57) or when a hydrometeor is illuminated close to a boundary, such as the snow surface or a tree branch (Figure 58). These deviations are indicated as green in Figure 55.

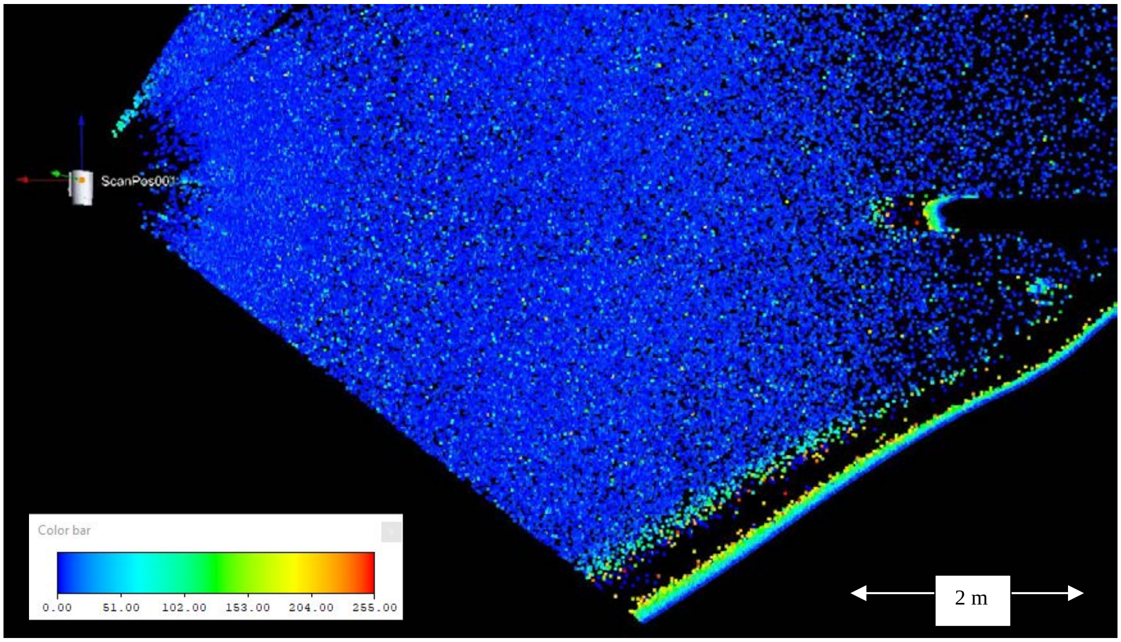

Figure 55: Line scan deviation in RiSCAN Pro.

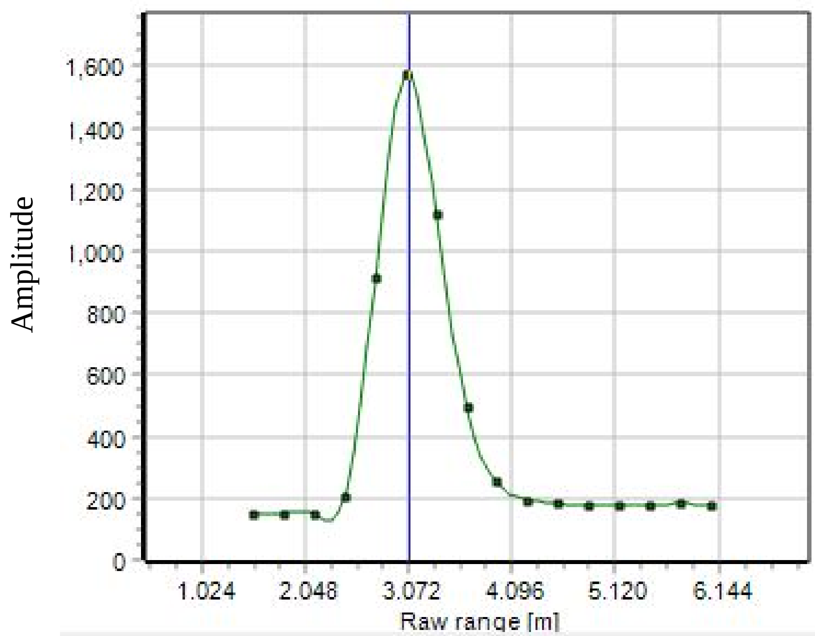

Figure 56: Full-waveform of single hydrometeor with low deviation.

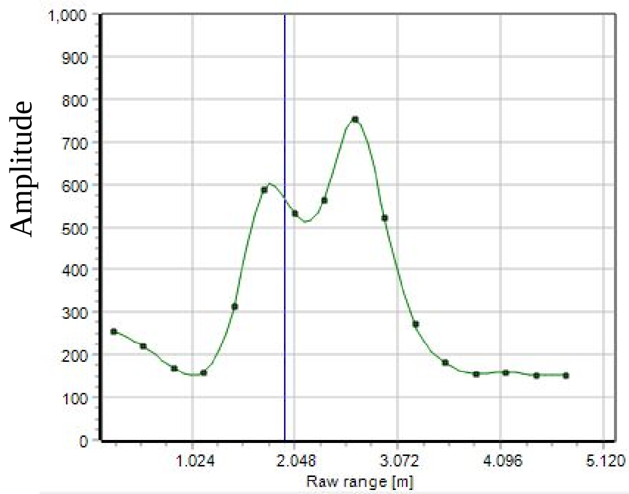

Figure 57: Full-waveform of two hydrometeors with minor deviation.

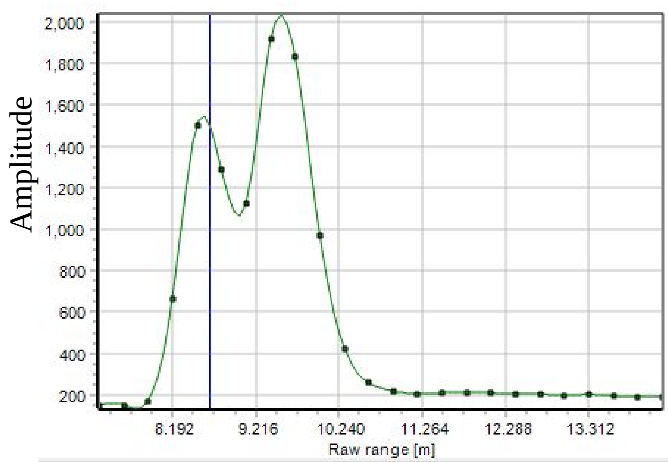

Figure 58: Full-waveform of hydrometeor near snow surface with minor deviation.

Hydrometeors can still have a low deviation when at sufficient distance from a surface. Figure 59 shows FW of a return with low deviation just above the boundary of green deviations that exists over the snow surface in Figure 55. As two targets get closer in proximity, their energy peaks begin to approach each other, which changes the overall shape from a normal return. Figure 60 - Figure 62 shows examples of higher deviations indicated by yellow, orange and red points in Figure 55.

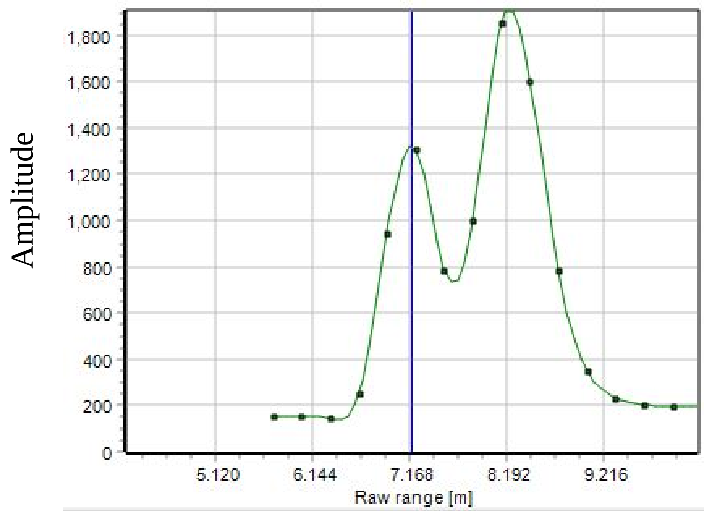

Figure 59: Full-waveform of hydrometeor above the snow surface with low deviation.

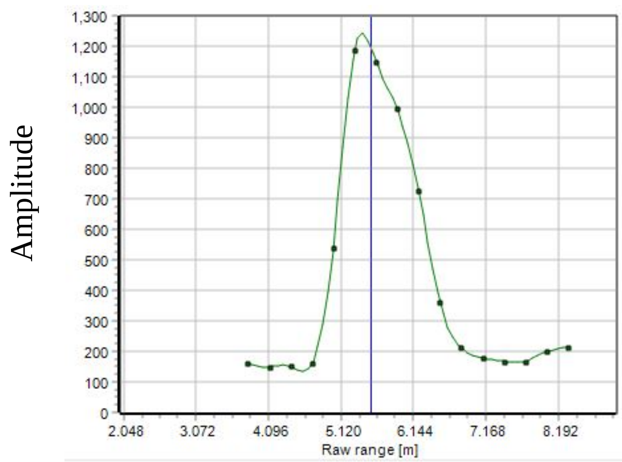

Figure 60: Full-waveform of two closely spaced hydrometeors with higher (yellow) deviation.

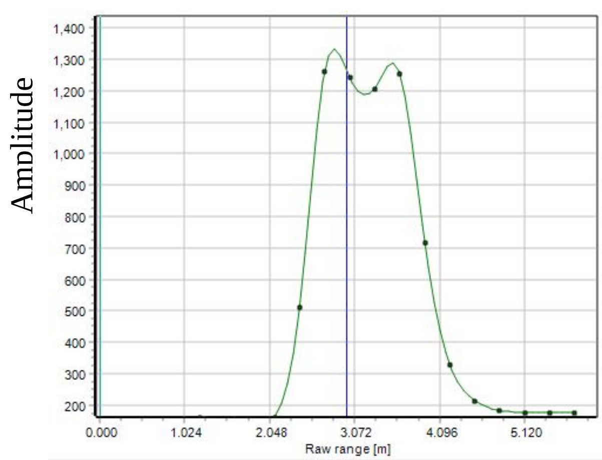

Figure 61: Full-waveform of a hydrometeor near the snow surface with higher (orange) deviation.

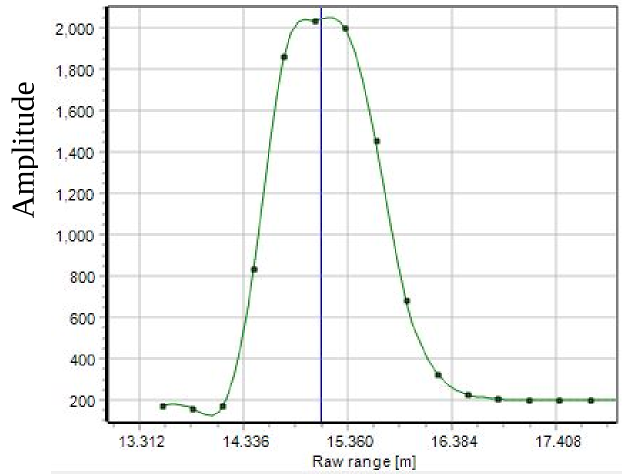

Figure 62: Full-waveform of a hydrometeor near the snow surface with high (red) deviation.

Fortunately, one of the line scans acquired with FW data experienced range reductions (Figure 63). This will show the FW characteristics of returns that reach extinction due to interaction with hydrometeors and the atmosphere. Returns were

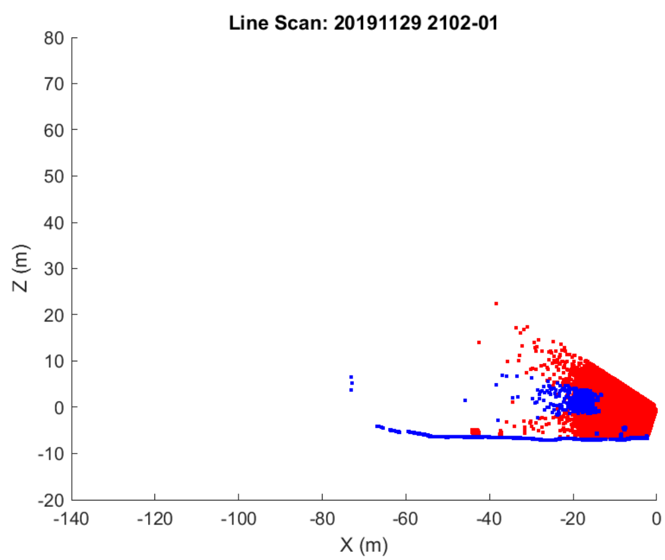

Figure 63: Line scan with range reductions

filtered such that only single returns were examined to ensure no other target impeded the laser energy beforehand and making sure no other return was acquired after. FW returns during dense snowfall showed that the laser energy is not capable of acquiring many returns from hydrometeors and does not exhibit a unique waveform characteristic. Only one dominant return is captured followed by a long trail of low amplitudes/noise. Figure 64 shows single returns at different lengths that met extinction in the atmosphere. Returns examined at a closer range and further away all show similar FW characteristics.

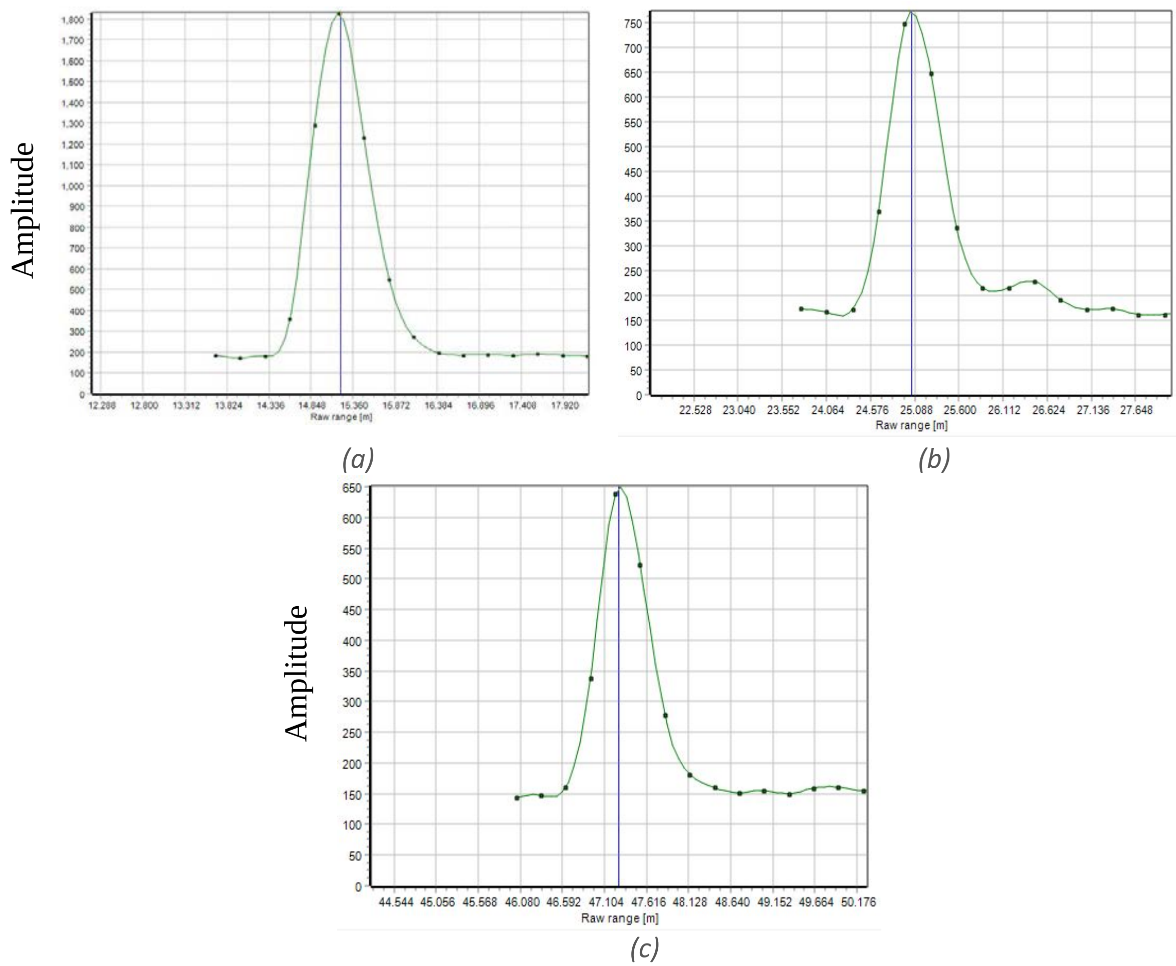

Figure 64: FW of returns that met extinction in the atmosphere at different ranges. (a) 15 meters, (b) 26 meters, (c) 47 meters.

4.7. Particle Size

The MDS calculated from the PD size estimates for a given collection period was compared with various TLS metrics. MDS is not an exact, definite proxy for the particle size and there is a lot of variability due to the amalgamation of bulk observations, sampling of different hydrometeors and inherent uncertainties of the PD size estimation for solid precipitation.

The type of hydrometeor formation (i.e., snow, rain, hail, etc.) depends on the vertical temperature profile of the atmosphere (Sankare and Theriault 2016). Figure 65 plots the ambient air temperature with the MDS to see if temperatures at the surface have any impact on the observed estimates of hydrometeor size. There appears to be no correlation between ambient temperature and MDS.

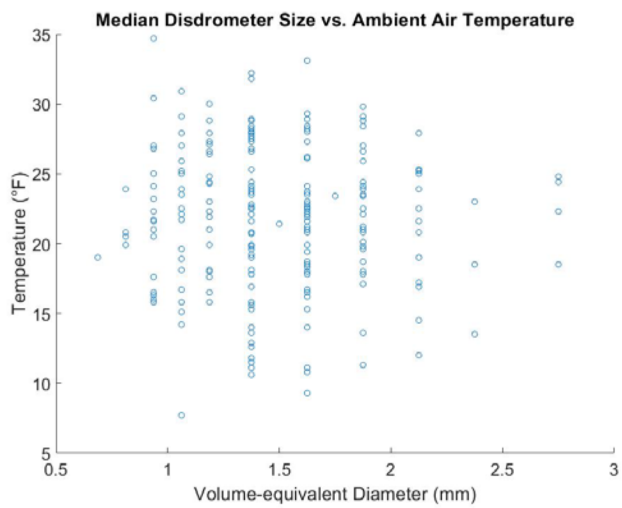

Figure 65: Median disdrometer size vs. ambient air temperature.

It was suspected that larger hydrometeors would impede more of the laser energy, therefore further reducing the second return reflectance on the Spectralon panel. The

MDS compared with the Spectralon second return reflectance does not show any clear correlation to support this (Figure 66).

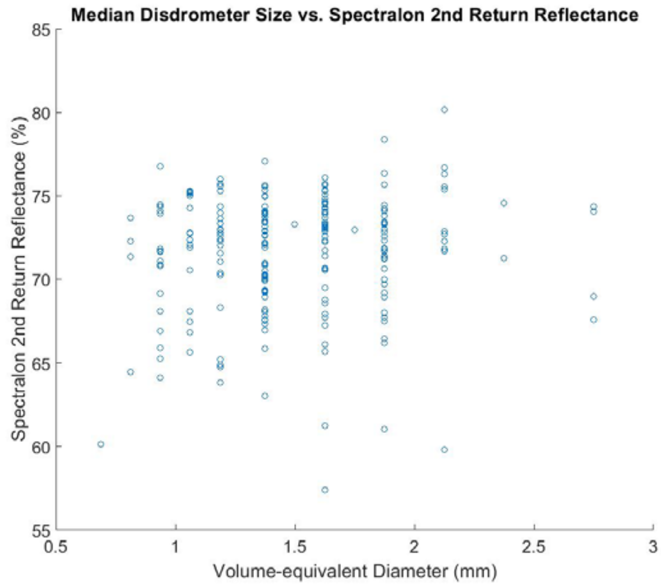

Figure 66: Median disdrometer size vs. Spectralon second return reflectance average.

Returns in the near field range of the scanner had a large variation of counts between all of the line scans. Larger hydrometeors can reflect more of the laser energy back to the sensor, which might make them easier to detect in the near range. In Figure 67, MDS was compared to the near count total within 5 meters of the TLS. Particle size is not the only factor for observing targets in the near field, because rate of snowfall will also determine how many hydrometeors are present to observe. Therefore, points are colored by the PD snow intensity estimate as well. The plot indicates that particle size does not impact number of observations in the near field. Smaller particle sizes still acquire large near count totals when there is a lot of precipitation. None of the larger MDS values were observed at these higher precipitation rates.

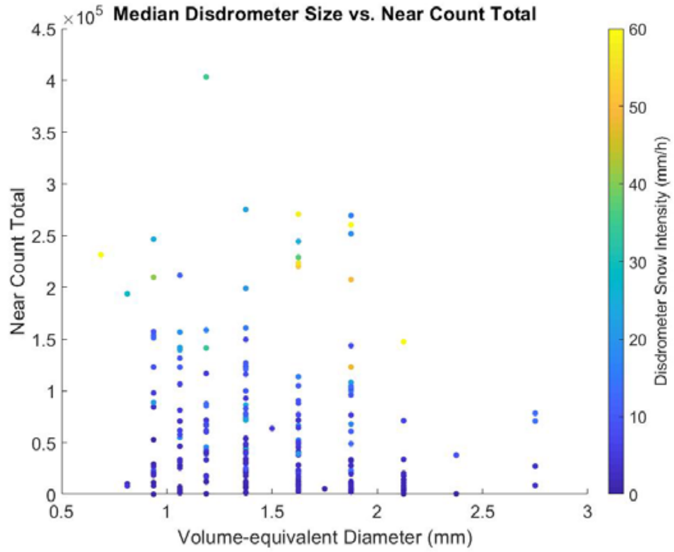

Figure 67: Median disdrometer size vs near count total.

Since larger hydrometeors occlude more of the laser energy, the MDS was also compared with the average range of hydrometeors observed for each line scan (Figure 68). Again, PD snow intensity rate estimate is used to color the points. Size does not appear to be correlated with the average range hydrometeors are observed. Occlusion of the TLS' range depends more on the rate of precipitation.

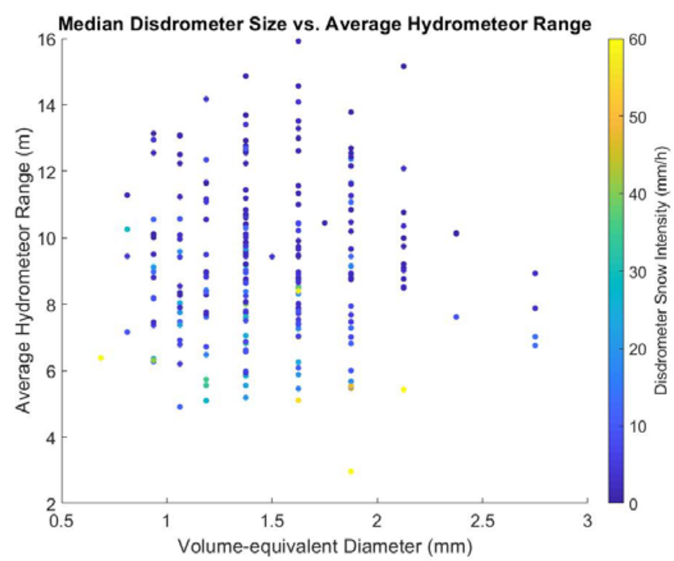

Figure 68: Median disdrometer size vs average hydrometeor range.

4.8. Particle Speed

Velocity estimates from the PD were compared with estimates that were derived from streaks observed in the TLS point clouds. Streaks could be observed in approximately 70% of the frame scans during hydrometeor events. A manual and automated process were both evaluated. For the manual evaluation, 38 streaks were examined and results were found to be comparable to those of the PD. Figure 69 shows the PD speed estimates and the manually calculated speeds from the TLS point streaks. All of the measured velocities from the TLS are within the measured range of

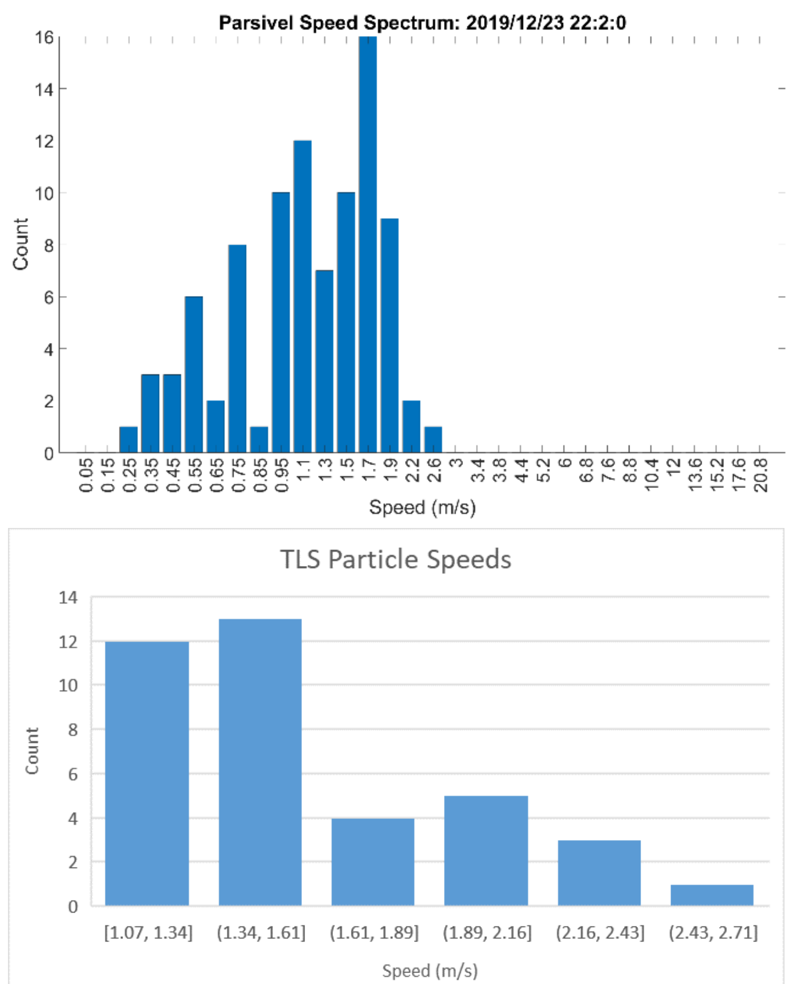

Figure 69: PD speed estimates (top) and manually calculated speeds from TLS (bottom).

the PD. Note that these streaks were manually selected because they visually appeared to be a good selection choice with ample returns defining a longer streak providing a larger signal-to-noise ratio.

An automated function was then created to calculate the total number of points within a streak along with total distance, time interval and velocity. The input to the function is a point cloud of returns within five meters of the scanner with a scalar field of calculated linearity values from CloudCompare (see section 3.3.1). The function then cycles through all of the points to find returns that are within 0.05 seconds of each other. This revealed a large variety of streak velocities estimated from the TLS, many of which are unreasonable with measurements from 20 m/s up to a few extreme values over 1000 m/s. Figure 70 shows a histogram of automatically calculated velocities from the point cloud in Figure 31. The extreme velocities have very short time differences of a few microseconds and the streaks only contain a few particles. Coordinate uncertainty (due to coordinates automatically being placed at the center of the laser beam), motion of the scanning laser and oversampling are suspected to be the causes for unrealistic estimates. Filtering streaks that have more than two returns and limiting velocities to less than 5 m/s shows results similar to those of the PD and manually selected streaks (Figure 71).

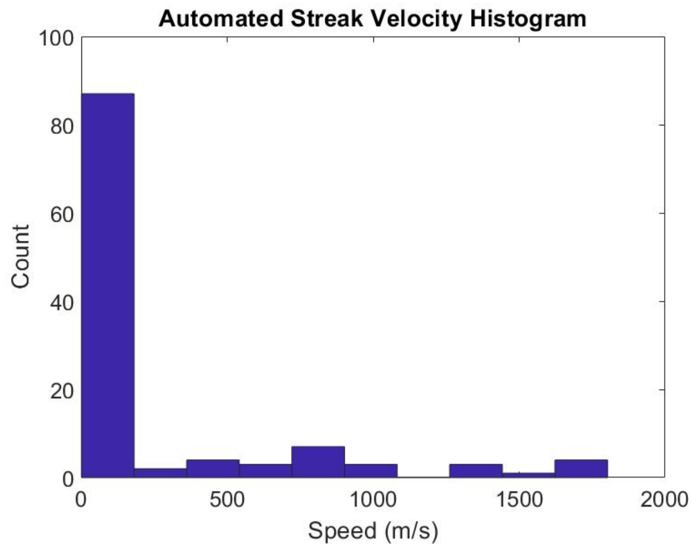

Figure 70: Automatically calculated streak velocities.

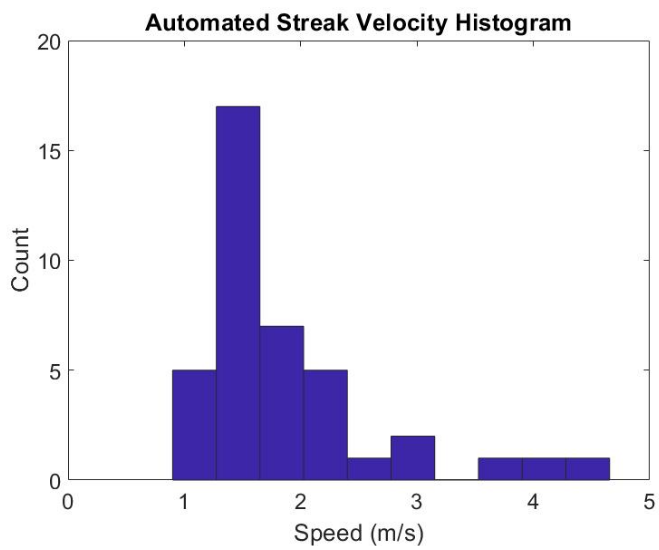

Figure 71: Automatically calculated streak velocities - filtered by count and speed.

4.9. Snowfall Intensity

The snow intensity rate estimated by the PD is the instrument's attempt to quantify the amount of snow that will accumulate based on measurements of hydrometeors in the air. Obviously, the TLS could just scan the surface at different time intervals to estimate accumulation. However, the PD estimate was used as a proxy for the amount of hydrometeors present in the air to compare with statistics from the TLS observations. Various regressions were evaluated to determine what TLS observations were useful and which model had the strongest correlation with the PD snowfall intensity.

An exponential fit aligns with the reduction of the first return reflectance average (Figure 72). Parameters for the non-linear regression model and the goodness of fit are given in Table 6. As noted earlier, light snowfall events are influenced by the

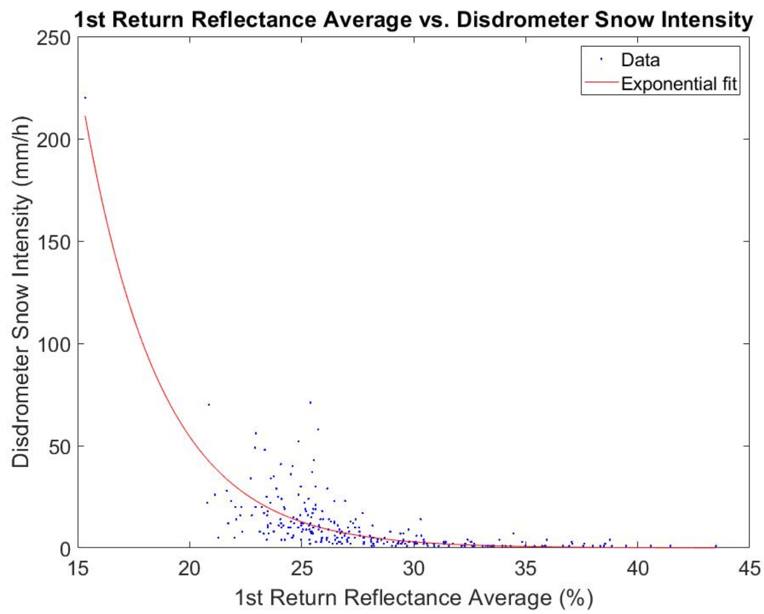

Figure 72: Non-linear regression of 1st return reflectance average vs. disdrometer snow intensity.

Table 6: Non-linear regression results from 1st return reflectance average vs disdrometer snow intensity.

	1st Return Reflectance Average vs Disdrometer Snow Intensity
Model	a*exp(b*x)
a	1.82E+04
b	-0.2907
R^2	0.6845
RMSE	9.83

misclassification of tree branches as hydrometeors, which causes the larger reflectance average. As the snowfall intensity increases and more hydrometeors are scanned, a reduction in the average first return reflectance is observed. There is little variation until the reflectance average drops below 28%. The lowest average just above 15% was during the heaviest snowfall event observed in which ranges were most reduced. The reduction of the first return reflectance average is believed to be a result of more first returns being actual hydrometeors compared to false positive returns in the tree branch and returns being observed closer to the scanner where the recorded returns have lower amplitudes (see Figure 10).

Figure 73 shows a point cloud of observations within 5 meters of the scanner colored by their reflectance percentage. Clearly, within the first 2 meters the return reflectance is significantly smaller. This is confirmed when plotting the first return reflectance average versus the average hydrometer range, which shows a strong linear

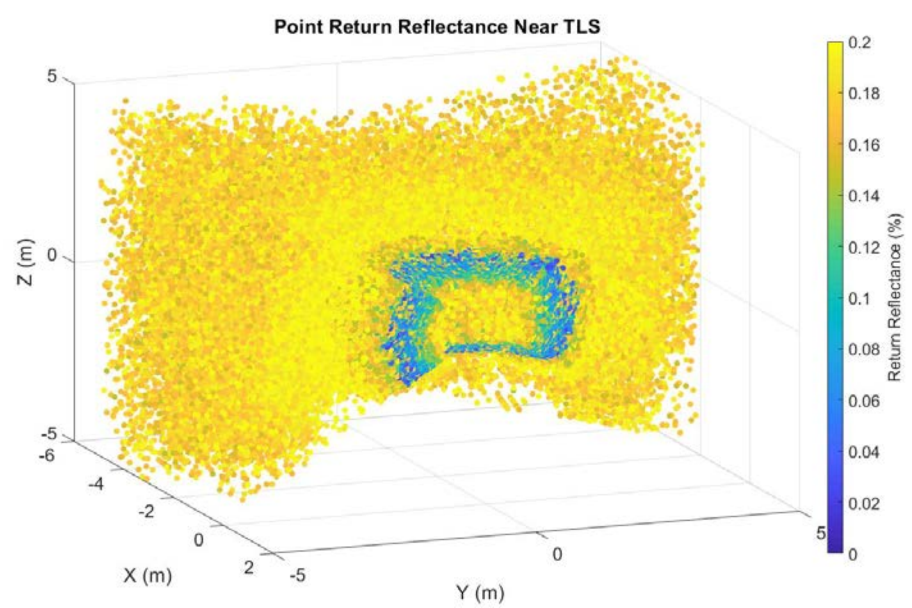

Figure 73: Near frame reflectance returns.

trend (Figure 74). A large reflectance variation is seen as the average range approaches the first tree branch around 10 meters from the scanner.

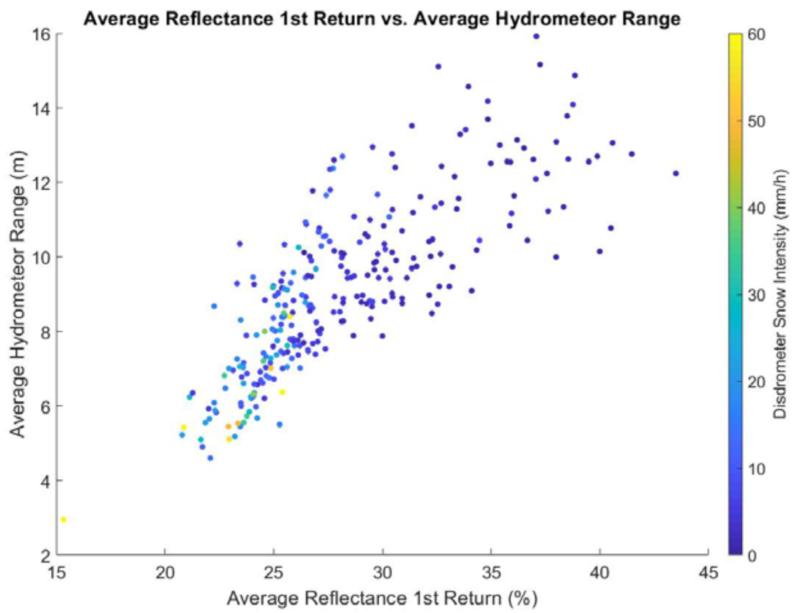

Figure 74: Average reflectance 1st return vs average hydrometeor range.

The near count total, average first return reflectance, single and double returns were evaluated in a multi-variable linear regression model (Figure 75) and the resulting statistics are given in Table 7. There is a lot of variance for smaller snowfall events, but larger snowfall events exhibit a linear trend. The slope of the model proved significant with a confidence level of 99%. The RMSE of approximately 10 mm/h seems reasonable considering the PD estimated accuracy for snow intensity is 20% (OTT Hydromet). This shows that the TLS measurements are correlated with snow intensities.

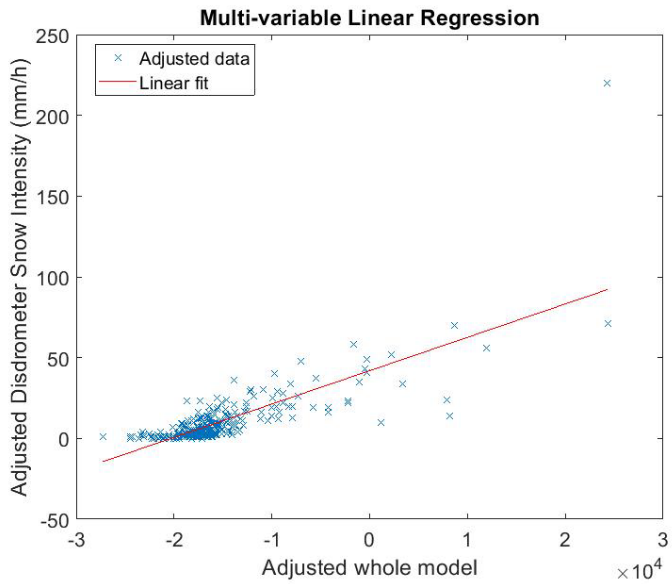

Figure 75: Multi-variable linear regression of near count total, average reflectance 1st return, return count 1 and 2 vs disdrometer snow intensity.

Table 7: Multi-variable linear regression statistics for disdrometer snow intensity model.

	Near Count Total, Average Reflectance 1st Return, Single Count, Double Count vs Disdrometer Snow Intensity
R^2	0.604
RMSE	10.9
SSR	49,302
SSE	32,303
MSR	12,326
MSE	119
F Statistic	103
F Critical	3.4
Significant	Yes

The Spectralon line scan and a subset of panel returns filtered from the frame scans were also evaluated and modeled. Figure 76 shows the second return reflectance average of points that hit the Spectralon panel from the frame scan. As the average reflectance is reduced, we have an increase in PD snow intensity. The plot is colored by the count of second returns that hit the Spectralon panel. Higher count totals are

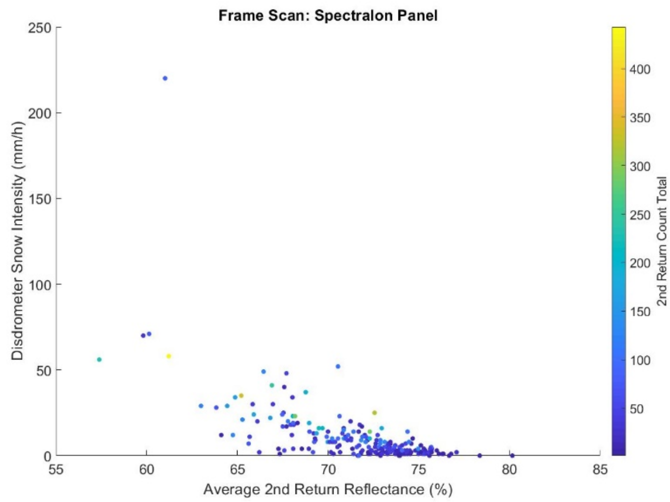

Figure 76: Average second return reflectance from Spectralon panel of frame scans identified with hydrometeors vs disdrometer snow intensity.

correlated with a higher PD estimate and a larger reduction in the average reflectance. Similar results are shown in Figure 77 for the second return reflectance averages from the Spectralon line scan. The main difference between these two datasets (besides the Spectralon line scan having fewer observations) is the amount of second returns collected. The frame scan on average collects 50 second point returns from the Spectralon panel, whereas the Spectralon line scan on average collects 1,700 second point returns. When the frame scan plot is zoomed in (due to having some higher PD estimates) it resembles that of the Spectralon line scan (Figure 78). These results indicate that depending on the target size and range, a limited amount of return points can still provide meaningful insight and that a dedicated line scan may not always be necessary. Non-linear regressions for the target along with their statistics can be found in Appendix E.

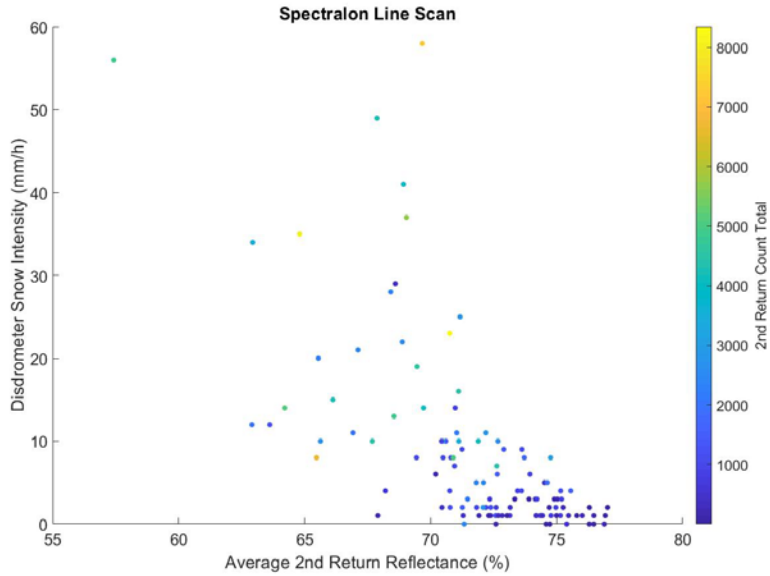

Figure 77: Average second return reflectance from Spectralon line scan vs disdrometer snow intensity.

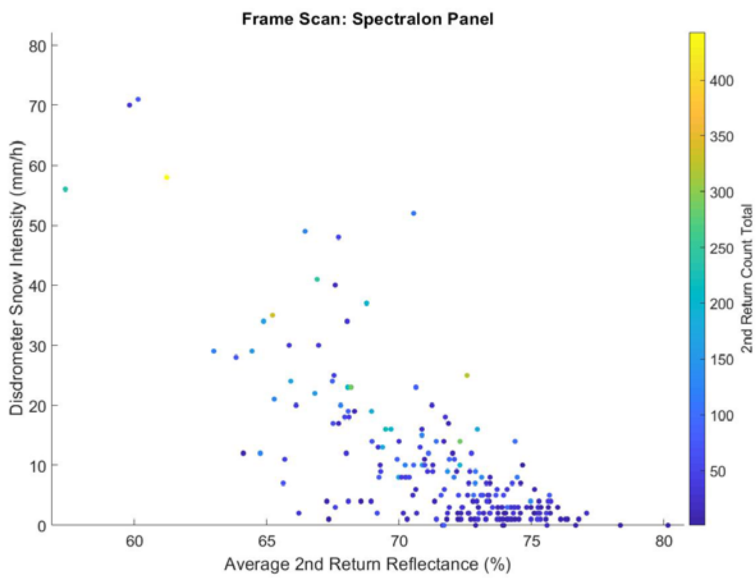

Figure 78: Average second return reflectance from Spectralon panel of frame scans identified with hydrometeors vs disdrometer snow intensity – zoomed in.

4.10. Visibility

The PD estimates visibility by extrapolating observations from a 54-cm^2 area to ranges of several kilometers assuming homogeneity in the atmosphere from 0-20 km. Human-perceived visibility is much more complex than a single metric of light scattering at one specific wavelength. Nevertheless, the PD MOR estimate is modeled with different observations derived from the TLS scans. Given the large extrapolation of the PD MOR and the TLS being unable to make measurements at those ranges, estimates were limited for some of the models to improve the overall fit. MOR estimates were limited by their range based upon the variance observed within the dataset.

Figure 79 shows the relationship between the disdrometer snow intensity and MOR. The plot is colored by first return reflectance average. Note the lowest visibility is from the heaviest snowfall event observed by the laser scanner. Plotting the PD MOR with the near count total (Figure 80) revealed a similar trend as the estimated PD snow intensity when the plot is zoomed in (Figure 81).

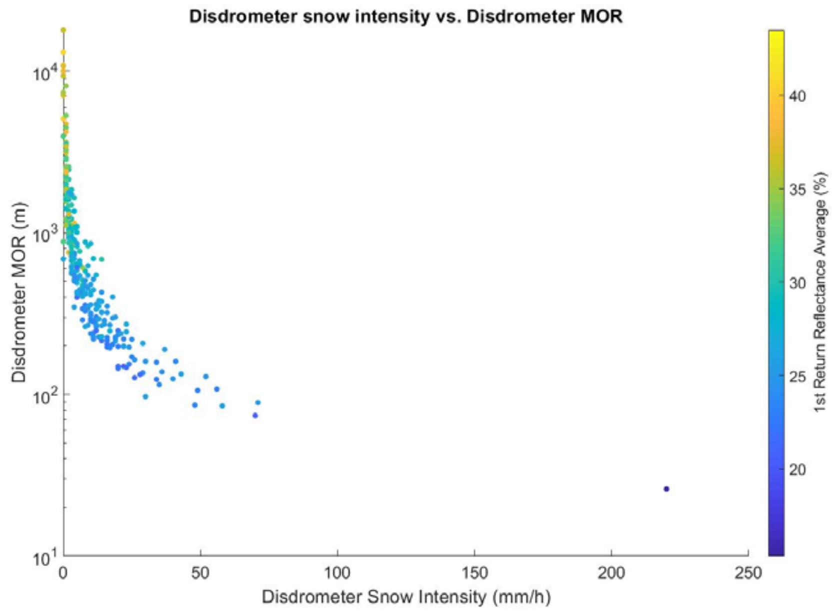

Figure 79: Disdrometer snow intensity vs MOR.

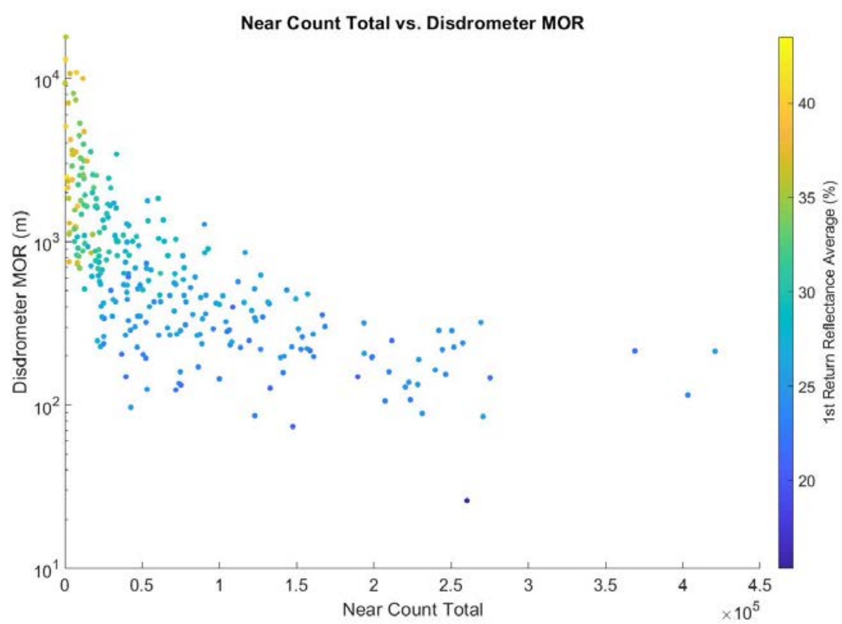

Figure 80: Disdrometer MOR vs near count total.

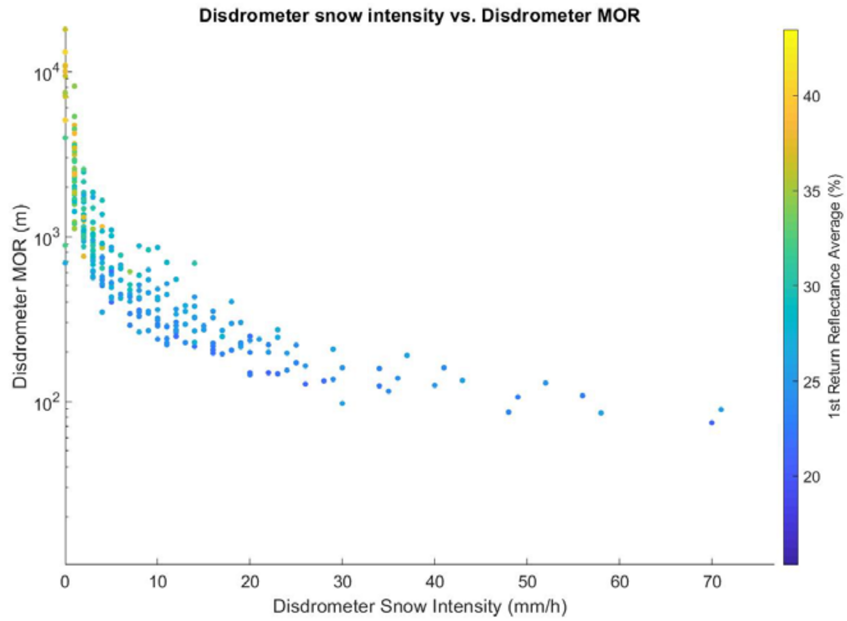

Figure 81: Disdrometer snow intensity vs MOR – zoomed in.

Nonlinear regression was used to model an exponential fit for the near count total with MOR estimates limited to 3,000 meters (Figure 82). As the near count total increases beyond 100,000, the estimated visibility is reduced significantly.

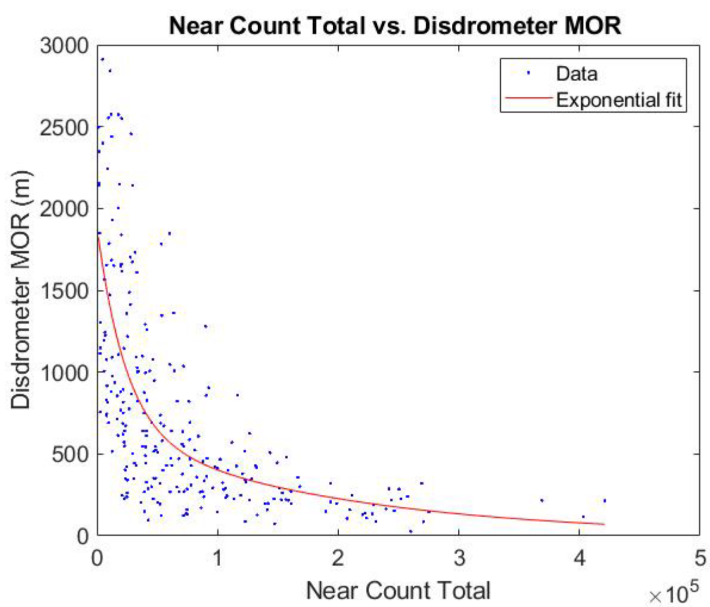

Figure 82: Nonlinear regression of near count total and disdrometer MOR.

For smaller near count totals, there is a large variance in the PD estimated visibility. The modeled results are given in Table 8.

Table 8: Nonlinear regression results from near count total and disdrometer MOR.

	Near Count Total vs Disdrometer MOR
Model	a*exp(b*x) + c*exp(d*x)
a	1.24E+03
b	-4.22E-05
c	650.2
d	-5.27E-06
R^2	0.484
RMSE	458

Regression was also used to evaluate some of the line scan statistics with the PD MOR. An additional statistical group, total return count beyond 75 meters, was calculated. This essentially treats the trees in the background as a target and uses the amount of target returns that were observed from the line scans as an estimate for visibility. Figure 83 shows the nonlinear regression of the far count total of returns beyond 75 meters with the MOR estimates limited to 1000 meters. Model parameters and statistics can be found in Table 9. As the count reaches zero, a target at 75 meters is no longer visible for the sensor. Therefore, extinction of targets that are normally detectable could serve as an indication of a DVE.

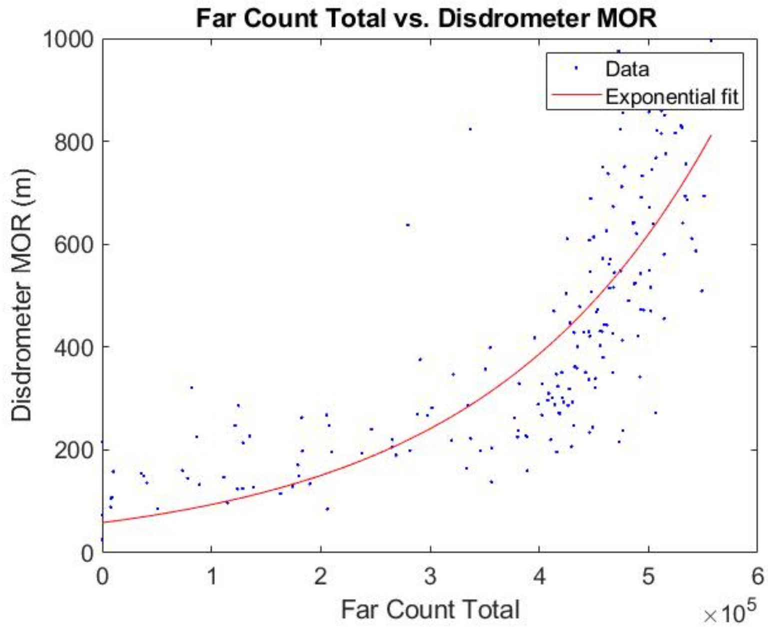

Figure 83: Nonlinear regression of far count total vs disdrometer MOR.

Table 9: Nonlinear regression results for far count total vs disdrometer MOR.

	Far Count Total vs Disdrometer MOR
Model	a*exp(b*x)
a	58.58
b	4.72E-06
R^2	0.6234
RMSE	148

The e-folding lengths calculated from the line scans were also compared with the disdrometer MOR (Figure 84). As the e-folding length gets closer to the scanner, the density of hydrometeors in the atmosphere has increased which affects visibility. The large variance of the results around and beyond 10 meters for e-folding length is attributed to the misclassifications of hydrometeors within the line scan. A linear trend is observed for e-folding lengths below 10 meters when limiting MOR to 1000 meters

(Figure 85). The heaviest estimated snowfalls from the PD are shown to have the smallest visibility estimate. The exponential decay of returns surrounding the TLS could be used to evaluate whiteout conditions as the sensor becomes saturated with returns in the near field. Linear regression was used to analyze correlation between MOR and e-folding length (Figure 86) and statistics can be found in Table 10.

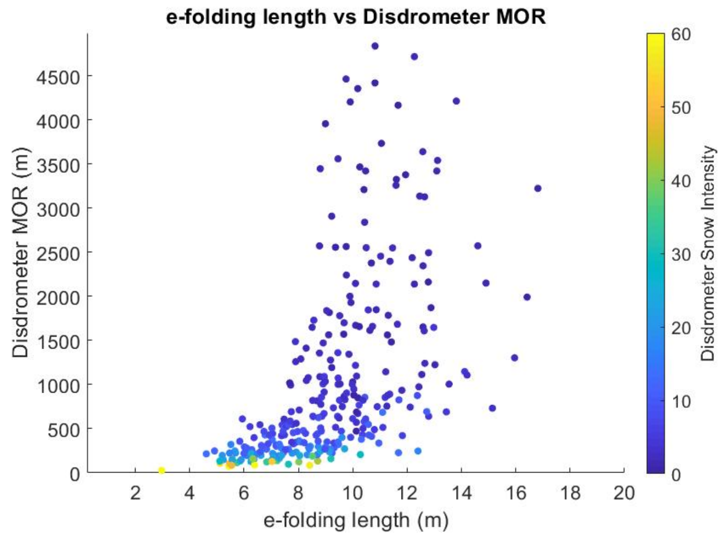

Figure 84: e-folding length vs disdrometer MOR (limited to 5000 meters). Colored by disdrometer snow intensity estimate.

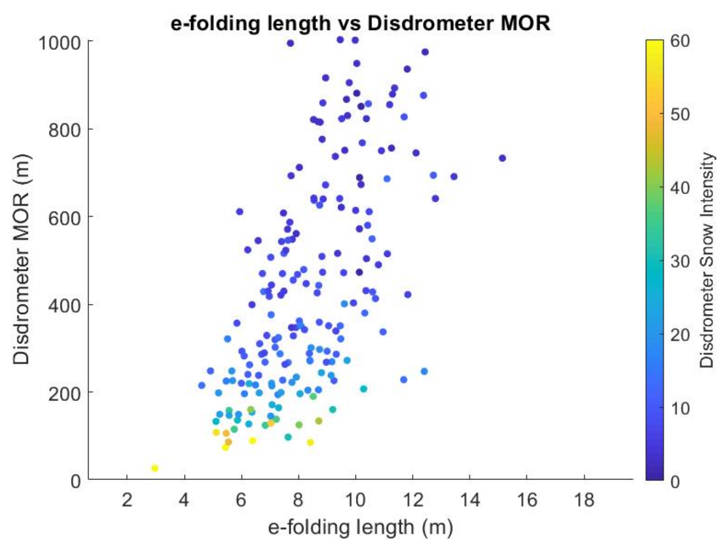

Figure 85: e-folding length vs disdrometer MOR (limited to 1000 meters). Colored by disdrometer snow intensity estimate.

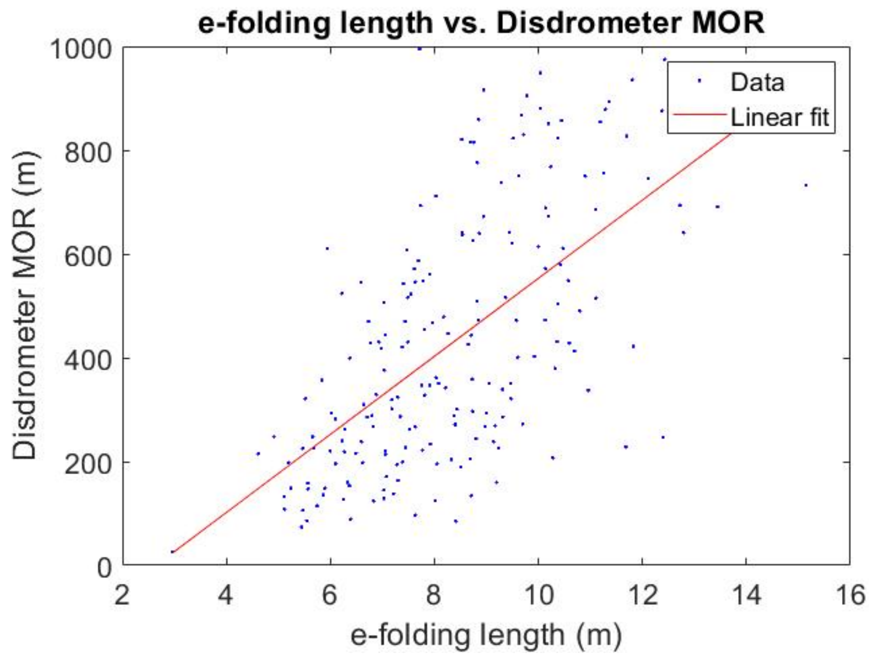

Figure 86: Linear regression of e-folding length vs disdrometer MOR.

A multi-variable linear regression was evaluated with the far count total, e-folding length and second return reflectance average for the Spectralon panel from the frame scans (Figure 87). The statistical results from this model can be found in Table 10. Both of the slopes from the e-folding length and multi-variable regression models proved to be statistically significant with a confidence level of 99%. The RMSE for these models are approximately 150-200 meters. This suggests that TLS observations have potential for estimating visibility conditions during heavy snowfall.

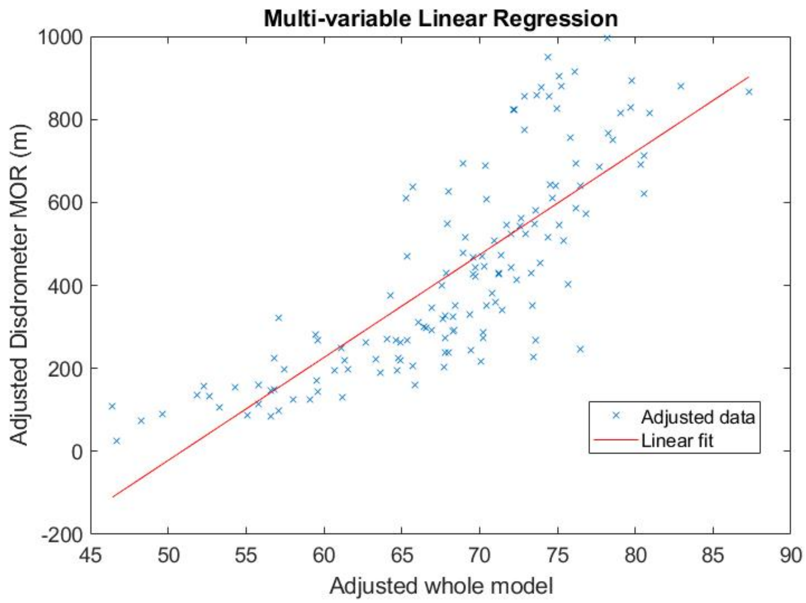

Figure 87: Multi-variable linear regression of far count total, average hydrometeor range, average 2nd return reflectance from Spectralon panel vs disdrometer MOR.

Table 10: Statistical results of linear regression models of disdrometer MOR.

	e-folding length vs Disdrometer MOR	Far Count Total, e-folding length and Average 2nd Return Reflectance of Spectralon Panel vs Disdrometer MOR
R^2	0.376	0.602
RMSE	191	156
SSR	4,115,287	5,056,468
SSE	6,821,607	3,348,743
MSR	4,115,287	1,685,489
MSE	36,093	24,443
F Statistic	114	69
F Critical	7	4
Significant	Yes	Yes

The PD MOR was also compared with the second return reflectance average from the Spectralon line scans and frame scan subsets. There is a large variance for large MOR values, but as the second return reflectance average from the Spectralon panel decreases below 70%, the visibility estimates have a larger reduction that is more consistent (Figure 88). It is not surprising that the data is poorly correlated for higher MOR values, due to the large extrapolation and unknown accuracy of the MOR estimates. Similar results were obtained for both the frame scan subset and Spectralon line scan, regardless of how many second returns were observed (Figure 89). Linear regression was used to evaluate the correlations between these datasets with a MOR limit of 1000 meters. The regressions and statistics can be found in Appendix F.

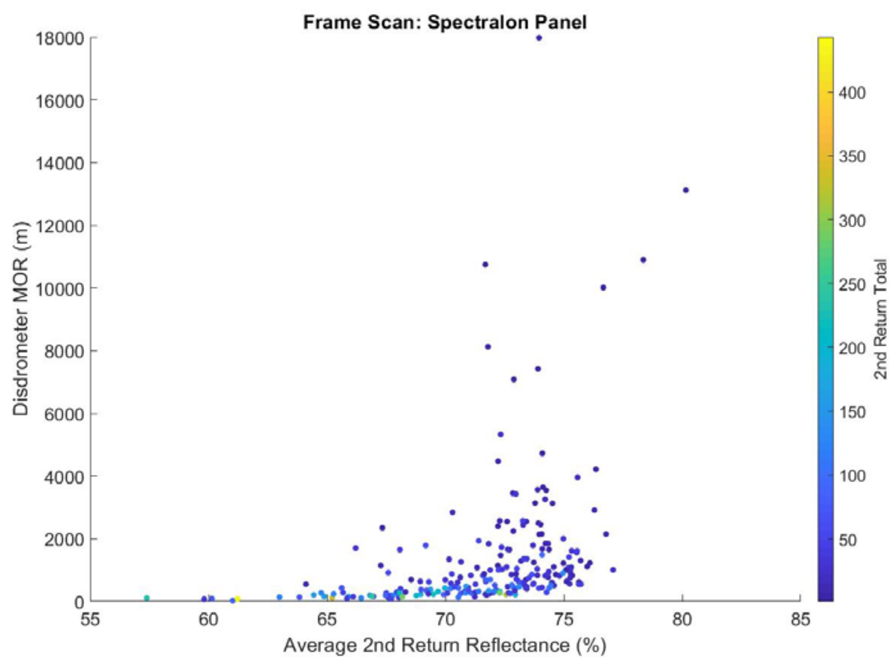

Figure 88: Frame scan Spectralon panel – Average 2nd reflectance return vs disdrometer MOR.

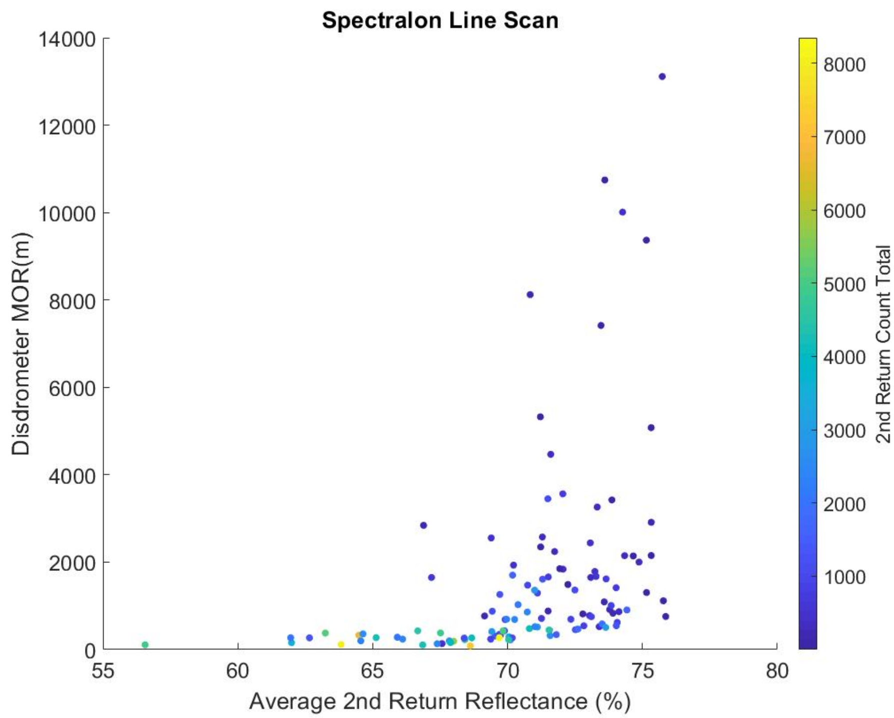

Figure 89: Spectralon line scan – Average 2nd reflectance return vs disdrometer MOR.

An interesting comparison was made between the PD MOR estimates and the maximum range of hydrometeors from the line scans. The two lowest observed MOR estimates from the PD were 26 and 74 meters and the maximum range from the corresponding line scans were 27 and 49 meters respectively. Almost all of the line scans were able to collect returns from a tree in the distance, approximately 75 meters away, but these two snow events that occurred sequentially on January 16 at 4 and 5 pm had no returns from the tree. Figure 90 shows the reduced ranges of the line scans due to whiteout conditions for the TLS system. Even though the PD samples a small area with a different wavelength than the TLS, low estimated visibility within the boundary of the tree also resulted in reduced range observations in the line scan.

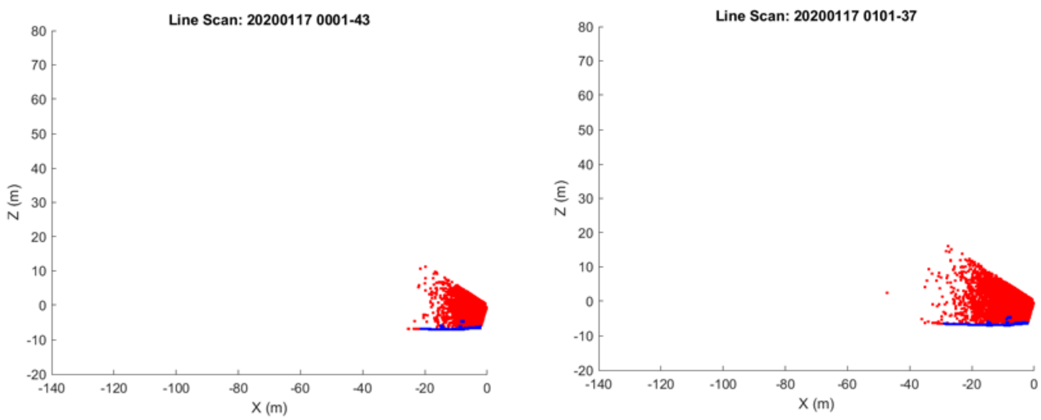

Figure 90: Line scans of maximum line scan range reductions

A hemispherical webcam, located at the CUES site approximately 1 km away from Sesame, provides a limited view of the weather conditions during these reduced visibility events. Figure 91 shows two images, one with reduced visibility and one without. It is difficult to distinguish some of the edges of the reduced visibility image. Ideally, a camera system should be set up to capture images with a longer range and more identifiable features that are also observed in the point cloud. If range extinction can be modeled to represent human visibility, then the TLS could provide a more accurate visible assessment of the environment surrounding the scanner compared to that of the PD or a forward scattering visibility meter.

Figure 91: Webcam images from CUES site - reduced visibility (top), clear visibility (bottom)

5. DISCUSSION

5.1. Can a TLS provide similar or enhanced snowfall metrics compared to other meteorological sensors?

This analysis has revealed various capabilities of the TLS for use as a meteorological sensor. Lidar point clouds are able to detect that a hydrometeor event is occurring and are sensitive to the intensity of the snowfall event. The automatic detection method for this study searched for returns in the atmosphere, but it was also shown that acquiring second returns from a target that typically only produces one return is a good indicator of snow as well. It is believed that the discrepant snow events stem from a variety of circumstances. Wind is suspected to be a factor by transporting settled snow from the ground and nearby trees into the atmosphere. An ensemble of smaller particles blown by the wind will more easily be detected by the larger volume of the TLS compared to the PD, which is shielded and has difficulty observing hydrometeors that are not falling vertically. The TLS system appears to be more sensitive to observing point returns compared with the PD classifying a hydrometeor for very light snow events.

The TLS has enhanced capabilities compared to the JUDS, with its ability to sample a larger area and record reflectance variations of the surface; this gives more details on the snowpack surrounding the scanner. Modeling TLS scan metrics with PD estimates proved statistically significant, which is promising for future research, showing that returns from the laser scanner can be used to estimate visibility and snowfall intensity rate.

5.2. Does FW scanning provide better snowfall estimation?

Examining the FW characteristics of laser pulses during snowfall shows that the waveform deviates when different targets are acquired within the range resolution of the scanner. Unlike the FW results obtained in fog (Pfenningbauer et al. 2014), the returns that met extinction in the atmosphere did not exhibit unique characteristics or the ability to penetrate far into dense snowfall. Possible reasons that the FW returns differ here is that fog consists of a uniform distribution of particles, which are much smaller and possess mie-scattering characteristics. Hydrometeors are significantly larger and create occlusions by absorbing and scattering the laser energy. Given the small size and low reflectance from hydrometeors at the laser's wavelength, it is likely that the laser energy is being impaired and not enough energy is being reflected back to exceed the detection threshold. For these reasons, FW analysis does not appear to provide an advantage compared to that of multi-return point clouds during whiteout conditions.

5.3. Can particle velocities be determined from a TLS?

Frame scans collected during hydrometeor events revealed streaks that are believed to be repeat measurements of individual hydrometeors. Of the 276 frame scans identified with hydrometeors, approximately 70% had some amount of point streaks present. Based on observations of the point clouds, the TLS's ability to record these streaks depends on a few factors, namely, how many hydrometeors are in the air, the wind conditions and if the hydrometeor is falling in the direction which the TLS is scanning. Heavy snowfall and high winds make it difficult for the scanner to observe streaks. Manual calculations from well-defined streaks were all within the velocity range from the PD. Evaluation of automated TLS velocity estimates revealed that 65% of the estimates were spurious. This is believed to be due to uncertainty in hydrometeor location due to motion of the laser beam when scanning and/or oversampling of returns near the scanner. Deriving hydrometeor speeds appears to be feasible with a TLS; however, results can be sporadic and inconsistent within scans depending on the weather conditions during data capture and snowfall intensity.

5.4. Are there any noticeable variations in data metrics due to hydrometeor size?

The PD has the ability to estimate a hydrometeor's size, but fundamental assumptions made in the instruments estimates are not ideal for solid precipitation. The median size from different collection periods were compared with various metrics derived from the TLS. However, based on the bulk statistics, particle size is not observable in TLS lidar scans. The range for median size estimates of hydrometeors varied from 0.687-2.75 mm. These are much smaller than the laser footprint, which varies from 6.5-29 mm for ranges from 0-75 m. TLS metrics are affected more by the intensity of snowfall than the median disdrometer size. A better truth metric for hydrometeor size is required to compare against TLS observations because the PD is not configured to accurately estimate solid precipitation; it only generates bulk statistics from snowfall events. The TLS' ability to discern hydrometeor sizes should be examined with controlled tests on hydrometeors of a known size.

5.5. Is a TLS able to estimate a snowfall intensity rate?

TLS statistics derived from hydrometeors and targets varied depending on the intensity of snowfall. Most hydrometeor returns occur within 10 meters of the scanner and the counts within 5 meters showed distinct variation between snowfall events. The return reflectance of hydrometeors within 2 meters of the scanner had significantly lower intensities compared with other hydrometeors. This is because the relative reflectance calibration is not well suited for small, low-reflectance targets. Heavier snowfall leads to more returns near the scanner, reducing the overall reflectance average for hydrometeors. First and second return reflectance averages from the Spectralon panel and tree trunk suggest that hydrometeors in the atmosphere impair the laser's energy, reducing the target amplitude. These statistics were used for modeling the PD estimate for snow intensity rate and all proved statistically significant. This indicates that TLS measurements have potential for estimating snowfall intensity. The multi-variable regression presented appears to be the most promising model for snowfall intensity rate and could be used to indicate differences between light, medium and heavy snowfall.

5.6. Do variations in TLS measurements relate to visibility?

A few events observed by the TLS show that it is capable of experiencing whiteout conditions due to heavy snowfall. The lowest PD visibility estimates aligned with the largest range reductions from the TLS. The PD MOR estimate extrapolates up to 20 km away from the single measurement location, which is far beyond the measurement range of this TLS, so estimates were limited for some of the correlation estimations. Counts, ranges and intensities were all modeled against the PD visibility estimates and proved statistically significant. A large number of hydrometeors observed near the scanner increased the near count total and affected the exponential decay of return counts, which relate to a DVE. In addition, the inability to acquire returns from targets at range indicate that a target is undetectable and likely impaired by a DVE. This suggests that statistics from hydrometeors and targets located around a TLS can be utilized in a establishing a framework to model visibility. For this study, targets were examined at relatively short distances compared to the TLS maximum range, due to the occlusions around the scanner. The use of targets and statistics at longer ranges would require the laser energy to traverse more of the atmosphere. This would produce greater reflectance reductions and fewer returns from a target, which could increase the sensitivity of the TLS to visibility reductions.

6. CONCLUSION AND FUTURE WORK

This thesis examined lidar and meteorological datasets collected during snowfall events at the Sesame Street Snow Study Plot in Mammoth Lakes, California. The objective was to analyze if the Riegl VZ-400 TLS system has the ability to determine visibility around the scanner and/or estimate properties related to hydrometeors by comparing results with the OTT Hydromet Parsivel^2 optical disdrometer. The questions presented in Chapter 1 are readdressed and italicized.

Can a TLS provide similar or enhanced snowfall metrics compared to other meteorological sensors? The VZ-400 demonstrated it is capable of detecting snowfall and the variation in measurements suggest that both visibility and snowfall intensity rate could be estimated. In addition, the TLS provides the ability to acquire depth and reflectance estimates for a large area compared to a static height estimate from an ultrasonic depth sensor. Although some snowfall velocity estimates could be obtained from the lidar scans, the TLS does not appear to give a reliable measure of particle velocity or size.

Does FW scanning provide better snowfall estimation? Analysis of returns during snowfall indicate that FW results can vary when multiple targets are observed within the range resolution of the scanner. However, during whiteout conditions, waveform characteristics do not yield additional information compared to a discrete returns.

Can particle velocities be determined from a TLS? There are certain instances where long, well-defined particle streaks from the TLS provide similar hydrometeor velocity estimates to the PD, but these results are sporadic and inconsistent among the lidar scans. Velocity estimates using small streaks yield erroneous results due to coordinate uncertainty and oversampling. Therefore, a TLS does not appear to be a reliable instrument for estimating snow particle velocity due to the scanning mechanics and the short distance over which the hydrometeors are observed.

Are there any noticeable variations in the TLS data metrics due to hydrometeor size? Hydrometeors observed in this study are much smaller than the laser footprint. The small size and low reflectance of hydrometeors makes it difficult for a TLS to distinguish size variations. The median disdrometer size estimate from the PD varies by only a few mm and fails to show correlations with any of the TLS observations.

Is a TLS able to estimate snowfall intensity rate? The slope from the multi-variable regression model evaluated with TLS observations and the PD estimate for snowfall intensity rate proved statistically significant with a confidence level of 99%. The model shows the capability to use the TLS to distinguish between light, moderate and heavy snowfall events.

Do variations in TLS measurements relate to visibility? Variations in TLS measurements do relate to visibility estimates from the PD. The increase of hydrometeor returns in the near range, changes in the e-folding length and a decrease of returns in the far range all showed a correlation with the PD MOR estimate. These TLS metrics relate to the atmospheric conditions and the sensor's ability to operate in a DVE.

Return statistics from hydrometeors appear to yield informative data from a TLS. Hydrometeors were mostly observed as first or second returns within 10 meters of the scanner; this region was the most affected by varying snowfall conditions. Detection of hydrometeors is limited and sporadic beyond 30 meters. This study has shown that hydrometer counts, their range variations and, for the VZ-400 specifically, changes in reflectance, have statistical properties that can be used for modeling purposes.

Reflectance reductions of the first returns from a target and reduced counts from large targets at range show that hydrometeors can obstruct the lasers energy in varying amounts. Both manmade and natural targets experienced reflectance reductions during different visibility conditions. This suggests that targets identified around a scanner can be utilized by comparing return counts and intensities during a DVE with values obtained from normalized visibility conditions. Since hydrometeors have been shown to scatter and absorb the laser's energy, targets at longer ranges could yield information regarding atmospheric conditions along the laser cone of diffraction. The laser footprint at longer ranges is likely too big for individual hydrometeors to reflect enough energy for a target to be detected; however, the sensor exhibited that it is capable of experiencing whiteout conditions from heavy snowfall as returns became extinguished at shorter ranges.

Development of a visibility model for a TLS system using range extinction and return statistics could be developed for a sensor's operable range, which varies from a few hundred meters up to a few kilometers. This could serve as an indicator for reduced visibility within its measurement range and improved spatial resolution for autonomous monitoring of critical areas, such as airports, harbors and highways. Although the models developed in the thesis have shown promising results, it is only for one season, using one model of TLS at a specific site with limited range observations and is compared against estimates from another instrument. Further validation will be required to determine the optimal settings (targets, ranges, statistic thresholds, etc.) for a specific instrument/application/location with accurate control measurements in place.

There are a few recommendations the author believes will help this research for future analysis. Use of fixed targets at varying distances within the instruments measurement range and field of view could allow the TLS to observe more distinct reflectance reductions, as the laser pulse has to travel through more of the atmosphere. Longer ranges to targets would also provide more meaningful statistics related to return counts/extinction.

It is hard to estimate visibility without having a visual reference, especially considering there are many factors besides hydrometeors that affect visibility. Having a camera on site collecting images of features around the TLS during each lidar scan will help distinguish differences between observations in the visible spectrum of light and active observations of the TLS in the near infrared wavelength.

Past research (Battaglia et al. 2010) has shown that the size estimate from the PD for solid precipitation has large uncertainty, especially for smaller particle sizes. In addition, the PD only provided bulk observations of hydrometeors for one-minute intervals. Performing different experiments with known hydrometer sizes might reveal better correlation with TLS statistics that could be utilized for discerning hydrometeor size.

The Riegl VZ-400 is a very powerful instrument that is capable of making accurate measurements of its surroundings, but it was not designed or intended to measure small targets with low-reflectance values like hydrometeors. With an expensive price point over $100,000, it would be hard to justify employing multiple sensors simply for monitoring purposes when there could be more affordable solutions available. It would be beneficial to conduct a study with a variety of laser scanners to see if other systems have similar observation characteristics. The evolution of autonomous vehicles has spurred research and development for various lidar sensors and mass production of sensors has reduced the costs significantly. There are now TLS sensors available that are 20-200 times less expensive, which if provide observations comparable to the Riegl VZ-400, could be a more feasible financial option for a network of sensors for monitoring visibility conditions.

Analysis has shown that a TLS is able to detect and observe variations between different snowfall events. Further analysis should be conducted with more controlled observations for specific applications to help realize a sensors true potential.

REFERENCES

Angulo-Martínez, Marta, Santiago Beguería, Borja Latorre, and María Fernández-Raga. "Comparison of Precipitation Measurements by OTT Parsivel 2 and Thies LPM Optical Disdrometers." *Hydrology and Earth System Sciences* 22, no. 5 (2018): 2811–37. http://dx.doi.org.ezproxy.lib.uh.edu/10.5194/hess-22-2811-2018.

Bair, Edward H. "Forecasting Artificially-Triggered Avalanches in Storm Snow at a Large Ski Area." *Cold Regions Science and Technology* 85 (January 1, 2013): 261–69. https://doi.org/10.1016/j.coldregions.2012.10.003.

Bair, Edward H, Robert E Davis, and Jeff Dozier. "Hourly Mass and Snow Energy Balance Measurements from Mammoth Mountain, CA USA, 2011–2017," 2018, 15.

Bair, Edward H, Robert E Davis, David C Finnegan, Adam L LeWinter, and Ethan Guttmann. "Can We Estimate Precipitation Rate during Snowfall Using a Scanning Terrestrial LiDAR?," 2012, 7.

Bair, Edward H., Jeff Dozier, Robert E. Davis, Michael T. Colee, and Keran J. Claffey. "CUES—a Study Site for Measuring Snowpack Energy Balance in the Sierra Nevada." *Frontiers in Earth Science* 3 (2015). https://doi.org/10.3389/feart.2015.00058.

Barup, Kerstin, Mikkel Brydegaard, Zuguang Guan, Anders Hedenström, Jenny Hellström, Märta Lewander, Patrik Lundin, Patrik Lundin, Christer Löfstedt, Aboma Merdasa, Annika Olsson, Anna Runemark, Gabriel Somesfalean, Erik Svensson, Maren Wellenreuther, Susanne Åkesson, Sune Svanberg. "Multi-Disciplinary Lidar

Applications." In *Lasers, Sources and Related Photonic Devices*, JTuA4. San Diego, California: OSA, 2010. https://doi.org/10.1364/ASSP.2010.JTuA4.

Battaglia, Alessandro, Elke Rustemeier, Ali Tokay, Ulrich Blahak, and Clemens Simmer. "PARSIVEL Snow Observations: A Critical Assessment." *Journal of Atmospheric and Oceanic Technology* 27, no. 2 (February 1, 2010): 333–44. https://doi.org/10.1175/2009JTECHA1332.1.

Bhardwaj, Anshuman, Lydia Sam, Akanksha Bhardwaj, and FJavier Martin-Torres. "LiDAR Remote Sensing of the Cryosphere: Present Applications and Future Prospects." *Remote Sensing of Environment* 177 (2016): 125–43. http://dx.doi.org.ezproxy.lib.uh.edu/10.1016/j.rse.2016.02.031.

Bratt, Richard M., and Allen D. Walker. "Degraded Visual Environment Paradigm Shift from Mission Deterrent to Combat Enabler." In *Situation Awareness in Degraded Environments 2019*, 11019:1101902. International Society for Optics and Photonics, 2019. https://doi.org/10.1117/12.2519013.

Camps, Adriano, Marc Rodriguez-Cassola, and William Emery. Introduction to Satellite Remote Sensing: Atmosphere, Ocean and Land Applications. Elsevier, 2017.

CNN, By David Williams. "The Terror of a 131-Car Pileup Revealed in Stranded Motorists' 911 Calls." CNN Digital, February 27, 2019. https://www.cnn.com/2019/02/27/us/wisconsin-pileup-911-trnd/index.html.

Davis, Robert E, Kelly Elder, Daniel Howlett, and Eddy Bouzaglou. "Relating Storm and Weather Factors to Dry Slab Avalanche Activity at Alta, Utah, and Mammoth Mountain, California, Using Classification and Regression Trees." *Cold Regions*

Science and Technology 30, no. 1 (December 1, 1999): 79–89. https://doi.org/10.1016/S0165-232X(99)00032-4.

Deems, Jeffrey S., Peter J. Gadomski, Dominic Vellone, Ryan Evanczyk, Adam L. LeWinter, Karl W. Birkeland, and David C. Finnegan. "Mapping Starting Zone Snow Depth with a Ground-Based Lidar to Assist Avalanche Control and Forecasting." *Cold Regions Science and Technology* 120 (December 1, 2015): 197–204. https://doi.org/10.1016/j.coldregions.2015.09.002.

Deems, Jeffrey S., Thomas H. Painter, and David C. Finnegan. "Lidar Measurement of Snow Depth: A Review." *Journal of Glaciology* 59, no. 215 (ed 2013): 467–79. https://doi.org/10.3189/2013JoG12J154.

Dennis H. Goldstein, David B. Chenault, and J. Larry Pezzaniti. "Polarimetric Characterization of Spectralon," Vol. 3754, 1999. https://doi.org/10.1117/12.366323.

Hackel, T., J. D. Wegner, and K. Schindler. "Contour Detection in Unstructured 3D Point Clouds." In *2016 IEEE Conference on Computer Vision and Pattern Recognition (CVPR)*, 1610–18, 2016. https://doi.org/10.1109/CVPR.2016.178.

Hartzell, P. J., C. L. Glennie, and D. C. Finnegan. "Empirical Waveform Decomposition and Radiometric Calibration of a Terrestrial Full-Waveform Laser Scanner." *IEEE Transactions on Geoscience and Remote Sensing* 53, no. 1 (January 2015): 162–72. https://doi.org/10.1109/TGRS.2014.2320134.

Higginbotham, Mike. "Army Aviation's Enduring Challenge." www.army.mil, June 24, 2014. https://www.army.mil/article/128754/army_aviations_enduring_challenge.

Huang, Gwo-Jong, Viswanathan N. Bringi, Andrew J. Newman, Gyuwon Lee, Dmitri Moisseev, and Branislav M. Notaroš. “Dual-Wavelength Radar Technique Development for Snow Rate Estimation: A Case Study from GCPEx.” *Atmospheric Measurement Techniques* 12, no. 2 (February 2019): 1409–27. https://doi.org/10.5194/amt-12-1409-2019.

Judd Communications - Home. Accessed March 9, 2021. http://juddcom.com/.

Kwon, Taek M. “Atmospheric Visibility Measurements Using Video Cameras: Relative Visibility,” n.d., 51.

Locatelli, John D., and Peter V. Hobbs. “Fall Speeds and Masses of Solid Precipitation Particles.” *Journal of Geophysical Research (1896-1977)* 79, no. 15 (1974): 2185–97. https://doi.org/10.1029/JC079i015p02185.

Löffler-Mang, Martin, and Ulrich Blahak. “Estimation of the Equivalent Radar Reflectivity Factor from Measured Snow Size Spectra.” *Journal of Applied Meteorology and Climatology* 40, no. 4 (April 1, 2001): 843–49. https://doi.org/10.1175/1520-0450(2001)040<0843:EOTERR>2.0.CO;2.

Löffler-Mang, Martin, and Jürg Joss. “An Optical Disdrometer for Measuring Size and Velocity of Hydrometeors.” *Journal of Atmospheric and Oceanic Technology* 17, no. 2 (February 1, 2000): 130–39. https://doi.org/10.1175/1520-0426(2000)017<0130:AODFMS>2.0.CO;2.

Lufft. “Compact Weather Sensors - WS600-UMB Smart Weather Sensor.” Accessed March 9, 2021. https://www.lufft.com/products/compact-weather-sensors-293/ws600-umb-smart-weather-sensor-1832/.

OTT Hydromet (2016). OTT Parsivel[2] [Brochure]. Retrieved from https://www.otthydromet.com/en/p-ott-parsivel-laser-present-weather-sensor/70.210.002.3.0

Pfennigbauer, Martin, and Andreas Ullrich. "Improving Quality of Laser Scanning Data Acquisition through Calibrated Amplitude and Pulse Deviation Measurement." edited by Monte D. Turner and Gary W. Kamerman, 76841F. Orlando, Florida, 2010. https://doi.org/10.1117/12.849641.

Pfennigbauer, Martin, Clifford Wolf, Josef Weinkopf, and Andreas Ullrich. "Online Waveform Processing for Demanding Target Situations," 9080:90800J–90800J–10. SPIE, 2014. https://doi.org/10.1117/12.2052994.

Prokop, Alexander. "Assessing the Applicability of Terrestrial Laser Scanning for Spatial Snow Depth Measurements." *Cold Regions Science and Technology*, Snow avalanche formation and dynamics, 54, no. 3 (November 1, 2008): 155–63. https://doi.org/10.1016/j.coldregions.2008.07.002.

RIEGL Laser Measurement Systems GmbH. (2017). LAS Extrabytes Implementation in RIEGL Software [White paper]. http://www.riegl.com/uploads/tx_pxpriegldownloads/Whitepaper_LASextrabytes_implementation_in-RIEGLSoftware_2017-12-04.pdf

Sankaré, Housseyni, and Julie M. Thériault. "On the Relationship between the Snowflake Type Aloft and the Surface Precipitation Types at Temperatures near 0°C." *Atmospheric Research* 180 (November 1, 2016): 287–96. https://doi.org/10.1016/j.atmosres.2016.06.003.

Sekhon, R. S., and R. C. Srivastava. "Snow Size Spectra and Radar Reflectivity." *Journal of the Atmospheric Sciences* 27, no. 2 (March 1, 1970): 299–307. https://doi.org/10.1175/1520-0469(1970)027<0299:SSSARR>2.0.CO;2.

Sevruk, B., M. Ondrás, and B. Chvíla. "The WMO Precipitation Measurement Intercomparisons." *Atmospheric Research*, 7th International Workshop on Precipitation in Urban Areas, 92, no. 3 (May 1, 2009): 376–80. https://doi.org/10.1016/j.atmosres.2009.01.016.

Telling, Jennifer, Andrew Lyda, Preston Hartzell, and Craig Glennie. "Review of Earth Science Research Using Terrestrial Laser Scanning." *Earth-Science Reviews* 169 (June 1, 2017): 35–68. https://doi.org/10.1016/j.earscirev.2017.04.007.

Tokay, Ali, Walter A. Petersen, Patrick Gatlin, and Matthew Wingo. "Comparison of Raindrop Size Distribution Measurements by Collocated Disdrometers." *Journal of Atmospheric and Oceanic Technology* 30, no. 8 (August 1, 2013): 1672–90. https://doi.org/10.1175/JTECH-D-12-00163.1.

Wang, Jingli, Xulin Liu, Xihua Yang, Ming Lei, Shunxian Ruan, Kai Nie, Yupeng Miao, and Jincheng Liu. "Development and Evaluation of a New Digital Photography Visiometer System for Automated Visibility Observation." *Atmospheric Environment* 87 (April 1, 2014): 19–25. https://doi.org/10.1016/j.atmosenv.2013.12.045.

World Meteorological Organization. *Guide to Meteorological Instruments and Methods of Observation*. Geneva: World Meteorological Organization, 2008.

Wyman, P. W. “LASER RADAR RANGE EQUATION CONSIDERATIONS:” Fort Belvoir, VA: Defense Technical Information Center, December 11, 1969. https://doi.org/10.21236/AD0699519.

Yuter, Sandra E., David E. Kingsmill, Louisa B. Nance, and Martin Löffler-Mang. “Observations of Precipitation Size and Fall Speed Characteristics within Coexisting Rain and Wet Snow.” *Journal of Applied Meteorology and Climatology* 45, no. 10 (October 1, 2006): 1450–64. https://doi.org/10.1175/JAM2406.1.

APPENDIX A

Spectralon panel calibration report

NO. DM-04109-001
REV. 01

Labsphere

TARGET REFLECTANCE UNIFORMITY TEST REPORT

REPORT NUMBER: 102725-1-1
DATE OF REPORT: 9/25/2018
PAGE 1 OF 2

RENDERED TO: CRREL

AUTHORIZATION: Purchase Order: **PHONE ORDER**

CALIBRATION LAB: Labsphere, Inc., Optical Calibration Laboratory
231 Shaker Street
North Sutton, N.H. 03260
Tel 603-927-4266 Fax 603-927-4694

TESTED SYSTEM OR STANDARD

PF-TARGET, P/N: AA-01391-094, PFT-94-05M-UF-WM

PF-TARGET, S/N: 0912183994

CALIBRATED REFERENCE STANDARD

REFL-26: SRS-99-020, SN: 7A41A-4744

The above standard is traceable following the NIST method of utilizing pressed polytetrafluoroethylene (PTFE) as the reference standard[1,2].

MEASUREMENT REQUESTED
Uniformity Mapping via Hemispherical/8° Spectral Reflectance Measurement at 905nm
Hemispherical/8° Spectral Reflectance Measurement

APPLICABLE DOCUMENTS
DM-13001-000 Product Appearance and Mechanical-fit Requirements

TEST AND TEST METHOD
The spectral reflectance is measured for the target listed above. The reflectance is determined by using an RSA-OO-FO and a CDS 610 Spectrometer. Reflectance measurements are taken in a 5 x 5 grid of equally spaced measurements across the target and reported at 905nm in Table II. The average reflectance at any given wavelength is expressed as the average reflectance of target from the mapping data and presented in Table III as (equation below is at 600nm):

$$\bar{R}_{600nm} = \frac{\sum R_i}{n}$$

The acceptable reflectance tolerance is calculated from the data taken at 600nm and is reported in Table I.

The acceptable uniformity tolerance is expressed as the range of absolute reflectances on either side of the average reflectance (equation below is at 600nm):

$$\textit{Uniformity Range} = R_{600nm\ min} < \bar{R}_{600nm} < R_{600nm\ max}$$

The acceptable uniformity tolerance is calculated from the data taken at 905nm and is reported in Table I along with the average reflectance at 905nm.

[1] Wiedner V.R., and Hsia, J. J. "Reflection Properties of Pressed Polytetrafluoroethylene Powder", J.Opt.Soc.Am., Vol71, 1981, pp856-861

[2] Barnes, P.Y., Early, E.A., and Parr, A.C., "NIST Measurement Services: Spectral Reflectance," U.S. Dept. of Commerce, 1998.

Labsphere

TARGET REFLECTANCE UNIFORMITY TEST REPORT

MEASUREMENT RESULTS

Table I
Average Reflectance and Acceptable Reflectance Uniformity Range

Average Reflectance @ 600nm	96.5 %
Average Reflectance @ 905nm	95.3 %
Uniformity Range	FALSE %

Table II
Reflectance Map
This table is absolute reflectance

	A	B	C	D	E
1	94.3	94.6	94.4	94.9	94.0
2	95.4	95.1	95.1	95.5	95.2
3	95.0	95.7	95.7	95.6	95.8
4	95.2	95.7	95.8	96.0	96.4
5	95.3	95.2	95.1	94.9	95.5

Table III
Average Spectral Reflectance

Wavelength (nm)	Reflectance (%R)	Wavelength (nm)	Reflectance (%R)	Wavelength (nm)	Reflectance (%R)	Wavelength (nm)	Reflectance (%R)
350	93.5	520	96.4	690	95.9	860	95.4
360	87.4	530	96.6	700	96.0	870	96.0
370	95.7	540	96.3	710	95.9	880	95.4
380	95.7	550	96.5	720	96.0	890	95.6
390	96.6	560	96.5	730	96.3	900	96.3
400	93.6	570	96.5	740	95.9	910	95.5
410	95.9	580	96.4	750	95.8	920	95.1
420	97.5	590	96.4	760	95.7	930	95.4
430	96.4	600	96.5	770	95.8	940	95.5
440	95.6	610	96.4	780	95.7	950	95.9
450	96.3	620	96.4	790	95.6	960	95.7
460	96.5	630	96.2	800	95.8	970	95.8
470	96.5	640	96.3	810	96.0	980	94.9
480	96.8	650	96.4	820	95.5	990	96.5
490	96.8	660	96.2	830	95.5	1000	96.2
500	96.5	670	96.3	840	95.7		
510	97.0	680	96.0	850	95.8		

Measured by:

Title: Optical Calibration Technician

ISO 9001 REGISTERED

APPENDIX B

Count statistics calculated and used from line scan analysis

Count Statistics	Used	Discarded
1st Return Count	x	
2nd Return Count		x
3rd Return Count		x
4th Return Count		x
Single Return Count	x	
Double Return Count	x	
Triple Return Count		x
Quadruple Return Count		x
Near Count Total	x	
Far Count Total	x	

APPENDIX C

Range statistics calculated and used from line scan analysis

Range Statistics	Used	Discarded
Average Hydrometeor Range	x	
e-folding length	x	
1st Return Minimum		x
1st Return Maximum		x
1st Return Average	x	
1st Return Variance		x
2nd Return Minimum		x
2nd Return Maximum		x
2nd Return Average		x
2nd Return Variance		x
3rd Return Minimum		x
3rd Return Maximum		x
3rd Return Average		x
3rd Return Variance		x
4th Return Minimum		x
4th Return Maximum		x
4th Return Average		x
4th Return Variance		x
Single Return Minimum		x
Single Return Maximum		x
Single Return Average		x
Single Return Variance		x
Double Return Minimum		x
Double Return Maximum		x
Double Return Average		x
Double Return Variance		x
Triple Return Minimum		x
Triple Return Maximum		x
Triple Return Average		x
Triple Return Variance		x
Quadruple Return Minimum		x
Quadruple Return Maximum		x
Quadruple Return Average		x
Quadruple Return Variance		x

APPENDIX D

Reflectance statistics calculated and used from line scan analysis

Reflectance Statistics	Used	Discarded
1st Return Minimum		x
1st Return Maximum		x
1st Return Average	x	
1st Return Variance		x
2nd Return Minimum		x
2nd Return Maximum		x
2nd Return Average		x
2nd Return Variance		x
3rd Return Minimum		x
3rd Return Maximum		x
3rd Return Average		x
3rd Return Variance		x
4th Return Minimum		x
4th Return Maximum		x
4th Return Average		x
4th Return Variance		x
Single Return Minimum		x
Single Return Maximum		x
Single Return Average		x
Single Return Variance		x
Double Return Minimum		x
Double Return Maximum		x
Double Return Average		x
Double Return Variance		x
Triple Return Minimum		x
Triple Return Maximum		x
Triple Return Average		x
Triple Return Variance		x
Quadruple Return Minimum		x
Quadruple Return Maximum		x
Quadruple Return Average		x
Quadruple Return Variance		x

APPENDIX E

Non-linear regression of Spectralon panel second returns vs disdrometer snow intensity

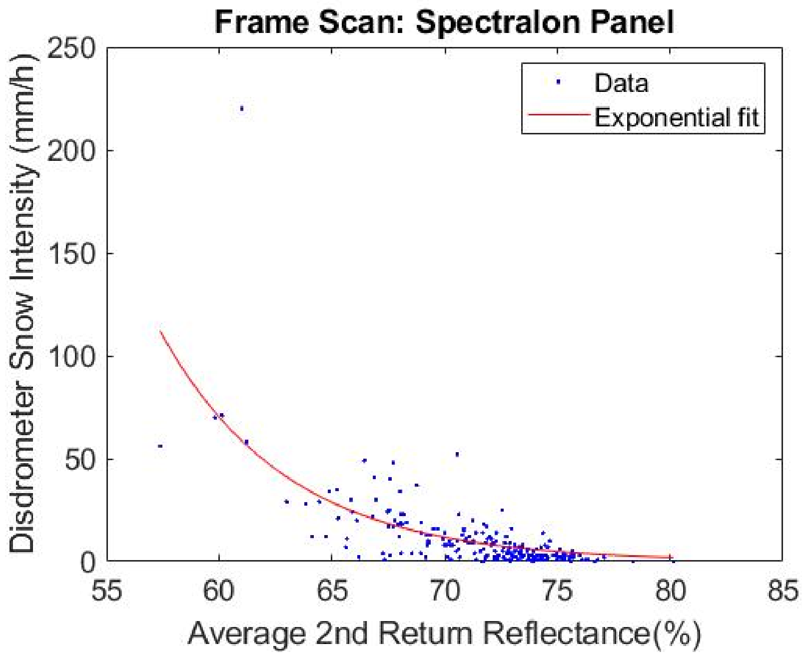

Linear regression of average 2nd return reflectance from the Spectralon panel from frame scans identified with hydrometeors vs disdrometer snow intensity

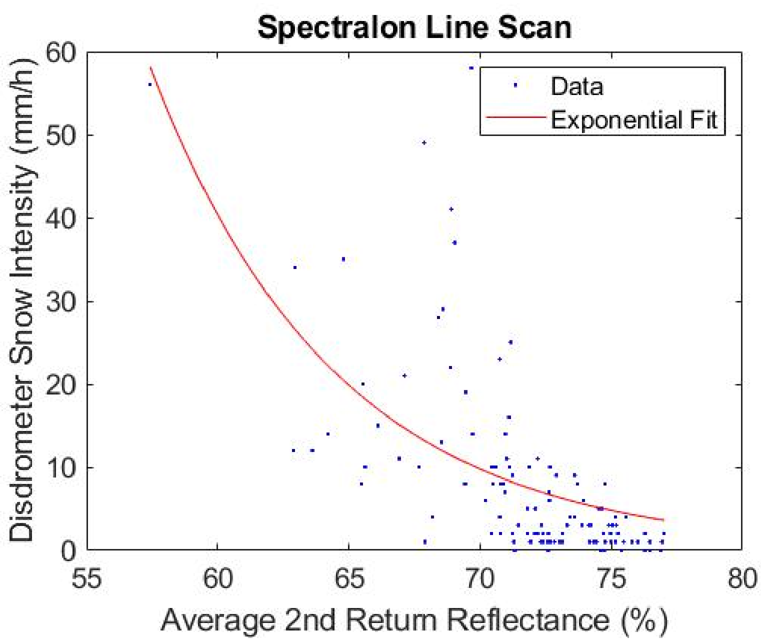

Linear regression of average 2nd return reflectance from Spectralon line scan vs disdrometer snow intensity

Statistical results of linear regression models of disdrometer snow intensities from Spectralon panel

	Frame Scan Average 2nd Return Reflectance vs Disdrometer Snow Intensity	Spectralon Line Scan Average 2nd Return Reflectance vs Disdrometer Snow Intensity
Model	a*exp(b*x)	a*exp(b*x)
a	3.158E+06	2.004E+05
b	-0.1789	-0.1418
R^2	0.460	0.396
RMSE	13.79	8.87

APPENDIX F

Linear regression of Spectralon panel second returns vs disdrometer MOR

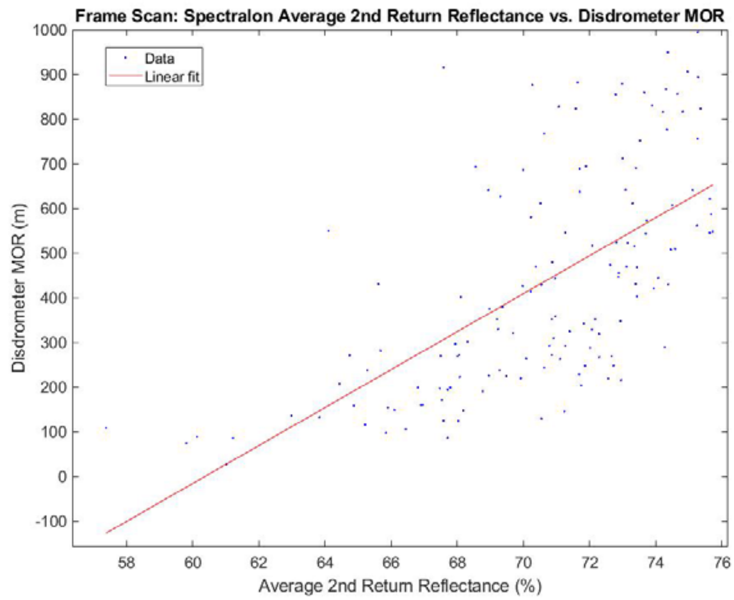

Linear regression of Spectralon average 2nd return intensity from a frame scan vs disdrometer MOR

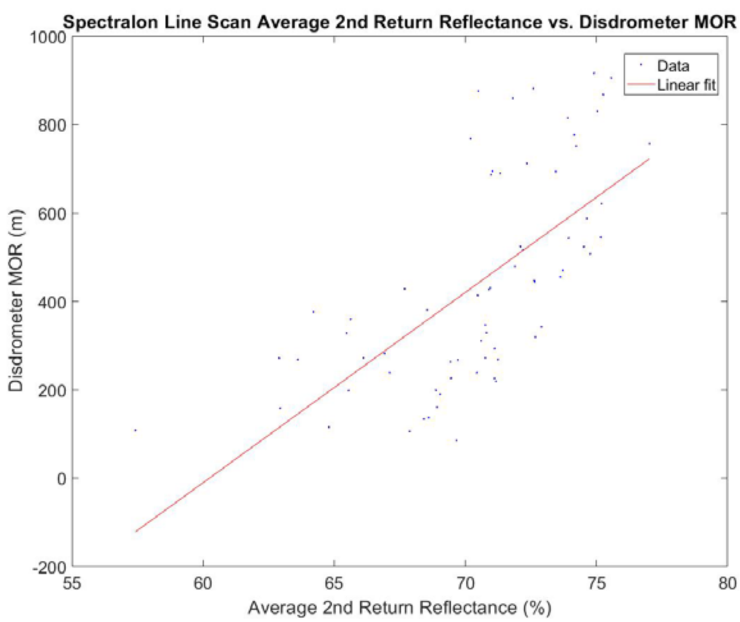

Linear regression of Spectralon average 2nd return reflectance from the Spectralon line scan vs disdrometer MOR

Statistical results of linear regression models of disdrometer MOR from Spectralon panel

	Frame Scan - Spectralon Average 2nd Return Reflectance vs Disdrometer MOR	**Spectralon Scan Average 2nd Return Reflectance vs Disdrometer MOR**
R^2	0.398	0.434
RMSE	191	182
SSR	3,342,214	1,677,629
SSE	5,062,997	2,186,556
MSR	3,342,214	1,677,629
MSE	36,424	33,130
F Statistic	92	51
F Critical	7	7
Significant	Yes	Yes